2018

Biomass Burning in the Conterminous United States: A Comparison and Fusion of Active Fire Observations from Polar-Orbiting and Geostationary Satellites for Emissions Estimation

Fangjun Li
South Dakota State University

BIOMASS BURNING IN THE CONTERMINOUS UNITED STATES: A COMPARISON AND FUSION OF ACTIVE FIRE OBSERVATIONS FROM POLAR-ORBITING AND GEOSTATIONARY SATELLITES FOR EMISSIONS ESTIMATION

BY

FANGJUN LI

A dissertation submitted in partial fulfillment of the requirements for the

Doctor of Philosophy

Major in Geospatial Science and Engineering

Specialization in Remote Sensing Geography

South Dakota State University

2018

BIOMASS BURNING IN THE CONTERMINOUS UNITED STATES: A COMPARISON AND FUSION OF ACTIVE FIRE OBSERVATIONS FROM POLAR-ORBITING AND GEOSTATIONARY SATELLITES FOR EMISSIONS ESTIMATION

FANGJUN LI

This dissertation is approved as a creditable and independent investigation by a candidate for the Doctor of Philosophy in Geospatial Science and Engineering degree and is acceptable for meeting the dissertation requirements for this degree. Acceptance of this does not imply that the conclusions reached by the candidate are necessarily the conclusions of the major department.

Xiaoyang Zhang, Ph.D.
Dissertation Advisor Date

Geoffrey M. Henebry, Ph.D.
Co-Director, Geospatial Sciences
Center of Excellence Date

Kimchel C. Doerner
Dean, Graduate School Date

To my wife, Juan Xie

ACKNOWLEDGMENTS

First and foremost, endless thanks and gratitude to my advisor, Dr. Xiaoyang Zhang, who patiently and encouragingly guided me through the course of this dissertation. Thanks for your inspirational mentoring, thanks for patiently editing my horrible writings, thanks for setting me on this academic path, and thanks for preparing us terrific Chinese food in holidays. You are a great advisor, and a good friend. It is a great honor for me to be your first Ph.D. student in SDSU. I am gratefully indebted to your financial assistance for conducting this study.

I am grateful to my Ph.D. committee members. Dr. David P. Roy, thanks for your insightful comments to improve this dissertation, and thanks for teaching me, the funny "black bear", about the fundamentals of quantitative remote sensing. I thank Dr. Michael C. Wimberly for being glad to join the committee after Dr. Mark A. Cochrane's leaving and giving helpful suggestions. I thank Dr. Mark A. Cochrane, the former member, for teaching me about fire knowledge. I also thank Dr. Billy Fuller for sharing experiences.

I also would like to thank Dr. Geoffrey Henebry and Dr. Niall P. Hanan for teaching me about essential writing and oral communication skills, and for creating opportunities to practice them in seminars and in public.

Last but not least, infinite thanks to my family. Mother and father, I sincerely appreciate your selfless supports from kindergarten to Ph.D. The person really responsible for my pursuit of this degree in SDSU is my wife, Juan Xie, who is for most of the best things in my life. She discovered the opportunity by chance and encouraged and helped me from the application to the final defense. Special thanks to my little angel, Helen, who brings me happiness.

CONTENTS

ABBREVIATIONS

ABI	Advanced Baseline Imager
AOD	Atmospheric Optical Depth
BBE	Biomass-Burning Emissions
CBI	Composite Burn Index
CC	Combustion Completeness
CLASS	Comprehensive Large Array-Data Stewardship System
CO	Carbon Monoxide
CONUS	Conterminous United States
EOS	Earth Observing System
EPA	Environmental Protection Agency
ETM+	Enhanced Thematic Mapper Plus
FBCC	FRE biomass combustion coefficient
FC	Fuel Consumption
FCCS	Fuel Characteristic Classification System
FEER	Fire Energetics and Emissions Research
FINN	Fire INventory from NCAR
FLAMBE	Fire Locating and Modeling of Burning Emissions
FRE	Fire Radiative Energy
FRP	Fire Radiative Power
GBBEP-Geo	Global Geostationary Satellite Biomass Burning Emissions Product
GBBEPx	Blended Global Biomass Burning Emissions Product from MODIS, VIIRS and Geostationary Satellites

GFAS	Global Fire Simulating System
GFED	Global Fire Emissions Database
Gg	Gigagram
GLCC	Global Land Cover Characterization
GMTCO	Moderate Bands Terrain Corrected Geolocation
GOES	Geostationary Operational Environmental Satellite system
ha	hectare
IGBP	International Geosphere-Biosphere Program
IPCC	Intergovernmental Panel on Climate Change
JPSS	Joint Polar Satellite System
km	kilometer
Land SIPS	Land Science Investigator-led Processing System
MMDBD	Monthly Maximum Diurnal Burning Duration
MJ	Megajoule
MODIS	Moderate Resolution Imaging Spectroradiometer
MSG	Meteosat Second Generation
MTBS	Monitoring Trends in Burn Severity
MW	Megawatt
NASA	National Aeronautics and Space Administration
NDEAF-L2	Data Exploitation Level 2 Active Fire
NEI	National Emissions Inventory
NEMS	NOAA Environmental Modeling System (NEMS)
NLCD	National Land Cover Database

NOAA	National Oceanic and Atmospheric Administration
OLI	Operational Land Imager
PM2.5	Particulate Matter with a diameter less than 2.5μm
QFED	Quick Fire Emissions Dataset
RMA	Reduced Major Axis
SEVIRI	Spinning Enhanced Visible and Infrared Imager
Suomi NPP	Suomi National Polar-orbiting Partnership
TM	Thematic Mapper
UTM	Universal Transverse Mercator
VIIRS	Visible Infrared Imaging Radiometer Suite
VZA	View Zenith Angle
WF_ABBA	WildFire Automated Biomass Burning Algorithm
WFEIS	Wildland Fire Emissions Information System
WRF-Chem	Weather Research and Forecasting (WRF) model coupled with Chemistry

LIST OF FIGURES

LIST OF TABLES

ABSTRACT

BIOMASS BURNING IN THE CONTERMINOUS UNITED STATES: A COMPARISON AND FUSION OF ACTIVE FIRE OBSERVATIONS FROM POLAR-ORBITING AND GEOSTATIONARY SATELLITES FOR EMISSIONS ESTIMATION

FANGJUN LI

2018

Biomass burning is an important source of atmospheric greenhouse gases and aerosol emissions that significantly influence climate and air quality. Estimation of biomass-burning emissions (BBE) has been limited to the conventional method in which parameters (i.e., burned area and fuel load) can be challenging to quantify accurately. Recent studies have demonstrated that the rate of biomass combustion is a linear function of fire radiative power (FRP), the instantaneous radiative energy released from actively burning fires, which provides a novel pathway to estimate BBE. To obtain accurate and timely BBE estimates for near real-time applications (i.e., air quality forecast), the satellite FRP-based method first requires a reliable biomass combustion coefficient that converts fire radiative energy (FRE), the temporal integration of FRP, to biomass consumption. The combustion coefficient is often derived in controlled small-scale fire experiments and is assumed a constant, whereas the coefficient based on satellite retrievals of FRP and atmospheric optical depth is suggested varying in a wide range. Undoubtedly, highly variable combustion coefficient results in large uncertainty of BBE estimates. Further, the FRP-based method also depends on high-spatiotemporal-resolution FRP retrievals that, however, are not available in any active fire products from

current polar-orbiting and geostationary satellites due to their sampling limitations. To address these challenges, this study first investigates the combustion coefficient for landscape-scale wildfires in the Conterminous United States (CONUS) by comparing FRE from the polar-orbiting Moderate Resolution Imaging Spectroradiometer (MODIS) and the Geostationary Operational Environmental Satellite system (GOES) with the Landsat-based biomass consumption. The results confirms that biomass consumption is a linear function of FRE for wildfires. The derived combustion coefficient is 0.374 kg · MJ^{-1} for GOES FRE, 0.266 kg · MJ^{-1} for MODIS FRE, and 0.320 kg · MJ^{-1} considering both GOES and MODIS FRE in the CONUS. Limited sensitivity analyses indicate that the combustion coefficient varies from 0.301 to 0.458 kg · MJ^{-1}, which is similar to the reported values in small fire experiments. Then, this study reconstructs diurnal FRP cycle to derive high-spatiotemporal-resolution FRP by fusing MODIS and GOES FRP retrievals and estimates hourly BBE at a 0.25°×0.3125° grid across the CONUS. The results indicate that the reconstructed diurnal FRP cycle varies significantly in magnitude and shape among 45 CONUS ecosystems. In the CONUS, the biomass burning annually releases approximately 690 Gg particulate matter (smaller than 2.5 μm in diameter, PM2.5). The diurnal-FRP-cycle-based BBE estimates compare well with BBE derived from Landsat burned areas in the western CONUS and with the hourly carbon monoxide emissions simulated using a biogeochemical model over the Rim Fire in California. Moreover, the BBE estimates show a similar seasonal variation to six existing BBE inventories but with variable magnitude. Finally, this study examines potential improvements in fires characterization capability of the Visible Infrared Imaging Radiometer Suite (VIIRS), which is the follow-on sensor of the MODIS sensor, for

integrating VIIRS FRP retrievals into the FRP-based method for BBE estimation in future work. The results indicate that the VIIRS fire characterization capability is similar across swath, whereas MODIS is strongly dependent on satellite view zenith angle. VIIRS FRP is generally comparable with contemporaneous MODIS FRP at continental scales and in most fire clusters. At 1-degree grid cells, the FRP difference between the two sensors is, on average, approximately 20% in fire-prone regions but varies significantly in fire-limited regions. In summary, this study attempts to enhance the capability of the FRP-based method by addressing challenges in its two parameters (combustion coefficient and FRP), which should help to improve estimation of BBE and advance our understanding of the effects of BBE on climate and air quality. This research has resulted in two published papers and one paper to be submitted to a peer-reviewed journal so far.

CHAPTER 1: Introduction

1.1. Overview of Biomass Burning in the Conterminous United States

Biomass burning is the combustion of organic matters, releasing energy stored by photosynthesis and generating smokes and water vapor (Pyne et al., 1996). It profoundly influences society, economy, the biosphere, the atmosphere, the Earth radiation budget, and climate. Wildfires directly cause fatalities and destroy properties, resulting in great economic losses (Thomas et al., 2015), increase soil erosion rates, triggering potential disastrous post-fire mudslide (Cannon & Gartner, 2005), and produce toxic pollutants that potentially contaminate water supplies, after rainfalls (Smith et al., 2011). In the biosphere, fire plays a critical role in shaping vegetation distributions and in determining vegetation species composition at broad scales (Bond & Keeley, 2005; Bond et al., 2005; Thonicke et al., 2001).

Furthermore, biomass burning is a significant source of atmospheric greenhouse gases and aerosols, which greatly affect climate and air quality. Global biomass burning annually releases, on average, approximately 2.2 Pg carbon emissions (approximately 23% of fossil-fuel carbon emissions in 2014 (Boden et al., 2017)), which are mainly contributed by fires in the tropics (84%) and boreal regions (9%) (van der Werf et al., 2017). As with greenhouse gases from burning fossil fuels, biomass-burning greenhouse gases (i.e., carbon dioxide, methane, etc.) warm the Earth by increasing absorption of solar radiation and the infrared radiation emitted from Earth surface (Jacobson, 2014). The smoke aerosols (i.e., particulates) reflect solar radiation (Kaufman et al., 2002), significantly influence cloud-formation processes and precipitation (Kaufman et al., 2002), reduce visibility in local ground and air transportations, and degrade regional air quality and threaten public health (Johnston et al., 2016; Lelieveld et al., 2015).

Biomass burning is a global phenomenon. Lit naturally by lightning strikes or set accidentally and/or intentionally by humans, fire burns in most vegetated terrestrial areas with available fuels and conductive weather (Bowman et al., 2009). Analyses of long-term fire proxies (i.e. charcoal and tree rings) suggest that historical fire activity was mainly driven and constrained by climate and the climate-induced changes in vegetation during the past 21,000 years (Daniau et al., 2012; Marlon et al., 2013., Power et al., 2008), and was greatly influenced by human land use during the past 2000 years (Marlon et al., 2008). During the past three decades, the length of fire weather season has significantly increased in one-quarter of global vegetated lands (Jolly et al., 2015). However, satellite-based fire observations indicate that global fire activity has shown a general decreasing trend during the past decade (Andela et al., 2017; Earl & Simmonds, 2018), with an annual mean burned area of approximately 350 million hectares (Giglio et al., 2013). Nevertheless, global fire activity is projected to significantly increase at mid-to-high latitudes in North Hemisphere and decrease at low latitudes by the end of 21st century (Flannigan et al., 2013; Krawchuk et al., 2009; Moritz et al., 2012).

This research mainly focuses on biomass burning in the Conterminous United States (CONUS). In the CONUS, fire mainly burns in the Southeast, the central-to-south parts of the great plain, and the West (Figure 1-1); whereas fire is very limited in the Northeast where burnings were widespread and frequent historically (Pyne, 1982). During a year, burning starts in the Southeastern CONUS in January and February, then moves northward, especially in Kansas and Oklahoma States, from March to May, and continues to migrate to most regions of the Western CONUS during summer months, and

finally returns to the Southeastern CONUS during late autumn and winter months (Figure 1-1a, b).

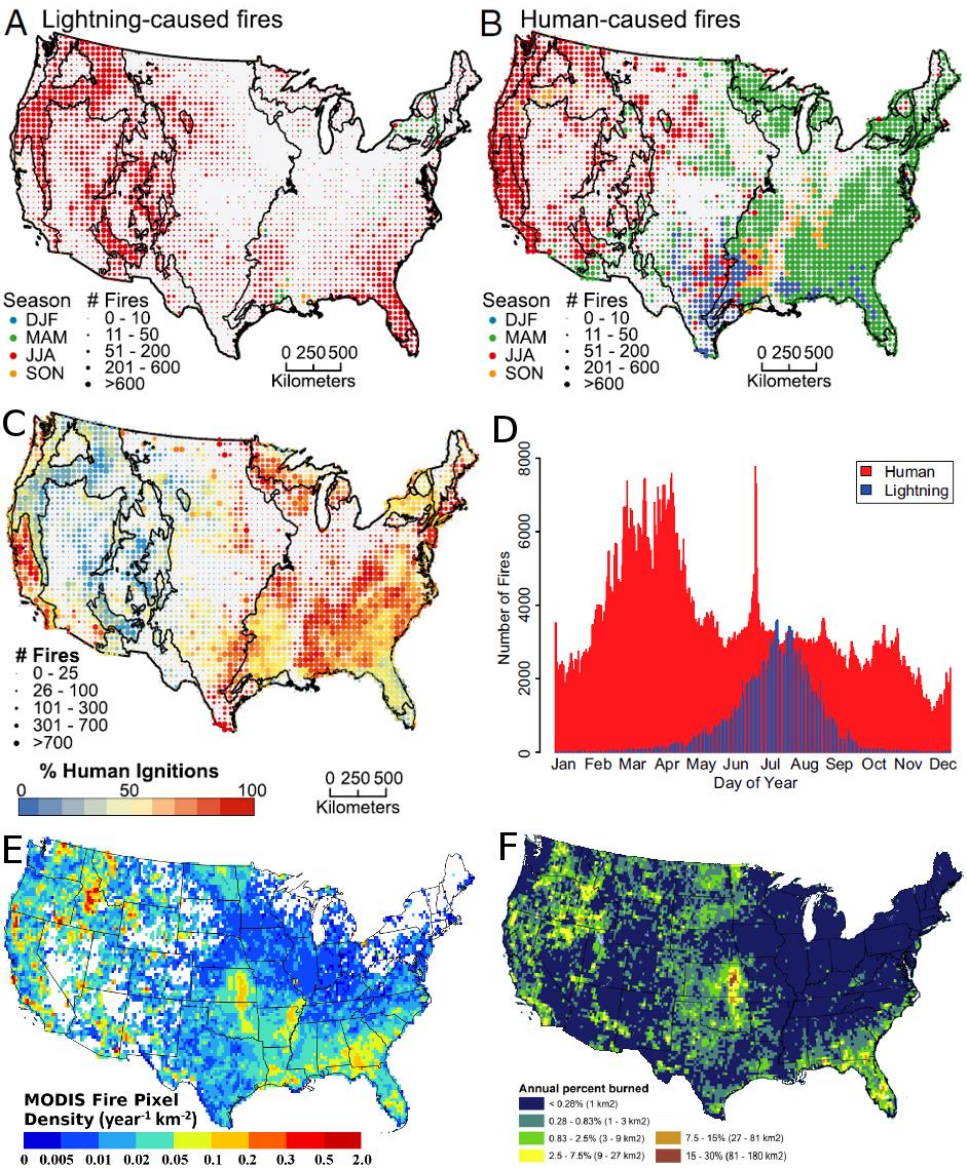

Figure 1-1. Spatiotemporal patterns of biomass burning in the CONUS. (A) Spatiotemporal pattern of the lightning-caused fires. (B) Spatiotemporal pattern of the human-caused fires. (C) Spatial distribution of the percentage of fires ignited by humans. (D) Seasonality of the lightning-caused and human-caused fires. (Note that (a-d) are copied from Balch et al. (2017) that is based on 20-year fire records from state and federal agencies from 1992-2012 (Short, 2014)). (E) The mean annual density (units: count · year^{-1} · km^{-2}) of 1-km MODIS (Terra and Aqua satellites) active fire detections at

a 0.25°×0.25° grid cell from 2002-2016. (F) The 30-m Landsat-based mean annual total burned area from 1984 to 2013 (copied from Hawbaker et al. (2017)).

Humans purposefully and/or accidentally cause most fires, and lightning strikes naturally ignite the rest in the CONUS (Figure 1-1c, d). In the past two decades, humans are responsible for approximately 84% of all fires, whereas the lightning strikes only account for a small portion (Balch et al., 2017). The lightning-caused fires mainly occur during summer months in the Western CONUS, especially in the forest-dominated mountainous regions. In contrast, human-caused fires occur throughout the entire year across most regions of the CONUS, especially in the Eastern CONUS because humans manage fire for a variety of purposes. Farmers set fires to clear agriculture residuals (i.e., rice in California and South Mississippi Valley, sugarcane in Lousiana and Florida, etc.) after harvest and before planting new crops (Baucum et al., 2002; Kross et al., 2008; Miller et al., 2010). Ranchers burn dead biomass in pastures (i.e., tall grass in the Flint Hills in Kansas and Oklahoma) to promote growth of new grasses for grazing (Fuhlendorf & Engle, 2004). The U.S. Forest Service employs prescribed fires to reduce fuel loads and fuel continuity to decrease wildfire risk (Pollet & Omi, 2002), to enhance wildlife habitats (Beck et al., 2009), to restore the fire-adapted ecosystems (Allen et al., 2002; Baker, 2006), and to control invasive plant species (Keeley, 2006) in the public lands.

Fire regimes in the CONUS have varied greatly in the past century due to human activity and climate change. Since the start of U.S. Forest Service in 1905 for the purpose of controlling and combating wildfires, the annual total number of fires and total burned

area had decreased, reaching the lowest in the late 1960s (Littell et al., 2009; Schoennagel et al., 2004). Meanwhile, extensive exclusion and suppression of wildfires promoted unnatural fuel accumulation (Dodge, 1972; Schoennagel et al., 2004). In the past several decades, enhanced fuel aridity (Abatzoglou & Williams, 2016) and lengthened fire weather seasons (Jolly et al., 2015) due to increase in temperature and water vapor deficit have resulted in significantly increasing larger and severer wildfires (Dennison et al., 2014; Donovan et al., 2017) and longer fire seasons (Westerling 2006, 2016) in the Western CONUS, especially in forests. The fire suppression cost has increased by approximately 10 times (not considering the inflation rate of US dollar) in the past three decades and reached the historically highest cost of approximately three billion US dollars in 2017 (National Interagency Fire Center; https://www.nifc.gov/fireInfo/fireInfo_documents/SuppCosts.pdf). During the same period, fires annually burn, on average, approximately 3.1 million hectares across the CONUS, and the annual total burned area increased by 50% every decade (Hwabaker et al., 2017) regardless of no significant change in the annual total number of fires (National Interagency Fire Center; https://www.nifc.gov/fireInfo/fireInfo_stats_totalFires.html). As the increase in annual burned area, the annually consumed biomass across the CONUS has increased approximately 2.87 Tg per year since 1995 (Zhang et al., 2014). In the CONUS, biomass burning annually releases, on average, approximately 18 Tg carbon emissions that account for only 1% of the annual global carbon emissions (van der Werf et al., 2017).

Although biomass burning in the CONUS is not a significant source of global biomass-burning emissions (BBE) compared to the tropical regions (i.e., Africa, South

America, and Equatorial Asia), it has been well recorded and observed for several decades, and extensively studied based on ground, airborne, and satellite datasets. These long-term fire datasets and study findings provide an essential basis for improving the existing methods and/or developing new methods for estimating biomass-burning emissions. This is the main reason why this study chooses the CONUS as the main region of interesting.

1.2. Challenges for Estimating Biomass-Burning Emissions

BBE estimation depends on availability and quality of fire-related datasets. Since the 1980s, BBE has been conventionally estimated as the product of burned area, the fuel loading, the fraction of biomass consumed, and emissions factors (Seiler and Crutzen, 1980), which is mathematically described in equation (1).

$$BBE = A \times B \times C \times EF \quad (1)$$

where BBE is the total mass of an emission species (units: g), A is the total burned area (units: m^2), B is fuel load per unit area ($g \cdot m^{-2}$), C is combustion completeness (unitless, the percentage change in fuel before and after burning), and EF is the emission factor of an emission species(units: $g \cdot kg^{-1}$, the mass of the emission species released from burning per unit biomass). Prior to the satellite era, BBE estimation had been limited to local small scales while the estimation at broad scales were of high uncertainty due to the scarcity of measurements and observations of the four parameters in equation (1). In general, BBE at regional-global scales was roughly estimated by extrapolating results from local experiments based on certain statistical information (i.e., population, food supplies, agriculture land requirements, etc.) (Seiler & Crutzen, 1980; Crutzen &

Andreae, 1990; Hao et al., 1990). In the satellite era, satellite observations of fires and vegetation properties have enabled the capability of mapping hotspots (Prins & Menzel, 1992; Justice et al., 2002) and burned area (Roy et al., 2002; Tansey et al., 2004) and estimating live fuel loads at broad scales (van der Werf et al., 2006; Zhang et al., 2008), which greatly improve the accuracy of BBE estimation. In particular, the availability of global fire products, i.e., the Moderate Resolution Imaging Spectroradiometer (MODIS) fire products, has promoted a variety of regional and global BBE products, like the widely used Global Fire Emissions Database (GFED) (van der Werf et al., 2017), for instance.

Although large improvements have been made to estimate the four parameters in the equation (1), particularly burned area (Mouillot et al., 2014), it is still challenging to accurately estimate BBE using the conventional method. The satellite-based burned area products are often affected by obscuration of cloud and tree canopy (Boschetti et al., 2004; Roy et al., 2008), and fuel loads based on vegetation indices miss dead fuels, as well as fuels under tree canopy. Moreover, it is very difficult to estimate spatially explicit combustion completeness in landscape wildfires (Veraverbeke & Hook, 2013). In addition, the widely used emissions factors measured in labs could significantly differ from those retrieved from the airborne-based observations of wildfires (Liu et al., 2017).

The satellite-retrieved fire radiative power (FRP), the instantaneous radiative energy released from fire, provides alternative ways to estimate BBE. Controlled fire experiments in lab and field demonstrated that FRP is linearly related to the rate of biomass combustion, and the mass of emissions is a function of the temporally integrated

FRP, termed fire radiative energy (FRE) (Freeborn et al., 2008; Kremens et al., 2012; Wooster et al., 2003). This relationship is described as following:

$$BBE = \left(FBCC \times FRE\right) \times EF = \left(FBCC \times \int_{t_1}^{t_2} FRPdt \right) \times EF \quad (2)$$

where BBE is the same as in equation (1), *FRE* is fire radiative energy (units: MJ) released from the fire during the time period from t_1 to t_2, *FBCC* is FRE biomass combustion coefficient (unitless) that converts FRE to the total biomass consumption, *EF* is the same as in equation (1), and *FRP* is fire radiative power (units: MW) that is calculated using the radiances of fire pixel and its non-fire ambient background at the 4-m band (Kaufman et al., 1998; Wooster et al., 2003). FRP retrievals from polar-orbiting and geostationary satellites are widely used to estimate regional and global BBE using equation (2) (Ellicott et al., 2009; Kumar et al., 2011; Kaiser et al., 2012; Vermote et al., 2009; Zhang et al., 2012).

The FRP-based method (equation (2)) has two advantages over the conventional method. First, the FRP-based method has fewer parameters, with the FRE estimate as a function of burned area, fuel load, and combustion completeness in equation (1). The reduction of the parameters potentially improves accuracy of BBE estimation. Second, satellites are able to detect small-sized fires that could be omitted by burned area products.

Accurate and timely estimation of BBE for near real-time applications (i.e., air quality forecast) requires reliable FBCC and high-spatiotemporal-resolution FRP estimates. The FBCC value is assumed to be fixed and has been derived by comparing

FRE estimates with measurements of biomass consumption in the controlled small-scale fire experiments, indicating a FBCC value ranging from 0.368 to 0.453 kg · MJ^{-1} (Freeborn et al., 2008; Kremens et al., 2012; Wooster et al., 2005). However, the FBCC value was suggested varying from 0.13 to 12.0 kg · MJ^{-1} based on satellite retrievals of FRP, atmospheric optical depth (AOD), and carbon monoxide (CO) (Kaiser et al., 2012; Konovalov et al., 2014; Zhang et al., 2012). Obviously, highly variable FBCC undoubtedly results in large discrepancies among different FRP-based BBE estimates (Zhang et al., 2012).

Further, estimation of high-spatiotemporal-resolution FRP is also challenging. None of the current polar-orbiting and geostationary satellites is able to provide high-spatiotemporal-resolution FRP due to sampling limitations. Sensors on board polar-orbiting satellites, e.g., Aqua and Terra MODIS, have relatively higher spatial resolution and thus they are able to detect relatively smaller and cooler fires compared to geostationary sensors. However, the polar-orbiting satellites are not able to capture diurnal variations of fire activity because they only observe the same location twice a day under cloud-free conditions. In contrast, sensors on board the geostationary satellites, e.g., the Imager on the Geostationary Operational Environmental Satellite system (GOES) and the Spinning Enhanced Visible and Infrared Imager (SEVIRI) on the Meteosat satellites, observe fires every 5-15 min but their coarse spatial resolutions limit the capability of detecting small and cool fires, resulting in the underestimation of FRP estimates. Two possible solutions have been attempted to simulate high-spatiotemporal-resolution FRP. For a given fire pixel or a group of clustering fire pixels, the first solution fits linear or Gaussian functions to daily FRP retrievals from the polar-orbiting satellites

to predict FRP of temporal gaps without observations (Boschetti & Roy, 2009; Ellicott et al., 2009; Vermote et al., 2009). This solution oversimplifies the diurnal fire variations and could result in large uncertainties in FRE and BBE estimates because fire is dynamic and varies largely with environmental conditions (i.e., weather, topography, and fuel characteristics) (Andela et al., 2015). On the other hand, to mitigate the underestimation of the geostationary satellite FRP, the second solution tries to adjust the geostationary satellite FRP retrievals using the contemporaneous FRP retrievals from the polar-orbiting satellite (Freeborn et al., 2009, 2011). However, this solution requires a large number of samples that need to be cumulated in large spatiotemporal windows (i.e., 5°grid and 15 min, or 1°grid and one month) (Freeborn et al., 2009), which hardly meets the requirements of operational and near real-time emissions inventories. Therefore, a new solution, which makes use of available FRP retrievals from both the polar-orbiting and geostationary satellites, is needed to produce high-temporal-resolution FRP that has equivalent accuracy to the polar-orbiting satellite FRP.

In addition, advancements of satellite sensors enhance the capability of detecting small and cool fires and thus potentially improve the accuracy of BBE estimates. The Visible Infrared Imaging Radiometer Suite (VIIRS), the successor of the 1-km MODIS sensor on board the NASA's Earth Observing Systems (EOS) Aqua and Terra satellites, has a mission to continue the long-term MODIS Earth science data records that include MODIS active fire data. The Aqua and Terra MODIS sensors have provided the most scientifically reliable global active fire products since the beginning of the 2000s (Giglio et al., 2016). However, the MODIS active fire detection capability decreases sharply as the pixel size decreases from ~1 km^2 at nadir to ~9.6 km^2 at the scan edge, resulting in

increasing omission error at large satellite view angles (Freeborn et al., 2011; Kumar et al., 2011). Thus, significant underestimates of FRE and BBE estimates are expected even if the high-temporal-resolution FRP with an equivalent accuracy to MODIS FRP were available. The first VIIRS sensor on board the Suomi National Polar-orbiting Partnership (Suomi NPP) satellite launched in October 2011 detects daily global fires using the 4-μm bands with a resolution of 375m and 750m separately (Csiszar et al., 2014; Schroeder et al., 2014). Because the VIIRS sensor applies an onboard aggregation scheme, the growth rate of the VIIRS pixel size with view angle is largely reduced relative to MODIS observations (Wolfe et al., 2013). Specifically, the pixel size of the VIIRS moderate-resolution bands (M-bands) generally increases along the scan direction from nominal 0.75 km at nadir to ~1.6 km at the scan edge but decreases abruptly at the ends of aggregation zones due to the application of different aggregation schemes in three aggregation zone (see Section 4.2.2 for details) (Wolfe et al., 2013). Therefore, the VIIRS sensor is theoretically able to detect many smaller and cooler fires than MODIS, and thus potentially improves the accuracy of FRE and BBE estimates. However, the discrepancies between the two sensors' capabilities of characterizing fire have not been systematically investigated at different spatial scales, except for a simple comparison at pixel level in a few sites (Oliva & Schroeder, 2015).

1.3. Research Aim, Objectives, and Hypotheses

The overall aim of this research is to improve the capability of the FRP-based method (equation (2)) for estimation of BBE by integrating FRP retrievals from polar-

orbiting and geostationary satellites. This aim is pursued through the following three objectives:

1. Investigate the factor of FBCC for landscape fires by linking the Landsat-burned-area-based biomass consumption to the MODIS and GOES FRE estimates for the CONUS wildfires.
2. Reconstruct diurnal FRP cycles by fusing MODIS and GOES FRP retrievals to estimate BBE released from wildfires across the CONUS.
3. Assess the similarities and discrepancies between FRP retrievals from the MODIS sensor and the advanced VIIRS sensor at a variety of spatial scales for the purpose of estimation of BBE.

To meet the above objectives, this research addressed the following three hypotheses.

Hypothesis #1: Satellite retrieved FRE estimates are linearly related to the biomass consumption at landscape scales with a factor of FRE biomass combustion coefficient (FBCC).

Hypothesis #1 builds on the findings that, in controlled fire experiments, the ground-based FRP is related to the rate of biomass combustion, and the FRE estimate is a function of total biomass consumption (Kaufman et al., 1996; Wooster et al., 2003). The reported FBCC varies from 0.368 to 0.453 $kg \cdot MJ^{-1}$, and it is assumed to be fixed (Freeborn et al., 2008; Kremens et al., 2012; Wooster et al., 2005). Compared to the fuel complexity in landscape wildfires, the range of fuel types considered in these

experiments was very limited, primary savanna grass (Wooster et al., 2005), evergreen tree species (Freeborn et al., 2008), and mixed oak (Kremens et al., 2012). At more synoptic scales, however, the FBCC, which is derived by comparing satellite-based FRP, atmospheric optical depth (AOD), and emissions retrievals, is suggested as varying from 0.13 to 12.0 kg · MJ^{-1} (Kaiser et al., 2012; Konovalov et al., 2014; Zhang et al., 2012).

Hypothesis #2: Diurnal FRP cycles can be reconstructed from polar-orbiting and geostationary satellites FRP retrievals to improve emissions estimation.

Hypothesis #2 builds on recent researches that applied MODIS FRP or geostationary satellite (SEVIRI and GOES) FRP to investigate diurnal FRP cycles in Africa (Andela et al., 2015; Roberts et al., 2009) and the globe (Vermote et al., 2009). However, the predefined diurnal cycles based on temporally sparse MODIS FRP could be oversimplified, which results in large uncertainties in FRE and BBE estimates. For instance, the assumed Gaussian diurnal cycle could lead to 200-400% underestimation of BBE over large fires in the Western CONUS (Saide et al., 2015) and the FRE estimates by superimposing Gaussian diurnal cycles on MODIS FRP are ~30% smaller than SEVIRI FRE in Africa (Vermote et al., 2009). Moreover, although geostationary satellites observe fires very frequently (i.e., every 15min), FRP retrievals from geostationary satellites are underestimated due to their coarse resolutions (Roberts et al., 2005). Therefore, integration of polar-orbiting and geostationary satellites FRP retrievals may help to overcome their temporal and spatial sampling limitations and help to build accurate diurnal FRP cycles. For instance, Freeborn et al. (2011) found that the simulated

FRP estimates based on MODIS and SEVIRI FRP retrievals improves SEVIRI FRE estimates by 30%.

Hypothesis #3: The 750-m VIIRS sensor has better capability of characterizing fires than the 1-km MODIS sensor.

Hypothesis #3 builds on the improvements of the VIIRS sensor compared to the MODIS sensor. First, VIIRS has higher spatial resolution than MODIS, and its pixel size is less affected by satellite view angle. As view angle increases from nadir to the scan edge, the pixel size of VIIRS moderate-resolution bands (M-bands) increases from ~0.56 to ~2.56 km^2 (Wolfe et al., 2013), and MODIS pixel size increases from ~1 to ~9.6 km^2 (Wolfe et al., 1998). Second, VIIRS is less likely to saturate in observing intense fires than MODIS. The VIIRS 4-μm M-band nominally saturates at 634 K at low gain settings (Csiszar et al., 2014) that is more than 100 K higher than the MODIS 4-μm band (500K) (Justice et al., 2002). Therefore, the higher spatial resolution and saturation temperature of the VIIRS sensor theoretically enhance its capability of characterizing both small cool and large intense fires.

1.4. Significance of the Research

The satellite retrieved FRP has shown promising potential to accurately estimate BBE in a timely manner for near real-time applications (Roberts et al., 2015; Zhang et al., 2012). The FRP-based method for estimation of BBE requires reliable FBCC (the factor that coverts FRE to biomass consumption) and high-spatiotemporal-resolution satellite FRP. However, the FBCC values derived in controlled fire experiments differ by a factor

of larger than 10 from those derived using satellite retrievals of FRP, AOD, and emissions (i.e., CO) (Zhang et al., 2012). Moreover, neither of the current polar-orbiting and geostationary satellites is able to provide the high-spatiotemporal-resolution FRP due to their sampling limitations (Freeborn et al., 2011). Although several solutions have been proposed to overcome these limitations, the FRP produced through these solutions hardly meet the requirements of near real-time applications (Reid et al., 2009). Thus, there is a great need to investigate the FBCC for landscape wildfires across large areas and to develop new methods that make use of available satellite FRP retrievals to simulate high-spatiotemporal-resolution FRP.

By addressing three hypotheses, this study potentially enhances the FRP-based method and thus improves the accuracy and application potential of BBE. First, investigation of the FBCC over a large number of wildfires shows statistical evidence to examine the existence of the fire-experiment-based empirical relationship between FRE and biomass consumption in wildfires and provides a FBCC value that converts satellite FRE to biomass consumption for wildfires in the CONUS, as well as other regions possibly. Second, development of a new method for the reconstruction of diurnal FRP cycle from MODIS and GOES FRP helps to simulate high-temporal-resolution FRP with an accuracy equivalent to MODIS FRP, which potentially produce the BBE that meet near real-time applications. Finally, understanding the advantage of the advanced VIIRS sensor over the MODIS sensor in characterizing fires provide key information on the degree to which the accuracy of the BBE estimates can be improved using data from the new sensor. In summary, the potentially accuracy-improved BBE estimates may significantly benefit models for near real-time applications (i.e., air quality forecast),

advance our understanding the role of BBE in climate, and assist governors to make sound smoke emissions-related policies.

1.5. Organization of the Dissertation

This dissertation has five chapters. Chapter 1 (this Chapter) provides an overview of biomass burning, especially in the CONUS, which reviews methods for estimation of BBE and frames the "aim, objectives, and hypotheses" that this research attempts to pursue and address. Then, Chapter 2 through Chapter 4 separately addresses the above three hypotheses. Finally, Chapter 5 concludes the whole research.

Chapter 2 addresses Hypothesis #1. It statistically compares the MODIS and GOES FRE estimates with the surface biomass consumption based on Landsat burned area over 445 wildfires across the CONUS, further reports the FBCC value for MODIS FRE, GOES FRE, and average FRE of the two sensors, and finally investigates the sensitivity of the FBCC to combustion completeness and fuel consumption.

Chapter 3 addresses Hypothesis #2. It proposes a method to reconstruct diurnal FRP cycles from the 15-min FRP estimates that are derived by fusing the 1-km MODIS and 4-km GOES FRP retrievals. Specifically, this chapter reports diurnal FRP climatology for 45 ecosystems, estimates hourly BBE at 0.25°×0.3125° grid cell across the CONUS, and evaluates the BBE estimates by comparing with existing BBE products.

Chapter 4 addresses Hypothesis #3. It statistically compares FRP retrievals from the advanced VIIRS sensor and the MODIS sensor from individual fire clusters to fire data on continental and global scales, and reports the similarities and discrepancies.

Chapter 5 presents major conclusions. It summarizes the key findings in the tests of three hypotheses and relates them back to the aim and specific objectives. Recommendations on possible future research directions are also discussed.

References

Abatzoglou, J. T., and A. P. Williams (2016), Impact of anthropogenic climate change on wildfire across western US forests, *Proceedings of the National Academy of Sciences*, *113*(42), 11770-11775, doi: https://doi.org/10.1073/pnas.1607171113.

Allen, C. D., M. Savage, D. A. Falk, K. F. Suckling, T. W. Swetnam, T. Schulke, P. B. Stacey, P. Morgan, M. Hoffman, and J. T. Klingel (2002), Ecological restoration of southwestern ponderosa pine ecosystems: A broad perspective, *Ecological Applications*, *12*(5), 1418-1433, doi: https://doi.org/10.1890/1051-0761(2002)012[1418:EROSPP]2.0.CO;2.

Andela, N., J. W. Kaiser, G. R. van der Werf, and M. J. Wooster (2015), New fire diurnal cycle characterizations to improve fire radiative energy assessments made from MODIS observations, *Atmos. Chem. Phys.*, *15*(15), 8831-8846, doi: https://doi.org/10.5194/acp-15-8831-2015.

Andela, N., D. C. Morton, L. Giglio, Y. Chen, G. R. van der Werf, P. S. Kasibhatla, R. S. DeFries, G. J. Collatz, S. Hantson, S. Kloster, D. Bachelet, M. Forrest, G. Lasslop, F. Li, S. Mangeon, J. R. Melton, C. Yue, and J. T. Randerson (2017), A human-driven decline in global burned area, *Science*, *356*(6345), 1356-1362, doi: https://doi.org/10.1126/science.aal4108.

Baker, W. L. (2006), Fire and Restoration of Sagebrush Ecosystems, *Wildlife Society Bulletin (1973-2006)*, *34*(1), 177-185.

Balch, J. K., B. A. Bradley, J. T. Abatzoglou, R. C. Nagy, E. J. Fusco, and A. L. Mahood (2017), Human-started wildfires expand the fire niche across the United States, *Proceedings of the National Academy of Sciences*, *114*(11), 2946-2951, doi: https://doi.org/10.1073/pnas.1617394114.

Baucum, L., R. Rice, and T. Schueneman (2002), An overview of Florida sugarcane, *Agronomy Department, Florida Cooperative Extension Service, Institute of Food and Agricultural Sciences, University of Florida. Publication# SS-AGR-232*.

Beck, J. L., J. W. Connelly, and K. P. Reese (2009), Recovery of Greater Sage-Grouse Habitat Features in Wyoming Big Sagebrush following Prescribed Fire, *Restoration Ecology*, *17*(3), 393-403, doi: https://doi.org/10.1111/j.1526-100X.2008.00380.x.

Boden, T. A., G. Marland, and R. J. Andres (2017), Global, Regional, and National Fossil-Fuel CO2 Emissions, edited by O. R. N. L. Carbon Dioxide Information Analysis Center, U.S. Department of Energy, Oak Ridge, Tenn., U.S.A., doi: https://doi.org/10.3334/CDIAC/00001_V2017.

Bond, W. J., and J. E. Keeley (2005), Fire as a global 'herbivore': the ecology and evolution of flammable ecosystems, *Trends in Ecology & Evolution*, *20*(7), 387-394, doi: https://doi.org/10.1016/j.tree.2005.04.025.

Bond, W. J., F. I. Woodward, and G. F. Midgley (2005), The global distribution of ecosystems in a world without fire, *New Phytologist*, *165*(2), 525-538, doi: https://doi.org/10.1111/j.1469-8137.2004.01252.x.

Boschetti, L., H. D. Eva, P. A. Brivio, and J. M. Grégoire (2004), Lessons to be learned from the comparison of three satellite-derived biomass burning products, *Geophysical Research Letters*, *31*(21), L21501, doi: https://doi.org/10.1029/2004GL021229.

Boschetti, L., and D. P. Roy (2009), Strategies for the fusion of satellite fire radiative power with burned area data for fire radiative energy derivation, *Journal of Geophysical Research: Atmospheres*, *114*(D20), D20302, doi: https://doi.org/10.1029/2008JD011645.

Bowman, D. M. J. S., J. K. Balch, P. Artaxo, W. J. Bond, J. M. Carlson, M. A. Cochrane, C. M. D'Antonio, R. S. DeFries, J. C. Doyle, S. P. Harrison, F. H. Johnston, J. E. Keeley, M. A. Krawchuk, C. A. Kull, J. B. Marston, M. A. Moritz, I. C. Prentice, C. I. Roos, A. C. Scott, T. W. Swetnam, G. R. van der Werf, and S. J. Pyne (2009), Fire in the Earth System, *Science*, *324*(5926), 481-484, doi: https://doi.org/10.1126/science.1163886.

Cannon, S. H., and J. E. Gartner (2005), Wildfire-related debris flow from a hazards perspective, in *Debris-flow hazards and related phenomena*, edited, pp. 363-385, Springer.

Crutzen, P. J., and M. O. Andreae (1990), Biomass Burning in the Tropics: Impact on Atmospheric Chemistry and Biogeochemical Cycles, *Science*, *250*(4988), 1669-1678, doi: https://doi.org/10.1126/science.250.4988.1669.

Csiszar, I., W. Schroeder, L. Giglio, E. Ellicott, K. P. Vadrevu, C. O. Justice, and B. Wind (2014), Active fires from the Suomi NPP Visible Infrared Imaging Radiometer Suite: Product status and first evaluation results, *Journal of*

Geophysical Research: Atmospheres, *119*(2), 2013JD020453, doi: https://doi.org/10.1002/2013JD020453.

Daniau, A. L., P. J. Bartlein, S. P. Harrison, I. C. Prentice, S. Brewer, P. Friedlingstein, T. I. Harrison-Prentice, J. Inoue, K. Izumi, J. R. Marlon, S. Mooney, M. J. Power, J. Stevenson, W. Tinner, M. Andrič, J. Atanassova, H. Behling, M. Black, O. Blarquez, K. J. Brown, C. Carcaillet, E. A. Colhoun, D. Colombaroli, B. A. S. Davis, D. D'Costa, J. Dodson, L. Dupont, Z. Eshetu, D. G. Gavin, A. Genries, S. Haberle, D. J. Hallett, G. Hope, S. P. Horn, T. G. Kassa, F. Katamura, L. M. Kennedy, P. Kershaw, S. Krivonogov, C. Long, D. Magri, E. Marinova, G. M. McKenzie, P. I. Moreno, P. Moss, F. H. Neumann, E. Norström, C. Paitre, D. Rius, N. Roberts, G. S. Robinson, N. Sasaki, L. Scott, H. Takahara, V. Terwilliger, F. Thevenon, R. Turner, V. G. Valsecchi, B. Vannière, M. Walsh, N. Williams, and Y. Zhang (2012), Predictability of biomass burning in response to climate changes, *Global Biogeochemical Cycles*, *26*(4), GB4007, doi: https://doi.org/10.1029/2011GB004249.

Dennison, P. E., S. C. Brewer, J. D. Arnold, and M. A. Moritz (2014), Large wildfire trends in the western United States, 1984–2011, *Geophysical Research Letters*, *41*(8), 2014GL059576, doi: https://doi.org/10.1002/2014GL059576.

Dodge, M. (1972), Forest Fuel Accumulation—A Growing Problem, *Science*, *177*(4044), 139-142, doi: https://doi.org/10.1126/science.177.4044.139.

Donovan, V. M., C. L. Wonkka, and D. Twidwell (2017), Surging wildfire activity in a grassland biome, *Geophysical Research Letters*, *44*(12), 5986-5993, doi: https://doi.org/10.1002/2017GL072901.

Earl, N., and I. Simmonds (2018), Spatial and Temporal Variability and Trends in 2001–2016 Global Fire Activity, *Journal of Geophysical Research: Atmospheres*, *123*(5), 2524-2536, doi: https://doi.org/10.1002/2017JD027749.

Ellicott, E., E. Vermote, L. Giglio, and G. Roberts (2009), Estimating biomass consumed from fire using MODIS FRE, *Geophysical Research Letters*, *36*(13), L13401, doi: https://doi.org/10.1029/2009GL038581.

Flannigan, M., A. S. Cantin, W. J. de Groot, M. Wotton, A. Newbery, and L. M. Gowman (2013), Global wildland fire season severity in the 21st century, *Forest Ecology and Management*, *294*, 54-61, doi: https://doi.org/10.1016/j.foreco.2012.10.022.

Freeborn, P. H., M. J. Wooster, W. M. Hao, C. A. Ryan, B. L. Nordgren, S. P. Baker, and C. Ichoku (2008), Relationships between energy release, fuel mass loss, and trace gas and aerosol emissions during laboratory biomass fires, *Journal of Geophysical Research-Atmospheres*, *113*(D1), doi: https://doi.org/10.1029/2007jd008679.

Freeborn, P. H., M. J. Wooster, and G. Roberts (2011), Addressing the spatiotemporal sampling design of MODIS to provide estimates of the fire radiative energy emitted from Africa, *Remote Sensing of Environment*, *115*(2), 475-489, doi: https://doi.org/10.1016/j.rse.2010.09.017.

Freeborn, P. H., M. J. Wooster, G. Roberts, B. D. Malamud, and W. Xu (2009), Development of a virtual active fire product for Africa through a synthesis of geostationary and polar orbiting satellite data, *Remote Sensing of Environment*, *113*(8), 1700-1711, doi: https://doi.org/10.1016/j.rse.2009.03.013.

Fuhlendorf, S. D., and D. M. Engle (2004), Application of the fire–grazing interaction to restore a shifting mosaic on tallgrass prairie, *Journal of Applied Ecology*, *41*(4), 604-614, doi: https://doi.org/10.1111/j.0021-8901.2004.00937.x.

Giglio, L., J. T. Randerson, and G. R. van der Werf (2013), Analysis of daily, monthly, and annual burned area using the fourth-generation global fire emissions database (GFED4), *Journal of Geophysical Research: Biogeosciences*, *118*(1), 317-328, doi: https://doi.org/10.1002/jgrg.20042.

Giglio, L., W. Schroeder, and C. O. Justice (2016), The collection 6 MODIS active fire detection algorithm and fire products, Remote Sensing of Environment, 178, 31-41, doi: https://doi.org/10.1016/j.rse.2016.02.054.

Hao, W. M., M.-H. Liu, and P. J. Crutzen (1990), Estimates of Annual and Regional Releases of CO2 and Other Trace Gases to the Atmosphere from Fires in the Tropics, Based on the FAO Statistics for the Period 1975–1980, in *Fire in the Tropical Biota: Ecosystem Processes and Global Challenges*, edited by J. G. Goldammer, pp. 440-462, Springer Berlin Heidelberg, Berlin, Heidelberg, doi: https://doi.org/10.1007/978-3-642-75395-4_20.

Hawbaker, T. J., M. K. Vanderhoof, Y.-J. Beal, J. D. Takacs, G. L. Schmidt, J. T. Falgout, B. Williams, N. M. Fairaux, M. K. Caldwell, J. J. Picotte, S. M. Howard, S. Stitt, and J. L. Dwyer (2017), Mapping burned areas using dense time-series of Landsat data, *Remote Sensing of Environment*, *198*, 504-522, doi: https://doi.org/10.1016/j.rse.2017.06.027.

Jacobson, M. Z. (2014), Effects of biomass burning on climate, accounting for heat and moisture fluxes, black and brown carbon, and cloud absorption effects, *Journal of*

Geophysical Research: Atmospheres, *119*(14), 2014JD021861, doi: https://doi.org/10.1002/2014JD021861.

Jolly, W. M., M. A. Cochrane, P. H. Freeborn, Z. A. Holden, T. J. Brown, G. J. Williamson, and D. M. J. S. Bowman (2015), Climate-induced variations in global wildfire danger from 1979 to 2013, *Nat Commun*, *6*, doi: https://doi.org/10.1038/ncomms8537.

Justice, C. O., L. Giglio, S. Korontzi, J. Owens, J. T. Morisette, D. Roy, J. Descloitres, S. Alleaume, F. Petitcolin, and Y. Kaufman (2002), The MODIS fire products, *Remote Sensing of Environment*, *83*(1–2), 244-262, doi: https://doi.org/10.1016/S0034-4257(02)00076-7.

Kaiser, J. W., A. Heil, M. O. Andreae, A. Benedetti, N. Chubarova, L. Jones, J. J. Morcrette, M. Razinger, M. G. Schultz, M. Suttie, and G. R. van der Werf (2012), Biomass burning emissions estimated with a global fire assimilation system based on observed fire radiative power, *Biogeosciences*, *9*(1), 527-554, doi: https://doi.org/10.5194/bg-9-527-2012.

Kaufman, Y. J., C. O. Justice, L. P. Flynn, J. D. Kendall, E. M. Prins, L. Giglio, D. E. Ward, W. P. Menzel, and A. W. Setzer (1998), Potential global fire monitoring from EOS-MODIS, *Journal of Geophysical Research: Atmospheres*, *103*(D24), 32215-32238, doi: https://doi.org/10.1029/98JD01644.

Kaufman, Y. J., D. Tanre, and O. Boucher (2002), A satellite view of aerosols in the climate system, *Nature*, *419*(6903), 215-223.

Keeley, J. E. (2006), Fire Management Impacts on Invasive Plants in the Western United States, *Conservation Biology*, *20*(2), 375-384, doi: https://doi.org/10.1111/j.1523-1739.2006.00339.x.

Konovalov, I. B., E. V. Berezin, P. Ciais, G. Broquet, M. Beekmann, J. Hadji-Lazaro, C. Clerbaux, M. O. Andreae, J. W. Kaiser, and E. D. Schulze (2014), Constraining CO2 emissions from open biomass burning by satellite observations of co-emitted species: a method and its application to wildfires in Siberia, *Atmos. Chem. Phys.*, *14*(19), 10383-10410, doi: https://doi.org/10.5194/acp-14-10383-2014.

Krawchuk, M. A., M. A. Moritz, M.-A. Parisien, J. Van Dorn, and K. Hayhoe (2009), Global Pyrogeography: the Current and Future Distribution of Wildfire, *PLoS ONE*, *4*(4), e5102, doi: https://doi.org/10.1371/journal.pone.0005102.

Kremens, R. L., M. B. Dickinson, and A. S. Bova (2012), Radiant flux density, energy density and fuel consumption in mixed-oak forest surface fires, *International Journal of Wildland Fire*, *21*(6), 722-730, doi: https://doi.org/10.1071/WF10143.

Kross, J. P., R. M. Kaminski, K. J. Reinecke, and A. T. Pearse (2008), Conserving Waste Rice for Wintering Waterfowl in the Mississippi Alluvial Valley, *Journal of Wildlife Management*, *72*(6), 1383-1387, doi: https://doi.org/10.2193/2007-226.

Kumar, S. S., D. P. Roy, L. Boschetti, and R. Kremens (2011), Exploiting the power law distribution properties of satellite fire radiative power retrievals: A method to estimate fire radiative energy and biomass burned from sparse satellite observations, *Journal of Geophysical Research: Atmospheres*, *116*(D19), D19303, doi: https://doi.org/10.1029/2011JD015676.

Lelieveld, J., J. S. Evans, M. Fnais, D. Giannadaki, and A. Pozzer (2015), The contribution of outdoor air pollution sources to premature mortality on a global scale, *Nature*, *525*(7569), 367-371, doi: https://doi.org/10.1038/nature15371.

Littell, J. S., D. McKenzie, D. L. Peterson, and A. L. Westerling (2009), Climate and wildfire area burned in western U.S. ecoprovinces, 1916–2003, *Ecological Applications*, *19*(4), 1003-1021, doi: https://doi.org/10.1890/07-1183.1.

Liu, X., L. G. Huey, R. J. Yokelson, V. Selimovic, I. J. Simpson, M. Müller, J. L. Jimenez, P. Campuzano-Jost, A. J. Beyersdorf, D. R. Blake, Z. Butterfield, Y. Choi, J. D. Crounse, D. A. Day, G. S. Diskin, M. K. Dubey, E. Fortner, T. F. Hanisco, W. Hu, L. E. King, L. Kleinman, S. Meinardi, T. Mikoviny, T. B. Onasch, B. B. Palm, J. Peischl, I. B. Pollack, T. B. Ryerson, G. W. Sachse, A. J. Sedlacek, J. E. Shilling, S. Springston, J. M. St. Clair, D. J. Tanner, A. P. Teng, P. O. Wennberg, A. Wisthaler, and G. M. Wolfe (2017), Airborne measurements of western U.S. wildfire emissions: Comparison with prescribed burning and air quality implications, *Journal of Geophysical Research: Atmospheres*, *122*(11), 6108-6129, doi: https://doi.org/10.1002/2016JD026315.

Marlon, J. R., P. J. Bartlein, C. Carcaillet, D. G. Gavin, S. P. Harrison, P. E. Higuera, F. Joos, M. J. Power, and I. C. Prentice (2008), Climate and human influences on global biomass burning over the past two millennia, *Nature Geosci*, *1*(10), 697-702, doi: https://doi.org/10.1038/ngeo313.

Marlon, J. R., P. J. Bartlein, A.-L. Daniau, S. P. Harrison, S. Y. Maezumi, M. J. Power, W. Tinner, and B. Vanniére (2013), Global biomass burning: a synthesis and

review of Holocene paleofire records and their controls, *Quaternary Science Reviews*, *65*, 5-25, doi: https://doi.org/10.1016/j.quascirev.2012.11.029.

Miller, M. R., J. D. Garr, and P. S. Coates (2010), Changes in the Status of Harvested Rice Fields in the Sacramento Valley, California: Implications for Wintering Waterfowl, *Wetlands*, *30*(5), 939-947, doi: https://doi.org/10.1007/s13157-010-0090-2.

Moritz, M. A., M.-A. Parisien, E. Batllori, M. A. Krawchuk, J. Van Dorn, D. J. Ganz, and K. Hayhoe (2012), Climate change and disruptions to global fire activity, *Ecosphere*, *3*(6), art49, doi: https://doi.org/10.1890/ES11-00345.1.

Mouillot, F., M. G. Schultz, C. Yue, P. Cadule, K. Tansey, P. Ciais, and E. Chuvieco (2014), Ten years of global burned area products from spaceborne remote sensing—A review: Analysis of user needs and recommendations for future developments, *International Journal of Applied Earth Observation and Geoinformation*, *26*, 64-79, doi: https://doi.org/10.1016/j.jag.2013.05.014.

Pollet, J., and P. N. Omi (2002), Effect of thinning and prescribed burning on crown fire severity in ponderosa pine forests, *International Journal of Wildland Fire*, *11*(1), 1-10, doi: https://doi.org/10.1071/WF01045.

Power, M. J., J. Marlon, N. Ortiz, P. J. Bartlein, S. P. Harrison, F. E. Mayle, A. Ballouche, R. H. W. Bradshaw, C. Carcaillet, C. Cordova, S. Mooney, P. I. Moreno, I. C. Prentice, K. Thonicke, W. Tinner, C. Whitlock, Y. Zhang, Y. Zhao, A. A. Ali, R. S. Anderson, R. Beer, H. Behling, C. Briles, K. J. Brown, A. Brunelle, M. Bush, P. Camill, G. Q. Chu, J. Clark, D. Colombaroli, S. Connor, A. L. Daniau, M. Daniels, J. Dodson, E. Doughty, M. E. Edwards, W. Finsinger, D.

Foster, J. Frechette, M. J. Gaillard, D. G. Gavin, E. Gobet, S. Haberle, D. J. Hallett, P. Higuera, G. Hope, S. Horn, J. Inoue, P. Kaltenrieder, L. Kennedy, Z. C. Kong, C. Larsen, C. J. Long, J. Lynch, E. A. Lynch, M. McGlone, S. Meeks, S. Mensing, G. Meyer, T. Minckley, J. Mohr, D. M. Nelson, J. New, R. Newnham, R. Noti, W. Oswald, J. Pierce, P. J. H. Richard, C. Rowe, M. F. Sanchez Goñi, B. N. Shuman, H. Takahara, J. Toney, C. Turney, D. H. Urrego-Sanchez, C. Umbanhowar, M. Vandergoes, B. Vanniere, E. Vescovi, M. Walsh, X. Wang, N. Williams, J. Wilmshurst, and J. H. Zhang (2008), Changes in fire regimes since the Last Glacial Maximum: an assessment based on a global synthesis and analysis of charcoal data, *Clim Dyn*, *30*(7-8), 887-907, doi: https://doi.org/10.1007/s00382-007-0334-x.

Prins, E. M., and W. P. Menzel (1992), Geostationary satellite detection of biomass burning in South America, *International Journal of Remote Sensing*, *13*(15), 2783-2799, doi: https://doi.org/10.1080/01431169208904081.

Pyne, S. J. (1982), *Fire in America: a cultural history of wildland and rural fire*, University of Washington Press.

Pyne, S. J., P. L. Andrews, and R. D. Laven (1996), *Introduction to wildland fire*, John Wiley and Sons.

Reid, J. S., E. J. Hyer, E. M. Prins, D. L. Westphal, Z. Jianglong, W. Jun, S. A. Christopher, C. A. Curtis, C. C. Schmidt, D. P. Eleuterio, K. A. Richardson, and J. P. Hoffman (2009), Global Monitoring and Forecasting of Biomass-Burning Smoke: Description of and Lessons From the Fire Locating and Modeling of Burning Emissions (FLAMBE) Program, *Selected Topics in Applied Earth*

Observations and Remote Sensing, IEEE Journal of, *2*(3), 144-162, doi: https://doi.org/10.1109/JSTARS.2009.2027443.

Roberts, G., M. J. Wooster, G. L. W. Perry, N. Drake, L. M. Rebelo, and F. Dipotso (2005), Retrieval of biomass combustion rates and totals from fire radiative power observations: Application to southern Africa using geostationary SEVIRI imagery, Journal of Geophysical Research: Atmospheres, 110(D21), D21111, doi: https://doi.org/10.1029/2005JD006018.

Roberts, G., M. J. Wooster, and E. Lagoudakis (2009), Annual and diurnal african biomass burning temporal dynamics, *Biogeosciences*, *6*(5), 849-866, doi: https://doi.org/10.5194/bg-6-849-2009.

Roberts, G., M. J. Wooster, W. Xu, P. H. Freeborn, J. J. Morcrette, L. Jones, A. Benedetti, H. Jiangping, D. Fisher, and J. W. Kaiser (2015), LSA SAF Meteosat FRP products – Part 2: Evaluation and demonstration for use in the Copernicus Atmosphere Monitoring Service (CAMS), *Atmos. Chem. Phys.*, *15*(22), 13241-13267, doi: https://doi.org/10.5194/acp-15-13241-2015.

Roy, D. P., L. Boschetti, C. O. Justice, and J. Ju (2008), The collection 5 MODIS burned area product — Global evaluation by comparison with the MODIS active fire product, Remote Sensing of Environment, 112(9), 3690-3707, doi: https://doi.org/10.1016/j.rse.2008.05.013.

Roy, D. P., P. E. Lewis, and C. O. Justice (2002), Burned area mapping using multi-temporal moderate spatial resolution data—a bi-directional reflectance model-based expectation approach, *Remote Sensing of Environment*, *83*(1), 263-286, doi: https://doi.org/10.1016/S0034-4257(02)00077-9.

Schoennagel, T., T. T. Veblen, and W. H. Romme (2004), The Interaction of Fire, Fuels, and Climate across Rocky Mountain Forests, *BioScience, 54*(7), 661-676, doi: https://doi.org/10.1641/0006-3568(2004)054(0661:TIOFFA)2.0.CO;2.

Seiler, W., and P. Crutzen (1980), Estimates of gross and net fluxes of carbon between the biosphere and the atmosphere from biomass burning, *Climatic Change*, *2*(3), 207-247, doi: https://doi.org/10.1007/BF00137988.

Short, K. C. (2014), A spatial database of wildfires in the United States, 1992-2011, *Earth Syst. Sci. Data*, *6*(1), 1-27, doi: https://doi.org/10.5194/essd-6-1-2014.

Smith, H. G., G. J. Sheridan, P. N. J. Lane, P. Nyman, and S. Haydon (2011), Wildfire effects on water quality in forest catchments: A review with implications for water supply, *Journal of Hydrology*, *396*(1), 170-192, doi: https://doi.org/10.1016/j.jhydrol.2010.10.043.

Tansey, K., J. M. Grégoire, D. Stroppiana, A. Sousa, J. Silva, J. M. C. Pereira, L. Boschetti, M. Maggi, P. A. Brivio, R. Fraser, S. Flasse, D. Ershov, E. Binaghi, D. Graetz, and P. Peduzzi (2004), Vegetation burning in the year 2000: Global burned area estimates from SPOT VEGETATION data, *Journal of Geophysical Research: Atmospheres*, *109*(D14), doi: https://doi.org/10.1029/2003JD003598.

Thomas, D., D. Butry, S. Gilbert, D. Webb, and J. Fung (2017), The Costs and Losses of Wildfires *Rep.*

Thonicke, K., S. Venevsky, S. Sitch, and W. Cramer (2001), The role of fire disturbance for global vegetation dynamics: coupling fire into a Dynamic Global Vegetation Model, *Global Ecology and Biogeography*, *10*(6), 661-677, doi: https://doi.org/10.1046/j.1466-822X.2001.00175.x.

van der Werf, G. R., J. T. Randerson, L. Giglio, G. J. Collatz, P. S. Kasibhatla, and A. F. Arellano Jr (2006), Interannual variability in global biomass burning emissions from 1997 to 2004, *Atmos. Chem. Phys.*, *6*(11), 3423-3441, doi: https://doi.org/10.5194/acp-6-3423-2006.

Veraverbeke, S., and S. J. Hook (2013), Evaluating spectral indices and spectral mixture analysis for assessing fire severity, combustion completeness and carbon emissions, *International Journal of Wildland Fire*, *22*(5), 707-720, doi: https://doi.org/10.1071/WF12168.

Vermote, E., E. Ellicott, O. Dubovik, T. Lapyonok, M. Chin, L. Giglio, and G. J. Roberts (2009), An approach to estimate global biomass burning emissions of organic and black carbon from MODIS fire radiative power, *Journal of Geophysical Research: Atmospheres*, *114*(D18), D18205, doi: https://doi.org/10.1029/2008JD011188.

Westerling, A. L. (2016), Increasing western US forest wildfire activity: sensitivity to changes in the timing of spring, *Philos Trans R Soc Lond B Biol Sci*, *371*(1696), doi: https://doi.org/10.1098/rstb.2015.0178.

Westerling, A. L., H. G. Hidalgo, D. R. Cayan, and T. W. Swetnam (2006), Warming and Earlier Spring Increase Western U.S. Forest Wildfire Activity, *Science*, *313*(5789), 940-943, doi: https://doi.org/10.1126/science.1128834.

Wolfe, R. E., G. Lin, M. Nishihama, K. P. Tewari, J. C. Tilton, and A. R. Isaacman (2013), Suomi NPP VIIRS prelaunch and on-orbit geometric calibration and characterization, Journal of Geophysical Research: Atmospheres, 118(20), 2013JD020508, doi: https://doi.org/10.1002/jgrd.50873.

Wolfe, R. E., D. P. Roy, and E. Vermote (1998), MODIS land data storage, gridding, and compositing methodology: Level 2 grid, Geoscience and Remote Sensing, IEEE Transactions on, 36(4), 1324-1338, doi: https://doi.org/10.1109/36.701082.

Wooster, M. J., G. Roberts, G. L. W. Perry, and Y. J. Kaufman (2005), Retrieval of biomass combustion rates and totals from fire radiative power observations: FRP derivation and calibration relationships between biomass consumption and fire radiative energy release, *Journal of Geophysical Research-Atmospheres*, *110*(D24), doi: https://doi.org/10.1029/2005jd006318.

Wooster, M. J., B. Zhukov, and D. Oertel (2003), Fire radiative energy for quantitative study of biomass burning: derivation from the BIRD experimental satellite and comparison to MODIS fire products, *Remote Sensing of Environment*, *86*(1), 83-107, doi: https://doi.org/10.1016/S0034-4257(03)00070-1.

Zhang, X., S. Kondragunta, and D. P. Roy (2014), Interannual variation in biomass burning and fire seasonality derived from geostationary satellite data across the contiguous United States from 1995 to 2011, Journal of Geophysical Research: Biogeosciences, 119(6), 2013JG002518, doi: https://doi.org/10.1002/2013JG002518.

Zhang, X., S. Kondragunta, J. Ram, C. Schmidt, and H.-C. Huang (2012), Near-real-time global biomass burning emissions product from geostationary satellite constellation, *Journal of Geophysical Research-Atmospheres*, *117*, doi: https://doi.org/10.1029/2012jd017459.

Zhang, X., S. Kondragunta, C. Schmidt, and F. Kogan (2008), Near real time monitoring of biomass burning particulate emissions (PM2.5) across contiguous United States

using multiple satellite instruments, *Atmospheric Environment*, *42*(29), 6959-6972, doi: https://doi.org/10.1016/j.atmosenv.2008.04.060.

CHAPTER 2: Investigation of the Fire Radiative Energy Biomass Combustion Coefficient: A Comparison of Polar and Geostationary Satellite Retrievals over the Conterminous United States

Li, F., X. Zhang, S. Kondragunta, and D. P. Roy (2018), Investigation of the Fire Radiative Energy Biomass Combustion Coefficient: A Comparison of Polar and Geostationary Satellite Retrievals Over the Conterminous United States, *Journal of Geophysical Research: Biogeosciences*, *123*(2), 722-739, doi:10.1002/2017JG004279.

This chapter address Hypothesis #1: *Satellite retrieved FRE estimates are linearly related to the biomass consumption at landscape scales with a factor of FRE biomass combustion coefficient (FBCC).*

Abstract

Biomass burning substantially contributes to atmospheric aerosol and greenhouse gas emissions that influence climate and air quality. Fire radiative energy (FRE) (units: MJ) has been demonstrated to be linearly related to biomass consumption (units: kg) with potential for improving biomass burning emission estimation. The scalar constant, termed herein as the FRE biomass combustion coefficient (FBCC) (units: $kg \cdot MJ^{-1}$), which converts FRE to biomass consumption, has been estimated using field and laboratory experiments, varying from 0.368 to 0.453 $kg \cdot MJ^{-1}$. However, quite different FBCC values, especially for satellite-based approaches, have been reported. This study investigated the FBCC with respect to 445 wildfires that occurred from 2011 to 2012 across the Conterminous United States (CONUS) considering both polar-orbiting and geostationary satellite data. The FBCC was derived by comparing satellite FRE estimates with biomass consumption for the CONUS. FRE was estimated using observations from the Moderate Resolution Imaging Spectroradiometer (MODIS) and the Geostationary Operational Environmental Satellite (GOES); biomass consumption was estimated using Landsat-derived burned areas with fuel loadings from the Fuel Characteristic Classification System and using combustion completeness parameterized by Landsat burn severity and Fuel Characteristic Classification System fuelbed type. The reported results confirm the linearity of the empirical relationship between FRE and biomass consumption for wildfires. The CONUS FBCC was 0.374 $kg \cdot MJ^{-1}$ for GOES FRE, 0.266 $kg \cdot MJ^{-1}$ for MODIS FRE, and 0.320 $kg \cdot MJ^{-1}$ considering both GOES and MODIS FRE. Limited sensitivity analyses, comparing MODIS and GOES FRE with

biomass consumption estimated in three different ways, indicated that the FBCC varied from 0.301 to 0.458 kg · MJ^{-1}.

2.1. Introduction

Wildfires release globally significant amounts of aerosols, trace gases, and greenhouse gases that influence air quality, weather, and climate (Bowman et al., 2009; van der Werf et al., 2010). Researchers have devoted considerable efforts to modeling and estimating biomass-burning emissions over the last several decades. Pyrogenic emissions are modeled conventionally using information on the burned area, fuel load, combustion completeness (CC), and fuel emission factors (Seiler & Crutzen, 1980). These parameters can be challenging to quantify accurately. For example, burned area estimates can differ by several orders of magnitude (Boschetti et al., 2004; Kasischke et al., 2011; Randerson et al., 2012); fuel loadings may differ by more than 35% among different fuel data sets (Zhang et al., 2008); CC could vary by more than 40% with fuel moisture content in the same fuelbed (Hély et al., 2003); many emission factors also have an uncertainty of about 20–30% (Andreae & Merlet, 2001).

Top-down pyrogenic emission estimation methods have been developed that use satellite retrievals of the instantaneous radiative energy released from actively burning fires detected at the time of satellite overpass. The retrieved instantaneous radiative energy is termed the fire radiative power (FRP) (units: MW). The FRP is proportional to the rate of biomass consumption, and temporal integration of the FRP over the life of the fire provides an estimate of the fire radiative energy (FRE) (units: MJ), which has been shown to be linearly related to the total amount of fuel consumed by fire (Kaufman et al.,

1996; Wooster et al., 2003). A scalar constant is used to convert the FRE to the total amount of biomass consumed, termed, for convenience in this paper, the FRE biomass combustion coefficient (FBCC) (units: $kg \cdot MJ^{-1}$). The FRE-based emission estimation approach has been used to estimate biomass combustion from FRP retrieved from the polar-orbiting Moderate Resolution Imaging Spectroradiometer (MODIS) and the geostationary Spinning Enhanced Visible and Infrared Imager for active fires detected at regional to continental scales (Ellicott et al., 2009; Kaiser et al., 2012; Roberts & Wooster, 2008; Vermote et al., 2009; Zhang et al., 2012) and from the Geostationary Operational Environmental Satellites (GOES) across the Conterminous United States (CONUS) (Zhang et al., 2012; Zhang, Kondragunta, & Roy, 2014). The FBCC value is usually assumed to be fixed and has been derived by statistical comparison of FRE retrievals with biomass consumed measurements for prescribed fires lit in the field and under more controlled conditions in plume towers. Studies indicate that the FBCC has a value ranging from 0.368 to 0.453 $kg \cdot MJ^{-1}$ (Freeborn et al., 2008; Kremens et al., 2012; Wooster et al., 2005). However, the range of fuel types considered in these experiments was limited, primary savanna grass (Wooster et al., 2005); evergreen tree species including ponderosa pine, white pine, and Douglas fir (Freeborn et al., 2008); and mixed oak (Kremens et al., 2012). In addition, the scale of prescribed fires in the field experiments (1.8–64 m^2 plots; Kremens et al., 2012; Wooster et al., 2005) was much reduced compared with landscape wildland fires. At more synoptic scales, using satellite data and models, the FBCC is suggested as varying from 0.30 to 0.52 $kg \cdot MJ^{-1}$ in Siberia wildfires based on MODIS FRP and satellite-based carbon monoxide (CO) retrievals (Konovalov et al., 2014), as varying from 0.13 to 1.55 $kg \cdot MJ^{-1}$ based on comparison of

MODIS FRE with global biomass combustion estimates from the Global Fire Emissions Database (Kaiser et al., 2012), and as varying from 1.6 to 12.0 kg · MJ^{-1} (Zhang et al., 2012) based on the comparison of MODIS-based emissions coefficients and aerosol optical thickness data (Ichoku & Kaufman, 2005; Sofiev et al., 2009).

This study quantifies the FBCC at a landscape scale, across the CONUS, by comparing polar-orbiting (MODIS) and geostationary (GOES) satellite-retrieved FRE estimates with biomass combustion estimates for 445 wildland fire events from 2011 to 2012. The biomass consumption estimates were derived using Landsat 30 m burned area maps combined with fuel load information from the Fuel Characteristic Classification System (FCCS) and CC information parameterized with Landsat-derived burn severity estimates. The FBCC was estimated by linear regression of the biomass consumption estimates against the satellite FRE estimates. Sensitivity analyses were undertaken to examine the FBCC variation using the biomass consumptions calculated from a consistent CC in all burn severity classes and from a land-cover-driven approach endorsed for national emission estimation (Intergovernmental Panel on Climate Change (IPCC), 2006). The paper concludes with a discussion of the findings and an appropriate FBCC value for large area satellite FRE-based quantification of biomass combustion.

2.2. Methods and Data

2.2.1. Bottom-Up Estimation of Biomass Consumption

Biomass consumption is conventionally estimated as the product of the burned area, fuel load, and CC (Seiler & Crutzen, 1980). In this study, we also incorporate the burn severity and assume that burn severity is related positively to biomass consumption

for the same fuel type. This is reasonable as fires that burn more biomass are generally expected to have more severe postfire effects (Heward et al., 2013; Keeley, 2009; Smith & Wooster, 2005; Veraverbeke & Hook, 2013). The burn severity is a qualitative metric that reflects the degree of organic matter consumption from fire and relates to changes in living and dead biomass, soil exposure, fire byproducts (char and ash), and fire effects (e.g., scorch height) (Eidenshink et al., 2007; Keeley, 2009). Several of these parameters are not amenable to optical wavelength remote sensing and/or may not be related in a linear way to reflectance (Disney et al., 2011; Roy et al., 2006); however, satellite estimates of burn severity have been widely adopted (Meigs et al., 2009; Moody et al., 2008; Rocha & Shaver, 2011), although with variable results (French et al., 2008; Lentile et al., 2006). In this study, the biomass consumption in a burned area was estimated as

$$BC_{AMC} = \sum_{i=1}^{n} \sum_{k=1}^{3} A(i,k) M(i,k) C(i,k) \quad (1)$$

where BCAMC is biomass consumption (kg), for fuelbed category *i* and burn severity class *k*; *A(i, k)* is the area burned (km^2); *M(i, k)* is the fuel loading ($kg \cdot km^{-2}$); *C(i, k)* is the CC (unitless: 0–1); and n is the number of fuelbed categories, and there are three burn severity classes. The derivation of these four variables is described below.

2.2.1.1. Burned Area and Severity

Landsat data have been used for decades to map the spatial extent of burning and to characterize post-fire effects (Boschetti et al., 2015; Hawbaker et al., 2017; Lentile et al., 2006). In this study, data from the U.S. Monitoring Trends in Burn Severity (MTBS) project are used. The MTBS project uses Landsat 30 m Thematic Mapper and Enhanced

Thematic Mapper Plus data to map the burn perimeter and the burn severity for all burned areas >404 and >202 ha in the western and eastern CONUS, respectively (Eidenshink et al., 2007). The MTBS project produces 30 m burn severity maps (e.g., Figure 2-1) by visual interpretation of the temporal difference in the normalized burn ratio (NBR), defined as the difference between the Landsat near-infrared band (0.76–0.90 μm) and the shortwave-infrared band (2.08–2.35 μm) divided by their sum, and a relativized temporal NBR difference (Cocke et al., 2005; Epting et al., 2005; Key & Benson, 2005). The MTBS burn severity map is classified into low, moderate, or high severity classes, with an additional unburned or undetected low severity class and an increased greenness (increased post-fire vegetation response) class (Eidenshink et al., 2007). A mask of unprocessed areas (due to cloud obscuration or land not sensed by Landsat) is also provided.

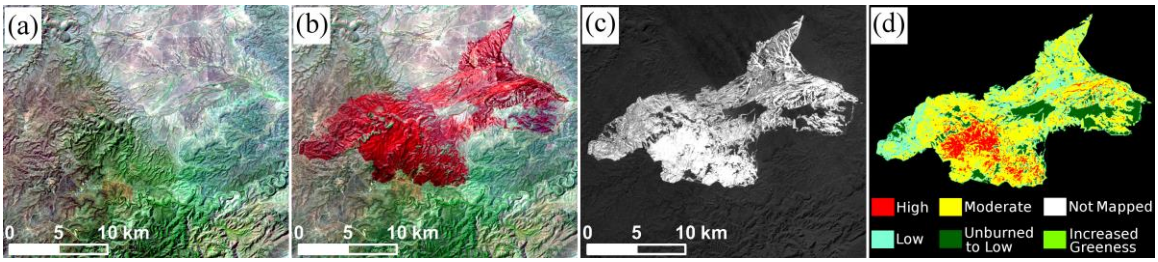

Figure 2-1. MTBS burn severity example derived from two Landsat images of the 2011 Last Chance fire, New Mexico, USA. (a) Prefire (23 April 2011) Landsat 5 Thematic Mapper false-color image (bands 7: 2.08–2.35 μm, 4: 0.76–0.90 μm, and 2: 0.52–0.60 μm). (b) Postfire (9 May 2011) false color image. (c) Differenced normalized burn ratio between the prefire and postfire normalized burn ratio. (d) MTBS burn severity map.

In this study, all the MTBS burned areas defined across the CONUS for 2011 and 2012 were obtained from the MTBS project (http://www.mtbs.gov/). A total of 2616

MTBS burned areas were available, although the final number of burned areas used in the study was reduced to 445 due to the filtering applied (section 2.2.3).

In equation (1) the area burned (km^2) for an MTBS burned area was derived as the product of the 30 m pixel area (9×10^{-4} km^2) and the sum of the number of 30 m pixels in each of the three (low, moderate, and high) burn severity classes and the fuelbed categories (see section 2.2.1.2). The unburned or undetected low severity and the increased greenness classes were excluded in the area burned calculation. The areas masked as unprocessed by MTBS were allocated to the three different severity classes (low, moderate, and high severity) weighted by the ratio of the area of a severity class to the total MTBS severity mapped area (as it is reasonable to assume that the burning conditions in the masked areas were similar to those in the processed areas).

2.2.1.2. Fuel Load

Development of fuel load maps is an area of active research, particularly at national to global scale (Pettinari & Chuvieco, 2016). The FCCS is commonly used because it includes a wide set of fuel physical characteristics that are not specific to a particular application or fire model. The United States FCCS 3.0 provides quantitative fuelbed information compiled from multiple sources including in situ fuel data sets, photographs, literature, and expert knowledge (Ottmar et al., 2007; Prichard et al., 2013). It defines a fuelbed as a set of fuel characteristics on the landscape that represent a distinct combustion environment. There are 250 fuelbeds, and each is divided into six strata with up to 18 categories: tree overstory, tree midstory, tree understory, total trees canopy, shrub, duff, nonwoody (dead and live) vegetation, sound woody debris (0-0.25,

0.25-1, 1-3, 3-9, 9-20, >20 inches), and rotten woody debris (3-9, 9-20, >20 inches) (Ottmar et al., 2007). Each stratum has one or more than one fuelbed category, and each category has common combustion characteristics. The FCCS data set has been used to model surface fire behavior, to predict fire potentials and effects (Cruz & Alexander, 2010; Lutes et al., 2009), and to estimate fuel consumption (FC) and fire emissions (Anjozian, 2009; Ottmar et al., 2006). In this study, the 30 m FCCS fuelbed map for year 2008 and the associated lookup table of fuel loadings per fuelbed category were obtained from the FCCS site (http://www.fs.fed.us/pnw/fera/fccs/maps.shtml).

In equation (1) the mean fuel loading of each fuelbed category and burn severity class was derived as

$$M(i,k) = \frac{\sum_{j=1}^{s} A(i,k,j)FL(i,k,j)}{A(i,k)} \quad (2)$$

where *M(i, k)* and *A(i, k)* are the mean fuel loading ($kg \cdot km^{-2}$) and the area burned (km^2), respectively, in burn severity class k and fuelbed category i over the burned area; j is one of the fuelbeds (a total number of *s*, $s \leqslant 250$) that include the fuelbed category *i*; and *A(i, k, j)* and *FL(i, k, j)* are the area burned (km^2) and the fuel loading ($kg \cdot km^{-2}$), respectively.

Change in the fuelbeds and associated fuel loadings between the production year of the FCCS map and the year of the burn due to land use change, disturbance (previous fires, insects, and drought, etc.), and vegetation seasonal phenology may introduce uncertainty into the biomass consumption estimates. Consequently, the sensitivity of FBCC to the biomass consumption was tested (section 2.2.5).

2.2.1.3. Combustion Completeness

The CC, that is, the proportion (0 to 1) of biomass consumed as a result of fire, is dependent on the fuel characteristics, including fuel moisture content, fuel arrangement, and fuel surface area to volume ratio, and environmental conditions (temperature, relative humidity, wind velocity, and slope) that affect the fire behavior and the fire duration (Hély et al., 2003; Ito & Penner, 2004; Ward et al., 1996). It is very challenging to obtain reliable spatially explicit CC maps at landscape scale (Veraverbeke & Hook, 2013). In the absence of any definitive spatially explicit CC data, published lookup tables that define CC as a function of the fuelbed category and burn severity class were used in this study (Table 2-1). The published CC values were obtained by qualitative field-based assessments of burn severity in the United States (Campbell et al., 2007; De Santis & Chuvieco, 2009; Ghimire et al., 2012; Key & Benson, 2006), typically inferred by human assessments and codified via the composite burn index (CBI) (Key & Benson, 2006) or the modified CBI (GeoCBI) (De Santis & Chuvieco, 2009). The CBI and GeoCBI indices provide a score from 0 to 3, based on fire manager and ecologist qualitative observations of a variety of post-fire effects including FC, change in soil color, foliage alteration, change in plant cover, canopy mortality, and scorch height (De Santis & Chuvieco, 2009; Key & Benson, 2006). The CBI and GeoCBI have been shown to be proportional to satellite-derived NBR and differenced normalized burn ratio values but with variable levels of statistical similarity (De Santis & Chuvieco, 2009; French et al., 2008; Keeley, 2009; Lentile et al., 2006; Veraverbeke & Hook, 2013) and as noted earlier some of the

post-fire effects may not be apparent in optical wavelength data and/or related in a linear way to reflectance (Disney et al., 2011; Roy et al., 2006).

Table 2-1. Combustion Completeness Lookup Table Defined as a Function of the Fuelbed Category and Burn Severity Class.

Fuelbed		Combustion Completeness			References
Stratum	Category	Low severity	Moderate severity	High severity	
Tree canopy	Overstory	0.20	0.45	0.75	Campbell et al., 2007 Ghimire et al., 2012
	Midstory	0.20	0.50	0.80	
	Understory	0.25	0.60	0.85	
Shrubs		0.30	0.70	0.90	Campbell et al., 2007 De Santis and Chuvieco., 2009 Key and Benson., 2006
Non-woody vegetation	Live	0.30	0.88	0.98	Campbell et al., 2007 De Santis and Chuvieco., 2009 Key and Benson., 2006
	Dead	0.70	0.90	1.00	
Duff	< 4 inches	0.50	0.80	0.95	Campbell et al., 2007 Ghimire et al., 2012
Sound woody debris	< 0.25 inches	0.70	0.90	1.00	Campbell et al., 2007 Ghimire et al., 2012
	0.25 – 1 inch	0.65	0.88	1.00	
	1 – 3 inches	0.60	0.80	0.85	
	3 – 9 inches	0.56	0.63	0.80	
	9 – 20 inches	0.56	0.63	0.80	
	> 20 inches	0.20	0.60	0.75	
Rotten woody debris	3 – 9 inches	0.56	0.63	0.80	Campbell et al., 2007 Ghimire et al., 2012
	9 – 20 inches	0.20	0.40	0.65	
	> 20 inches	0.20	0.40	0.65	

The CC values listed in Table 2-1 were applied for fuelbed category *i* and burn severity class k as equation (1) and assuming that the CC was the same for each fuelbed category and burn severity class across each MTBS burn and for all the burns considered across the CONUS. The sensitivity of FBCC to CC was also tested (section 2.2.5).

2.2.2. Top-Down Estimation of Biomass Consumption

Biomass consumption was derived from satellite (MODIS or GOES) estimates of FRE derived over each MTBS burned area (Wooster, 2002; Wooster et al., 2005) as

$$BC_{FRE} = \beta \ FRE \tag{3}$$

where BC_{FRE} is biomass consumption (kg), β is the FBCC (kg · MJ^{-1}), and the *FRE* is the MODIS or GOES FRE (MJ) defined as below.

2.2.2.1. MODIS FRE Estimation

The global Collection 5 MODIS 1-km Level 2 active fire product detects the 1 km location and time of fires that are burning at the time of overpass of the NASA Terra (MOD14) and Aqua (MYD14) satellites under cloud-free conditions (Giglio, 2013; Giglio et al., 2003). In this study, MOD14 and MYD14 active fire products for 2011–2012 were obtained from the NASA Reverb data portal (http://reverb.echo.nasa.gov/). The products contain for each 1-km pixel whether an active fire was detected, the detection confidence, the FRP (MW), the MODIS band 21 (3.660–3.840 μm) and band 31 (10.780–11.280 μm) blackbody temperatures (K), and average blackbody temperature in these two bands of the surrounding pixels. The MODIS FRP is calculated from band 21 brightness temperature based on a modeled

relationship developed in the Smoke, Clouds, and Radiation (SCAR) field experiments (Kaufman et al., 1998). If no MODIS active fire was detected then the surface status (land, water, cloud, or unknown) is defined. Only the nominal- and high-confidence fire detections were considered in this study to remove uncertain active fire detections that are classified as low-confidence detections in the Collection 5 MODIS active fire product (Giglio, 2013). Low-confidence detections are likely to be associated with the false alarms, for example, associated with solar heated charred ground surrounded by cool unburned areas. The Level 2 products are defined in the MODIS orbit geometry, corresponding to approximately 5 min of sensing in the track direction, covering an area of approximately 2,340 by 2,030 km in the across- and along-track directions, respectively. The MODIS scans ten 1-km pixel scan lines per mirror rotation over ±55° and the dimensions of the sensed pixel increase from ~1 km at nadir to ~2.01 km along track and ~4.83 km along scan at the scan edge (Wolfe et al., 1998, 2002). This geometry and the MODIS point spread function can result in the same single fire event being detected two or three times in consecutive scans (Freeborn et al., 2014; Peterson et al., 2013). Accordingly, detections in consecutive scans were considered as duplicated and were removed if they meet the following conditions: (1) detected at the same satellite view angles, (2) difference in observing time is less than 1 min, and (3) distance between two fire pixels is shorter than the along-track dimension of the fire pixels. After this filtering, there are, at CONUS latitudes, a maximum of four MODIS active fire detection opportunities (acquired approximately at 1:30, 10:30, 13:30, or 22:30 local time).

The MODIS FRP is underestimated at greater scan angle because the observed pixel size increases with scan angle (Freeborn et al., 2011; Kumar et al., 2011). To mitigate this effect, the FRP values were adjusted as

$$FRP_{adj} = FRP_{obs} \times \varepsilon \tag{4}$$

where FRP_{adj} is the adjusted FRP (MW), FRP_{obs} is the MODIS retrieved FRP (MW) stored in MOD14 or MYD14, and ε is a published adjustment factor (unitless) defined as a function of the scan angle (Freeborn et al., 2011).

The FRE was estimated from the adjusted MODIS FRP according to the established trapezoid method (Boschetti & Roy, 2009). The method can be applied to estimate FRE at a pixel level or for a cluster of pixels within a burned area. In this study, a cluster is considered as all the MODIS active fire pixels (and associated FRP values) within an MTBS burn perimeter over the lifetime of the fire. First, the cluster-level FRP was derived as

$$FRP(t_s) = \sum_{m=1}^{u} FRP_{adj}(m, t_s) \tag{5}$$

where $FRP(t_s)$ is the cluster-level FRP (MW) at time t_s when either MODIS sensor detected a fire, $FRP_{adj}(m, t_s)$ is the adjusted FRP of the mth fire pixel (equation (4)), and u is the total number of active fire pixels detected by MODIS at time t_s within an MTBS burned perimeter. Then, the MODIS FRE was derived as

$$FRE = \sum_{g=1}^{p} \sum_{s=1}^{q-1} \frac{\left[FRP(g, t_{s+1}) + FRP(g, t_s)\right](t_{s+1} - t_s)}{2} \tag{6}$$

where *FRE* is the MODIS FRE (MJ) released over the life of the fire in the MTBS burned area, q is total number ($q = 4$) of MODIS observing opportunities on the gth day, p is the total number of days that a fire event lasted, and FRP(g, t_s) is the cluster-level FRP (equation (5)) at time t_s (seconds from 12:00 a.m. local time) on the gth day. Note that FRP(g, t_s) was set to zero if there was no active fire detection on the gth day at time t_s.

2.2.2.2. GOES FRE Estimation

The GOES-West and GOES-East satellites each sense the CONUS every half an hour (or every 5–15 min in subregions) with a 4–7 km spatial resolution depending on the sensed CONUS location. The WildFire Automated Biomass Burning Algorithm (WF_ABBA Version 65) active fire product defines the location and timing of fires sensed by the GOES geostationary satellites (Prins et al., 1998; Schmidt & Prins, 2003). It provides the active fire detection date and time, geographic coordinate, pixel area, the FRP (MW), ecosystem type, and a quality flag. The FRP is calculated from the middle infrared band (3.9 μm) using the method developed in (Wooster et al., 2003). The WF_ABBA-based GOES fire products for 2011–2012 were obtained from the National Oceanic and Atmospheric Administration (NOAA) (http://satepsanone.nesdis.noaa.gov/pub/ FIRE/forPo/).

Successful GOES FRP retrievals are often temporally sparse due to cloud obscuration and sensor saturation (Prins et al., 1998). Therefore, the GOES FRP data were adjusted using the method described in (Zhang et al., 2012). The mean 15 min GOES FRP was defined independently for five ecosystems: forest, savanna, shrubland, grassland, and cropland, providing one mean CONUS FRP value every 15 min per

ecosystem. The five ecosystems cover all of the CONUS and were defined by the International Geosphere-Biosphere Programme ecosystem classification (Loveland et al., 2000). The resulting FRP ecosystem-specific 15 min diurnal climatologies were used to adjust the 2010–2012 good quality FRP values over each MTBS burned area using a least squares approach (Zhang et al., 2012). For brevity, we refer to the adjusted FRP time series data as the pixel-level GOES FRP data.

All the pixel-level GOES FRP data within an MTBS burn perimeter were considered as a cluster. The cluster-level GOES FRP over a burned area was calculated as

$$FRP(t) = \sum_{e=1}^{v} FRP(t,e) \tag{7}$$

where FRP(t) is the cluster-level GOES FRP (units: MW), FRP(t, e) is the eth pixel-level FRP (MW) at GOES observation time t, and v is the total number of GOES active fire detections at that time within the MTBS burned perimeter.

It is well established that MODIS is able to detect smaller and cooler fires than GOES due primarily to the higher spatial resolution and also dedicated active detection capabilities of MODIS (Roberts et al. 2005; Freeborn et al. 2009). Consequently, the following adjustment was applied:

$$FRP_{adj}(t) = FRP(t) + FRP_{offset}(t) \tag{8}$$

where $FRP_{adj}(t)$ is the adjusted GOES cluster-level FRP (MW); FRP(t) is the cluster-level GOES FRP calculated from equation (7), at GOES observation time t; and $FRP_{offset}(t)$ is an FRP offset value at time t derived from the difference between the cluster-level

MODIS and GOES FRP values (equations (5) and (7)) for that day. $FRP_{offset}(t)$ was determined based on the following steps. First the difference between the cluster-level MODIS FRP and the temporally closest cluster-level GOES FRP value was calculated for each MODIS observation during a 24 hr period, termed for brevity $FRP_{offset}(t_{MODIS})$, where t_{MODIS} is the MODIS observing local time (t_{MODIS} is approximately one of 1:30, 10:30, 13:30, or 22:30). If there were no MODIS FRP data over the burn in a 24 hr period then $FRP_{offset}(t)$ was set to zero for the period. If there were one or two MODIS FRP values in the 24 hr period then $FRP_{offset}(t)$ was set as the average of the $FRP_{offset}(t_{MODIS})$ values. If there were more than two MODIS FRP values then the $FRP_{offset}(t)$ was set to the first $FRP_{offset}(t_{MODIS})$ value for all times before the first MODIS observation in the day, or was linearly interpolated in time from the two closest $FRP_{offset}(t_{MODIS})$ values for times between the MODIS observations, or was set to the last $FRP_{offset}(t_{MODIS})$ value in the day for all times after the last MODIS observation. The results of this process are illustrated in Figure 2-2 for four cases showing different numbers of MODIS active fire detections in a 24-hour period.

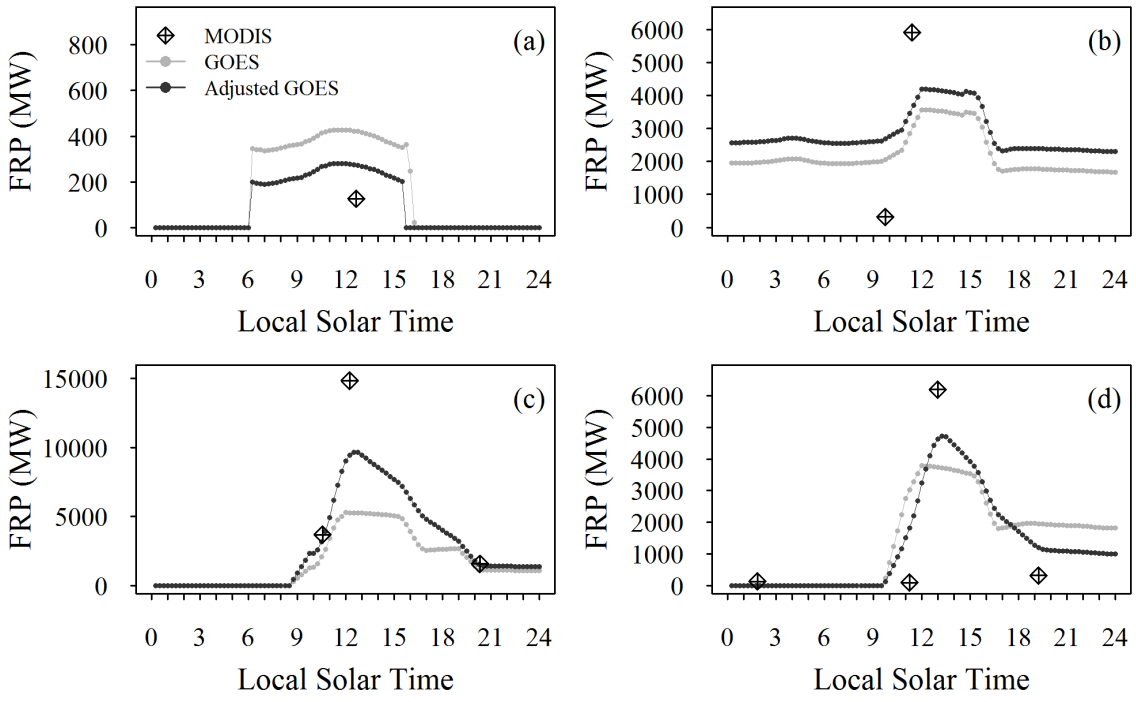

Figure 2-2. Illustration of the adjustment of cluster-level GOES FRP) over a 24 hr period for four examples where there are (a) one, (b) two, (c) three, and (d) four contemporaneous cluster-level MODIS FRP values. The gray and black filled cycles show the cluster-level GOES FRP before and after the adjustment, respectively, and the diamonds show the cluster-level MODIS FRP. The examples show satellite data for 23 August, 27 August, 30 July, and 1 September 2012, respectively, acquired over the Halstead fire, Idaho, USA.

The FRE was estimated from the adjusted GOES FRP for each MTBS burned area as

$$FRE = \sum_{d=1}^{n} \sum_{t=1}^{96} \left[FRP_{adj}(t) \times 900 \right] \quad (9)$$

where *FRE* is the GOES FRE (MJ) released over the life of the fire in the MTBS burned area, *n* is the total number of days that the fire event lasted, and $FRP_{adj}(t)$ is defined as equation (8) for every 15 min (corresponding to 900 s) and there are 96 15-min periods

each day (24 hr). This implicitly assumes that a fire event burned consistently in the same way in each 15 min period (Zhang et al., 2012).

2.2.3. Processing of Data to Ensure Contemporaneous Observations

The MTBS burned area perimeters were intersected spatially with the locations of the MODIS and GOES active fire detections so that the satellite FRE could be compared with the Landsat-derived biomass consumption (equation (1)) for each MTBS burned area. Specifically, the satellite active fire detections were projected into the Universal Transverse Mercator (UTM) projection defining the MTBS fire perimeter data. Each burned area perimeter was buffered outward by 5 km to accommodate for the coarser spatial resolution of the 4 km GOES active fire detections relative to the 1 km MODIS detections. All the active fire detections located within each buffered perimeter were considered within 80 days after the date of fire ignition defined in the MTBS burn metadata. An 80-day temporal threshold was used as several extensive CONUS fires lasted up to two months. This process is illustrated in Figure 2-3, which shows an example where active fire detections of GOES and MODIS were spatially and temporally intersected with an MTBS burned area.

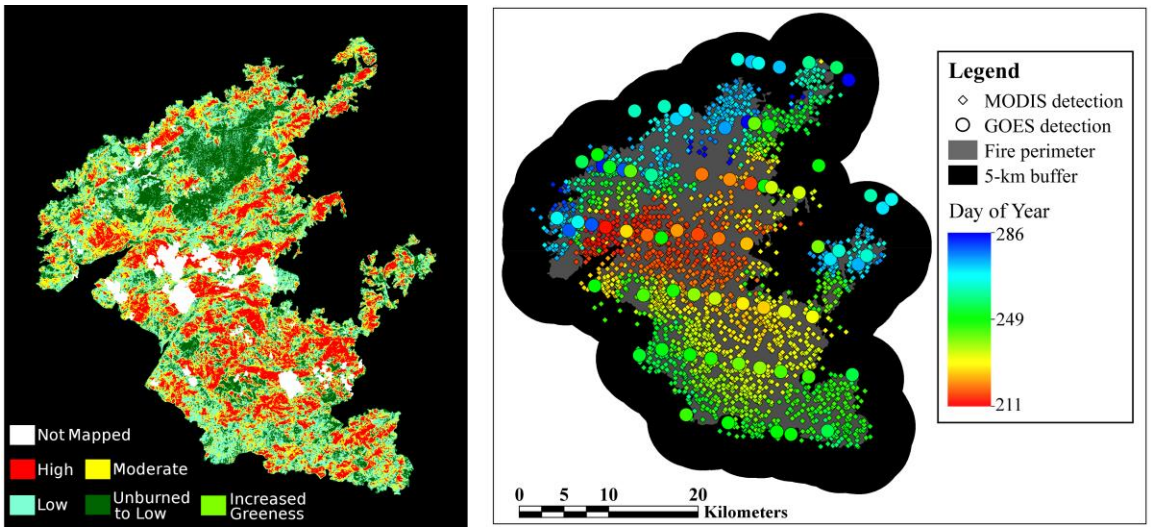

Figure 2-3. Spatial and temporal match of MTBS Landsat burned area and severity classes (left) with MODIS and GOES active fire detections (right) for the Halstead fire in Idaho, 2012.

All MTBS burned areas with insufficient active fire detections were removed from the analysis. To do this, the geographic spatial coverage of the active fire detections was derived as the spatial union of all the fire detection pixel areas within the 5 km buffered MTBS burned area over 80 days. The GOES fire pixel area was obtained from the WF_ABBA Version 65 GOES active fire product and the MODIS fire pixel area was calculated using the MODIS along-scan and along-track pixel dimensions (*Giglio*, 2013). For these two sensors, their pixel areas increase as scan angle increases from nadir to scan edge and the pixel shapes were approximated with rectangles in this study. For instance, for a MODIS fire pixel, its along-scan and along-track pixel dimensions were taken as the product of the length and width of the rectangle. The burned area was rejected from consideration if the geographic spatial coverage of the active fire detections was less than 85% of the area mapped by MTBS as low, moderate, and high burn

severity. The 85% threshold was set quite conservatively to prevent satellite FRE from being grossly underestimated due to insufficient FRP sampling, although, burned areas containing persistently burning active fires (i.e., forested systems) are less likely to be rejected. A total of 445 burned areas were selected in this way.

2.2.4. Estimation of the FRE Biomass Combustion Coefficient (FBCC)

The conventional (BC_{AMC}, equation (1)) and FRE-based (BC_{FRE}, equation (3)) biomass consumption estimates should equal the actual biomass consumption over the same fire event if the models, assumptions, and parameters, implicit in their derivations are correct. In this study, we assume that this is the case, i.e., that BC_{AMC} equals BC_{FRE}, and so rearranging equations (1) and (3) provides:

$$BC_{AMC} = FBCC \times FRE \tag{10}$$

where BC_{AMC} is the biomass consumption (kg) derived as equation (1), *FRE* is the satellite-derived FRE (MJ) defined by equation (6) (MODIS FRE) or equation (9) (GOES FRE), and *FBCC* is the FRE biomass combustion coefficient ($kg \cdot MJ^{-1}$).

The FBCC was derived by linear ordinary least squares regression of the BC_{AMC} (dependent variable) and satellite FRE estimates (independent variable) for the 455 CONUS burned areas and forcing the regression to have a zero intercept value. This was undertaken three times: considering the MODIS FRE, the GOES FRE, and the average of the MODIS and GOES FRE derived for each burn. The regression coefficient of determination (r^2) and *p*-value were used to test the statistical significance of the FBCC regression coefficients.

2.2.5. Sensitivity Analysis

There are several possible error sources that are discussed in the discussion. As there are no independent satellite FRE, or ground truth fuel consumption data, for the 455 MTBS burned areas, only a limited sensitivity analysis could be undertaken. Two sensitivity analyses of the biomass consumption estimation were conducted.

First, the CC parameterization with respect to burn severity (Table 2-1) was replaced with a single CC of 0.5, that is, simply assuming that half of the fuel load burned regardless of the fuel type or the burn severity. This value was used because it is close to the median value in Table 2-1. The biomass consumption (BC_{AMC}) was then calculated as equation (1) for the 445 selected MTBS burned areas using CC = 0.5 and the FCCS fuel loadings as before.

Second, the biomass consumption was computed in a different way using a land-cover driven approach endorsed for national emissions estimation (IPCC, 2006) defined as:

$$BC_{AMC} = \sum_{l=1}^{h} A(l)FC(l) \quad (11)$$

where BC_{AMC} is biomass consumption (kg) in the MTBS burned area; there are a total of h land cover types in the burned area and the lth land cover type has area burned A(l) (km^2) and fuel consumption FC(l) ($kg \cdot km^{-2}$). The 30m National Land Cover Database (NLCD 2011), which defines 16 land cover classes over the CONUS (Homer et al., 2015) and has a reported overall accuracy of 78.7% (Wickham et al., 2013), was used to define the land cover classes that were intersected (as described above in Section 2.2.3) with each buffered MTBS burned area. The IPCC provides mean fuel consumption (units:

$kg \cdot m^{-2}$) for broadly defined land cover types that were derived from published literature estimates (IPCC 2006). The broadly defined land cover types were cross-walked to NLCD land cover types. Across the 455 burned areas in this study there were only five (nonwater) IPCC unique mean fuel consumption values of 0.36 $kg \cdot m^{-2}$ (woody wetland and herbaceous wetland NLCD classes), 0.376 $kg \cdot m^{-2}$ (grassland, pasture, and developed open NLCD classes), 0.55 $kg \cdot m^{-2}$ (crops NLCD classes), 1.43 $kg \cdot m^{-2}$ (shrub, scrub NLCD classes), and 5.04 $kg \cdot m^{-2}$ (deciduous, mixed, and evergreen forest NLCD classes). The IPCC forest FC estimate used (5.04 $kg \cdot m^{-2}$) is similar (difference < 8%) to recent field measured U.S. forest mean FC data (van Leeuwen et al., 2014).

2.3. Results

Figure 2-4 shows the 445 (229 in 2011 and 216 in 2012) MTBS burned areas, selected because they had contemporaneous MODIS and GOES active fire detections, and their biomass consumption estimated using the conventional approach (equation (1)). The 445 MTBS burned areas occurred mainly in the west and southeastern CONUS and ranged in area from 1.221 to 1,353.088 km^2. The burned areas in the southeast were generally smaller and varied in size from 1.221 to 45.977 km^2. The largest burn was the Wallow fire in Arizona that burned 1,353.088 km^2 of predominantly mixed conifer forest including ponderosa pine, Douglas-fir, aspen, and Gambel oak (Waltz et al., 2014). The biomass consumption for the 455 burns varied from 2.47×10^{-4} to 4.08 Tg. Larger burned areas tended to have greater biomass consumption. All the burns with more than 1.0 Tg consumption occurred in the western CONUS, where the greatest biomass consumption (4.08 Tg) was for the Wallow fire. The MTBS burn severity for the 455 burned areas was

quite variable with no clear geographical pattern across the CONUS. The proportions of low, moderate, and high burn severity areas within a burned area on average were 62%, 27%, and 11%, respectively, across the 445 burned areas.

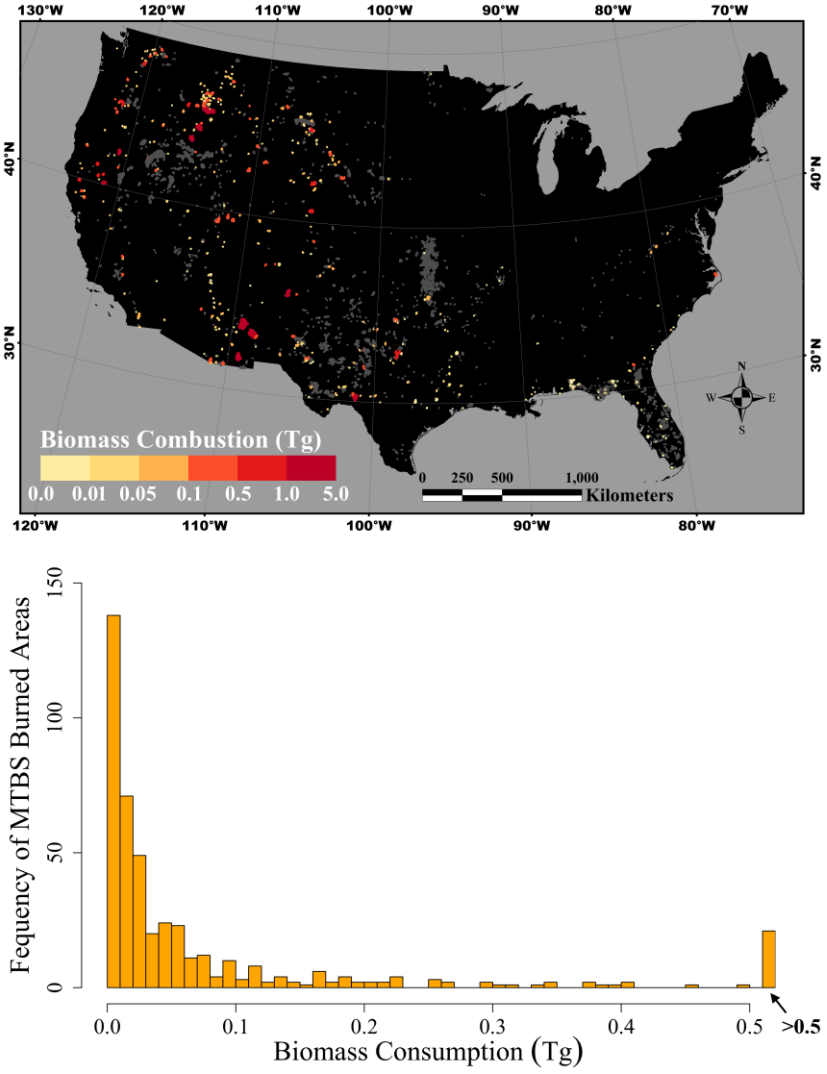

Figure 2-4. The selected 2011 and 2012 CONUS MTBS burned areas (total 445, orange and red colors) and the biomass consumption estimated by the conventional method (equation (1)) based on the burn severity parameterized combustion completeness. (top) The spatial distribution of the biomass consumption in the selected 445 burned areas (colored polygons); the gray polygons show the other 2011 and 2012 available MTBS burned areas that were not considered as they did not have sufficient contemporaneous

MODIS and GOES active fire detections (see section 2.2.3). (bottom) The histogram of the biomass consumption in the selected 445 burned areas.

Figure 2-5 shows the biomass consumption per unit area, found by dividing the biomass consumption (Figure 2-4) by the area burned. The biomass consumption per unit area was generally smaller in the southeast (< 3.0 kg $\cdot$ m^{-2}) and larger in the western states, particularly California, Oregon, and Washington, with values ranging from 1.5 to 20.0 kg $\cdot$ m^{-2}. For the largest Wallow fire, the biomass consumption per unit area was 3.02 kg $\cdot$ m^{-2} (Figure 2-5), which differs by only 4% from the biomass consumption estimated using the Consume 3.0 fuel consumption model (Veraverbeke et al., 2013). The results illustrated in Figure 2-5 are comparable in magnitude with biomass consumption estimates across the CONUS for different fires and years (where fuel conditions and fire behavior differences mean that exact quantitative comparison is not meaningful) (Lydersen et al., 2014; Prichard et al., 2017; Yokelson et al., 2013).

Figure 2-6 illustrates a comparison of the biomass consumption estimated by the conventional method based on the burn severity parameterized CC approach with the same approach but assuming CC=0.5 (Figure 2-6a) and with the IPCC FC method (Figure 2-6b). Linear regression of the results indicate that the different biomass consumption estimates were significantly correlated ($r^2 \geq 0.89$ and $p < 0.001$). The regression slopes indicate that, over the 445 sites, the burn severity parameterized biomass consumption estimates were larger by 3% than the CC=0.5 estimates but 32% smaller than the IPCC-FC based biomass consumption estimates.

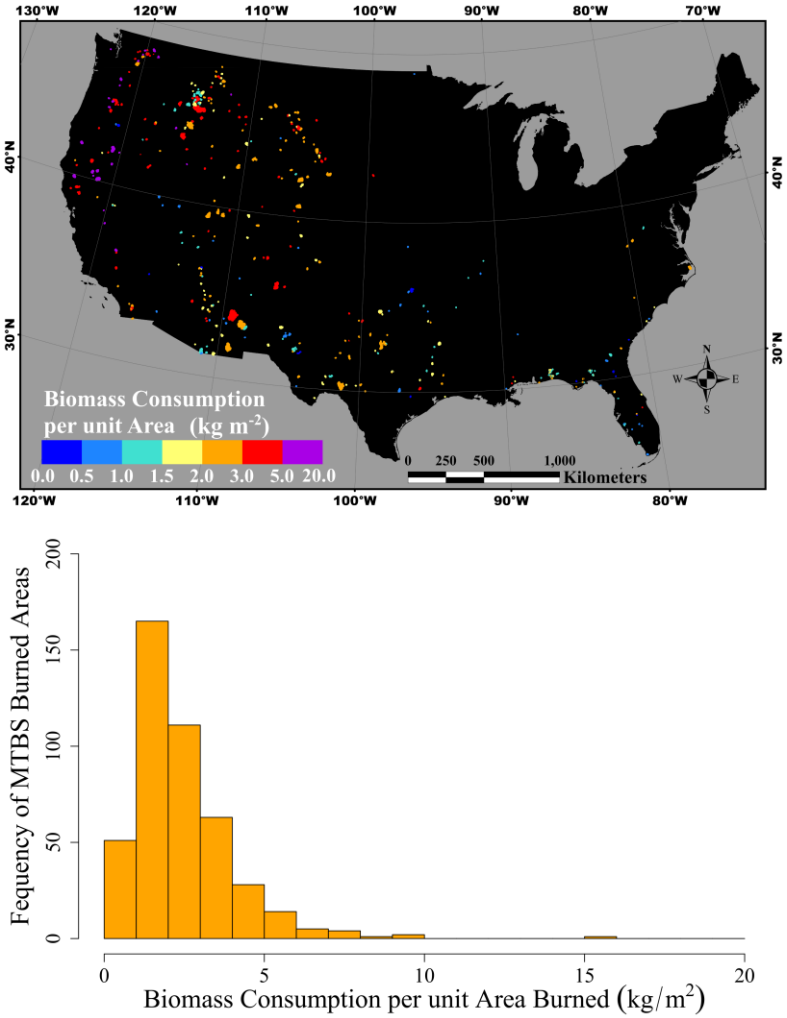

Figure 2-5. Biomass consumption (Figure 2-4) per area burned (units: kg · m^{-2}) in the selected 2011 and 2012 CONUS MTBS burned areas (total 445). (top and bottom) The spatial distribution and histogram of the biomass consumption per area burned, respectively, across the CONUS.

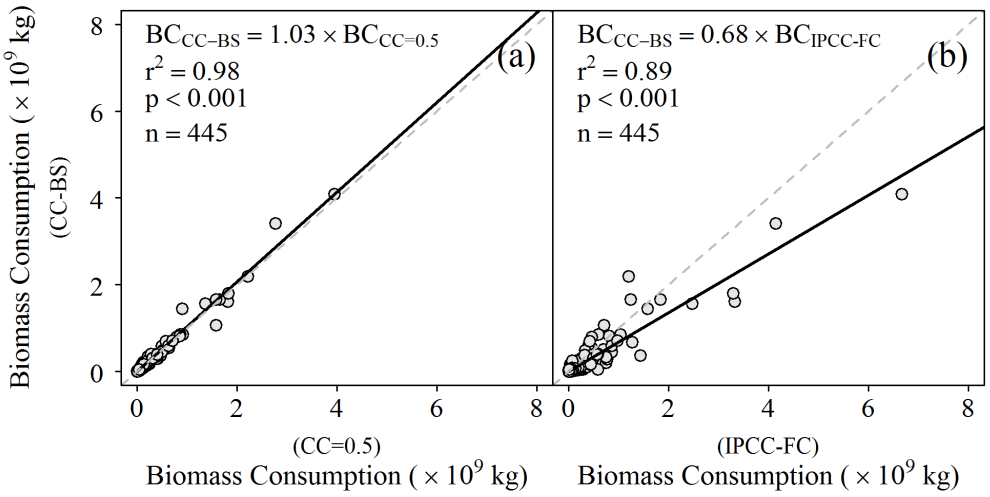

Figure 2-6. Comparison of the biomass consumption derived using the burn severity parameterized combustion completeness (CC) approach (Figure 2-4) with (a) the biomass consumption derived using the same method but fixed CC = 0.5 and with (b) the IPCC land-cover-driven approach (equation (11)). Linear regressions of the plotted data (solid lines) and the 1:1 line for comparison (dashed lines) are shown. The regression slope terms are the estimated FBCC values.

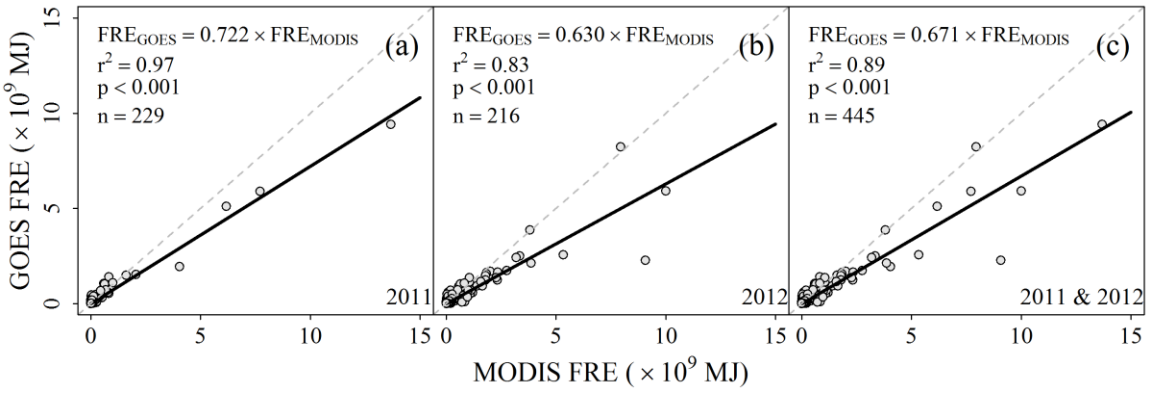

Figure 2-7. Comparisons between the adjusted cluster GOES FRE (equation (9)) and the cluster MODIS FRE (equation (6)) over the selected burned areas for (a) 2011 (229 burned areas), (b) 2012 (216 burned areas), and (c) for both 2011 and 2012 (445 burned areas). Linear regressions of the plotted data (solid lines) and the 1:1 line for comparison (dashed lines) are shown.

Figure 2-7 shows, for the burned areas in 2011, 2012, and for both years combined, the relationship between the adjusted cluster GOES FRE and the cluster MODIS FRE. The sensor FRE data were significantly correlated (r^2>0.8 and p<0.001) and the GOES FRE was about a third less than the MODIS FRE. In Figure 2-7, the GOES FRE varied from 0.99×10^5 to 9.41×10^9 MJ and the MODIS FRE varied from 5.67×10^5 to 13.68×10^9 MJ. The greatest FRE values were for the 2011 Wallow fire that also had the greatest area burned.

Figure 2-8 shows the relationships between the biomass consumption estimated by the burn severity parameterized CC approach and the GOES FRE, MODIS FRE, and the average of the GOES and MODIS FRE. The results for the burned areas in 2011, 2012, and for both years combined are shown. In all cases, the data were significantly correlated (r^2>0.75 and p<0.001). Recall that from equation (10) the slopes of the regressions plotted in Figure 2-8 provide an estimate of the FBCC. The FBCC estimates from the GOES FRE were larger than those from MODIS FRE by 34% and 46% in 2011 and 2012, respectively. When considering both years, the FBCC estimates were 0.374 kg · MJ^{-1} for GOES FRE, 0.266 kg · MJ^{-1} for MODIS FRE, and intermediate (0.320 kg · MJ^{-1}) for the average MODIS and GOES FRE.

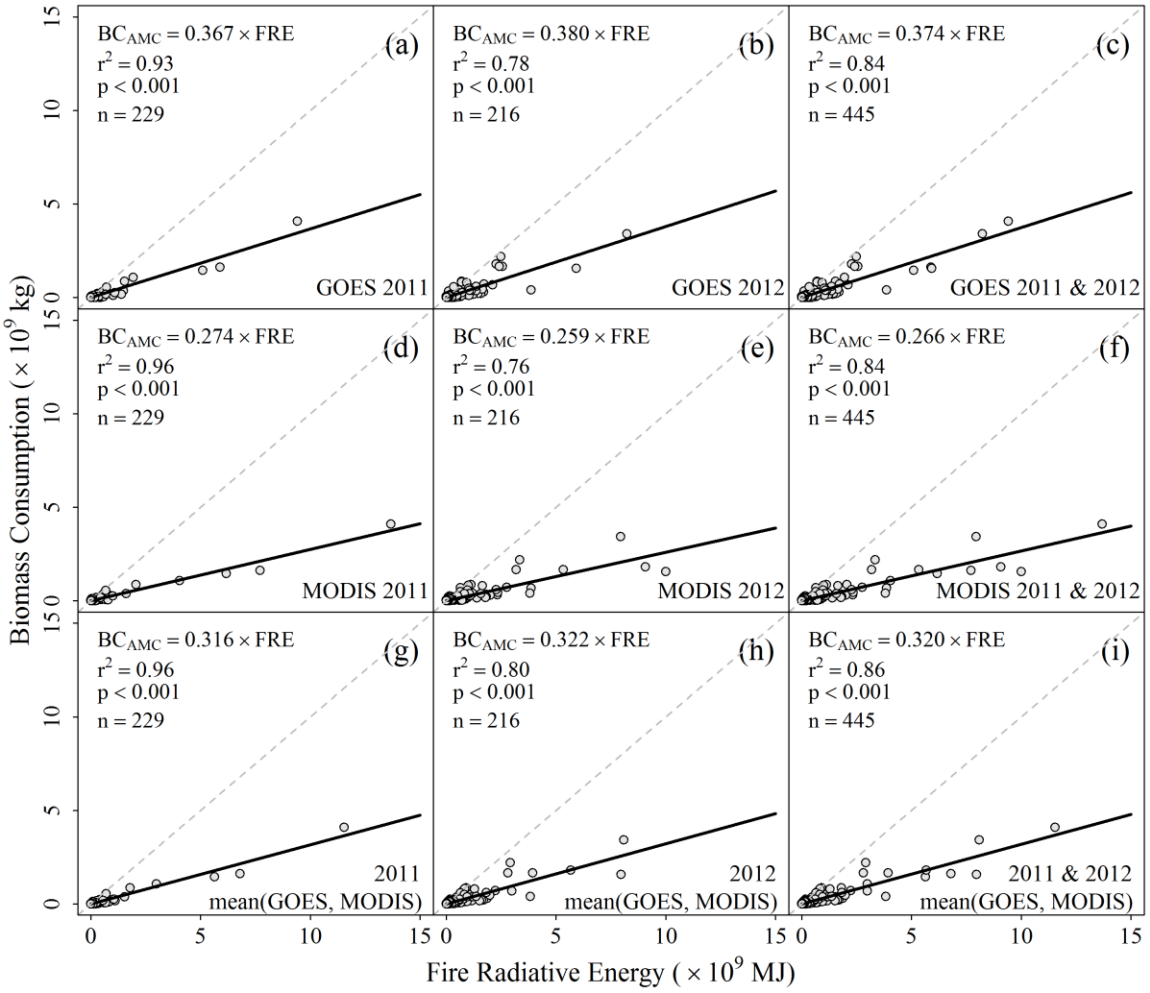

Figure 2-8. Relationships between the biomass consumption estimated by the burn severity parameterized CC approach (equation (1)) and the adjusted cluster GOES FRE (equation (9)) and the cluster MODIS FRE (equation (6)) and the average of the MODIS and GOES FRE in each burned area, for 2011, 2012, and both years together. Linear regressions of the plotted data (solid lines) and the 1:1 line (i.e., slope of 1.0 kg · MJ^{-1}) (dashed lines) are shown. The regression slope terms are the estimated FBCC values.

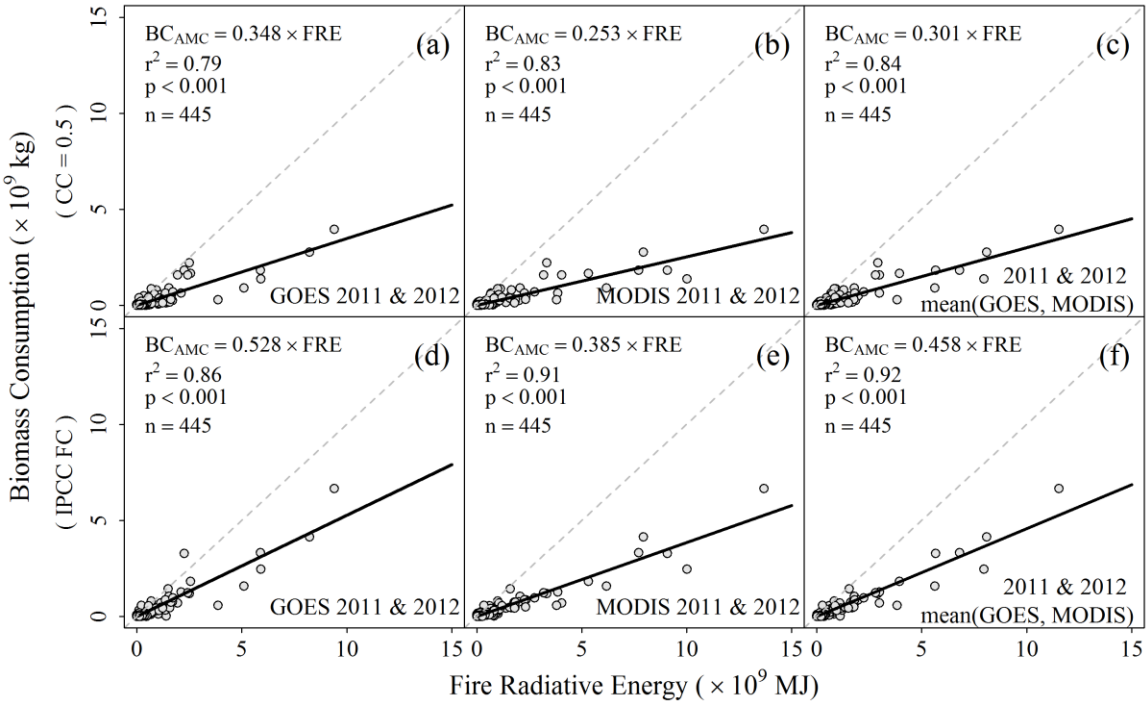

Figure 2-9. Relationships between the biomass consumption estimated with CC = 0.5 and with the IPCC-FC method with the adjusted cluster GOES FRE (equation (9)) and the cluster MODIS FRE (equation (6)) and the average of GOES and MODIS FRE in each burned area, for 2011, 2012, and both years together. Linear regressions of the plotted data (solid lines) and the 1:1 line (i.e., slope of 1.0 kg · MJ^{-1}) (dashed lines) are shown. The regression slope terms are the estimated FBCC values.

Figure 2-9 shows the same results as Figure 2-8 for both years combined (2011 and 2012) but compares the biomass consumption estimated with CC=0.5 and with the IPCC-FC method against the satellite FRE. All the regressions were significant ($r^2 \geq 0.79$ and $p<0.001$). When both years were considered, the FBCC values from GOES FRE were larger than those from the MODIS FRE by 37% for both the CC=0.5 estimation and the IPCC-FC estimation. The FBCC values from the average of GOES and MODIS FRE estimates were 0.301 kg · MJ^{-1} and 0.458 kg · MJ^{-1} for the CC=0.5 estimation and the IPCC-FC estimation, respectively, considering both years. In comparison with the FBCC estimates based on burn severity parameterized CC (Figure 2-8) when

both years were considered, the FBCC values derived assuming CC=0.5 (Figure 2-9) were smaller by 7% for GOES FRE and 5% for MODIS FRE, respectively, and the FBCC values derived from the IPCC-FC estimation (Figure 2-9) were larger by 41% for GOES FRE and 45% for MODIS FRE, respectively.

2.4. Discussion and Conclusions

This study investigated the relationship between satellite-retrieved FRE and biomass consumption estimates for 445 wildland fire events in 2011 and 2012. This large sample helps to improve our understanding of the FBCC for the estimation of biomass consumption using satellite FRP retrievals. The FBCC bridges the biomass combustion rate to FRP that provides a direct way to quantify biomass consumption (Kaufman et al., 1998; Wooster et al., 2003). The FRE-based approach may be advantageous compared to the conventional method because fuel load and CC information are not required (Wooster et al., 2003; Roberts et al., 2005). However, the FBCC value derived from different approaches is quite variable (0.13 to 12.0 kg $\cdot$ MJ^{-1}) (Freeborn et al., 2008; Kremens et al., 2012; Konovalov et al., 2014; Kaiser et al., 2012; Wooster et al., 2005; Zhang et al. 2012), which is a concern for the use of satellite FRE-based biomass consumption and biomass burning emission estimation.

The biomass consumption derived for Landsat mapped burned areas using a conventional approach (equation (1)) may have considerable uncertainty, even though the best data available, that is, MTBS Landsat burned area and FCCS fuel bed and fuel loadings, were used. The area burned from MTBS is generally considered reliable but in certain mapped burns the interior unburned areas may not be delineated, although these

interior unburned areas typically have low severity (Sparks et al., 2015) that may reduce the impact of MTBS burned area commission errors. The MTBS definition of burn severity is not consistently quantified but rather is based on subjective thresholding of the Landsat NBR that reduces their reliability (Eidenshink et al., 2007). The FCCS fuel loading information are static and so do not reflect seasonal and inter-annual fuel load changes (Pellizzaro et al., 2007). Moreover, the FCCS information may not reflect the fire history reliably; for example, a fire in the years before 2011 may have reduced the fuel load but may not be reflected in the FCCS (Steel et al., 2015). In addition, although the CC values in Table 2-1 were compiled from a large number of available forest and nonforest sources (including 15 studies summarized in Ghimire et al. (2012)), they may not adequately represent the fire behavior and fuel beds for the 445 fire events, and could be augmented using more estimates such as, for example, Lentile et al. (2009). Further, the CC parametrization by burn severity was simple, although based on empirical evidence of a linear relationship between these measures, and is known to have quite variable results (French et al., 2008; Veraverbeke et al., 2013).

In the absence of independent ground-truth biomass consumption data, sensitivity analyses were conducted to examine the sensitivity of the biomass consumption estimation. The biomass consumption estimated by the conventional method (equation (1)) based on the burn severity parameterized CC was close to that assuming a fixed CC=0.5 (Figure 2-6a). We note that CC = 0.5 is only 10% less than the mean of all the CC values parameterized by burn severity class (Table 2-1) and is about 18% smaller than the average of CC values measured at 15 sites across the CONUS (van Leeuwen et al., 2014). For the fixed CC results, potentially large biomass consumption biases may

occur if the CC values are very different to the fixed value. This may be the case as across the 445 CONUS burned areas the proportions of low, moderate, and high burn severity areas were 62%, 27%, and 11%, respectively. We also note that CC and burn severity may not always be directly related. For example, large trees that burn for long periods may result in white ash that are not detected and/or have low Landsat-derived burn severity (Smith and Hudak, 2005; Roy et al. 2010). Similarly, a fire may result in near complete combustion but the Landsat burn severity will not be mapped as high or moderate severity if only a fraction of the pixel is burned (Roy and Landmann, 2005).

Despite these caveats, the utility of the CC parameterization is evident in Figure 2-6a which shows the biomass consumption estimates based on the burn severity parameterized CC against the CC=0.5 based biomass consumption. In this figure, two burned areas had biomass consumption estimates that were 59% and 23% greater than when CC=0.5 was assumed, and these were for burned areas with moderate and high burn severity. Conversely, the one burned area with a biomass consumption estimate particularly below the 1:1 line was a low burn severity fire. Besides the parameterized CC, the need of spatially explicit fuel characteristics at burned area level was also suggested in the comparison of biomass consumption estimates based on the burn severity parameterized CC against those based on the IPCC approach (Figure 2-6). The biomass consumption estimated using the IPCC land cover based method was 32% greater than that based on burn severity and had much more scatter (Figure 2-6b) than the CC=0.5 based biomass consumption (Figure 2-6a). This could be due to the significantly simplified IPCC FC approach that is insufficient to characterize individual fire events. The use of only five unique IPCC FC values for the 445 burned areas will provide rather

generalized biomass consumption estimates that do not capture variations associated with fire behavior and site conditions.

Researchers have suggested a number of factors that may impact the reliability of satellite FRE retrieval. These include sensitivity to active fire detection capabilities (Giglio et al., 2003), under sampling of active fire events due primarily to the satellite orbit and sensing geometry and also cloud, smoke and overstory vegetation obscuration (Boschetti and Roy, 2009; Freeborn et al., 2014; Kumar et al., 2011; Mathews et al., 2016; Xu et al., 2010), reduction in FRP values due to the absorbing properties of smoke and atmospheric water vapor (Wooster et al., 2005) and fuel moisture (Smith et al. 2013), and issues with the geometric sensing characteristics relative to the spatial configuration and temperatures of actively burning fires (Calle et al., 2009; Freeborn et al., 2014). In this study, the polar-orbiting MODIS and geostationary GOES FRP data were used to derive the FRE. Compared to GOES, the MODIS is able to detect smaller and cooler fires but no more than four times per day. Conversely, the GOES has the capability to capture the fire diurnal variation due to its 5-15 min sampling but cannot detect small and cool fires (Freeborn et al., 2011; Roberts and Wooster., 2014; Xu et al., 2010; Zhang et al., 2012). In this study, the pixel-level MODIS FRP was adjusted using the method by (Freeborn et al., 2011) to mitigate the underestimation of MODIS FRP at off-nadir (equation (4)) and aggregated to obtain adjusted cluster-level MODIS FRP (equation (5)). To account for the underestimation of GOES FRP due to missed small and cool fires, the cluster-level GOES FRP estimate at each GOES observing time was adjusted over each of the 455 burned areas by adding an FRP offset (equation (8)) that was calculated from the difference between the cluster-level GOES and adjusted MODIS FRP estimates. The

example in Figure 2-2 illustrates the adjustment of cluster-level GOES FRP in different situations. The cluster-level MODIS FRP and adjusted GOES FRP were applied to estimate adjusted MODIS FRE and adjusted GOES FRE using established temporal integration methods (Boschetti and Roy, 2009; Zhang et al., 2012). The adjusted MODIS and GOES FRE values were significantly correlated across the 445 burned areas and the GOES FRE was about a third less than the MODIS FRE. Other researchers have noted smaller MODIS FRE than geostationary FRE derived over Africa from the Meteosat Second Generation (MSG) SEVIRI FRE (Freeborn et al., 2011; Vermote et al., 2009) although this could be attributed to different FRE derivation methodologies, fire regimes, and sensor capabilities. The satellite-derived FRE in this study could not be validated because there are no independent and contemporaneous FRE measurements. The relative error characteristics of the adjusted GOES and MODIS FRE are unknown and so for each burned area, their average was taken. Further work to investigate a weighting scheme or some other way to optimally combine the FRE from these the MODIS and GOES sensors is recommended.

Despite the above issues, this study demonstrated that the derived FBCC values were relatively stable. Comparing the satellite FRE with the biomass consumption estimated by the burn severity parameterized CC approach provided FBCC values of 0.374 kg $\cdot$ MJ^{-1} (GOES), 0.266 kg $\cdot$ MJ^{-1} (MODIS), and 0.320 kg $\cdot$ MJ^{-1} (average of GOES and MODIS FRE) when both years (2011 and 2012) were considered for the 445 CONUS fire events, and for either year, the derived FBCC value of one year varied by less than 6% of the other year's value. The other biomass consumption estimation methods considered provided similar magnitude FBCC values, with a two-year average

GOES and MODIS FRE estimate of 0.301 kg · MJ^{-1} when the CC was fixed at 0.5 and 0.458 kg · MJ^{-1} for the IPCC based method. All of these values are similar to the FBCC values derived from field and plume tower prescribed fire experiments (0.368 - 0.453 kg · MJ^{-1}) (Freeborn et al., 2008; Kremens et al., 2012; Wooster et al., 2005) and also with certain synoptic scale satellite research (0.300 to 0.520 kg · MJ^{-1}) (Konovalov et al., 2014). They are smaller however than the FBCC values (0.13 to 1.55 kg · MJ^{-1}) estimated using Global Fire Emissions Database and MODIS FRE (Kaiser et al., 2012) and much smaller than the values (1.6 to 12.0 kg · MJ^{-1}) derived comparing MODIS-based emissions coefficients and aerosol optical thickness data (Sofiev et al., 2009; Zhang et al. 2012). The large discrepancies among FBCC values derived by different approaches may explain some of the discrepancies among the existing FRP based emissions datasets (Zhang et al., 2012; Zhang et al., 2014b).

In summary, this study confirms the empirical relationship between biomass consumption estimates and FRE for landscape wildland fires. Despite the uncertainties in the data used it is important to note that for all cases the experiments confirmed the linear relationship between FRE and biomass consumption observed in previous studies (Freeborn et al., 2008; Kremens et al., 2012; Wooster et al., 2005). For combined use of GOES and MODIS FRE, an FBCC value of 0.320 kg · MJ^{-1} is suggested. Landscape-scale and detailed fire event specific experiments are needed. However, this is challenging due to the difficulty in measuring pre-fire and post-fire fuel loads and spatially explicit CC over large burned areas. These challenges might be mitigated by advances in technologies of remote sensing and field measurements, for example, application of LiDAR in estimation of fuel loads from airborne and ground-based

platforms (Cooper et al., 2017; Hudak et al., 2016; Price and Gordon, 2016) over prescribed fires, and also over wildfires if the pre-fire fuel conditions can be assessed.

Acknowledgments

This research was funded by NOAA contract NA14NES4320003 and BG-133E-15-SE-1613. The manuscript contents are solely the opinions of the author(s) and do not constitute a statement of policy, decision, or position on behalf of NOAA or the U.S. Government. The authors thank reviewers and Editors for their constructive comments. The authors comply with AGU's data policy. The output data sets of this study are accessible at the institutional repository of South Dakota State University (https://openprairie.sdstate.edu/global_land_surface_season_data/3/).

References

Andreae, M. O., & Merlet, P. (2001). Emission of trace gases and aerosols from biomass burning. *Global Biogeochemical Cycles*, 15(4), 955–966, doi: https://doi.org/10.1029/2000GB001382.

Anjozian, L.-N. (2009). Consume 3.0—A software tool for computing fuel consumption. In Fire Science Brief (Vol. 55, pp. 1–6). Retrieved from https://www.firescience.gov/projects/briefs/98-1-9-06_FSBrief55.pdf, last accessed on 1/30/2018.

Boschetti, L., & Roy, D. P. (2009). Strategies for the fusion of satellite fire radiative power with burned area data for fire radiative energy derivation. *Journal of Geophysical Research*, 114, D20302, doi: https://doi.org/10.1029/2008JD011645.

Boschetti, L., Eva, H. D., Brivio, P. A., & Grégoire, J. M. (2004). Lessons to be learned from the comparison of three satellite-derived biomass burning products. *Geophysical Research Letters*, 31, L21501, doi: https://doi.org/10.1029/2004GL021229.

Boschetti, L., Roy, D. P., Justice, C. O., & Humber, M. L. (2015). MODIS–Landsat fusion for large area 30 m burned area mapping. *Remote Sensing of Environment*, 161(0), 27–42, doi: https://doi.org/10.1016/j.rse.2015.01.022.

Bowman, D. M. J. S., Balch, J. K., Artaxo, P., Bond, W. J., Carlson, J. M., Cochrane, M. A., et al. (2009). Fire in the Earth system. Science, 324(5926), 481–484, doi: https://doi.org/10.1126/science.1163886.

Calle, A., Casanova, J. L., & González-Alonso, F. (2009). Impact of point spread function of MSG-SEVIRI on active fire detection. *International Journal of Remote Sensing*, 30(17), 4567–4579, doi: https://doi.org/10.1080/01431160802609726.

Campbell, J., Donato, D., Azuma, D., & Law, B. (2007). Pyrogenic carbon emission from a large wildfire in Oregon, United States. *Journal of Geophysical Research: Biogeosciences*, 112, G04014, doi: https://doi.org/10.1029/2007JG000451.

Cocke, A. E., Fulé, P. Z., & Crouse, J. E. (2005). Comparison of burn severity assessments using differenced normalized burn ratio and ground data. *International Journal of Wildland Fire*, 14(2), 189–198, doi: https://doi.org/10.1071/WF04010.

Cooper, S., Roy, D., Schaaf, C., & Paynter, I. (2017). Examination of the potential of terrestrial laser scanning and structure-from-motion photogrammetry for rapid nondestructive field measurement of grass biomass. *Remote Sensing*, 9(12), 531, doi: https://doi.org/10.3390/rs9060531.

Cruz, M. G., & Alexander, M. E. (2010). Assessing crown fire potential in coniferous forests of western North America: A critique of current approaches and recent simulation studies. *International Journal of Wildland Fire*, 19(4), 377–398, doi: https://doi.org/10.1071/WF08132.

De Santis, A., & Chuvieco, E. (2009). GeoCBI: A modified version of the composite burn index for the initial assessment of the short-term burn severity from remotely sensed data. *Remote Sensing of Environment*, 113(3), 554–562, doi: https://doi.org/10.1016/j.rse.2008.10.011.

Disney, M. I., Lewis, P., Gomez-Dans, J., Roy, D., Wooster, M. J., & Lajas, D. (2011). 3D radiative transfer modelling of fire impacts on a two-layer savanna system. *Remote Sensing of Environment*, 115(8), 1866–1881, doi: https://doi.org/10.1016/j.rse.2011.03.010.

Eidenshink, J., Schwind, B., Brewer, K., Zhu, Z., Quayle, B., & Howard, S. (2007). A project for monitoring trends in burn severity. Fire Ecology, 3(1), 3–21, doi: https://doi.org/10.4996/fireecology.0301003.

Ellicott, E., Vermote, E., Giglio, L., & Roberts, G. (2009). Estimating biomass consumed from fire using MODIS FRE. *Geophysical Research Letters*, 36, L13401, doi: https://doi.org/10.1029/2009GL038581.

Epting, J., Verbyla, D., & Sorbel, B. (2005). Evaluation of remotely sensed indices for assessing burn severity in interior Alaska using Landsat TM and ETM+. *Remote Sensing of Environment*, 96(3-4), 328–339, doi: https://doi.org/10.1016/j.rse.2005.03.002.

Freeborn, P. H., Wooster, M. J., Hao, W. M., Ryan, C. A., Nordgren, B. L., Baker, S. P., & Ichoku, C. (2008). Relationships between energy release, fuel mass loss, and trace gas and aerosol emissions during laboratory biomass fires. *Journal of Geophysical Research*, 113, DO1301, doi: https://doi.org/10.1029/2007JD008679.

Freeborn, P. H., Wooster, M. J., & Roberts, G. (2011). Addressing the spatiotemporal sampling design of MODIS to provide estimates of the fire radiative energy emitted from Africa. *Remote Sensing of Environment*, 115(2), 475–489, doi: https://doi.org/10.1016/j.rse.2010.09.017.

Freeborn, P. H., Wooster, M. J., Roberts, G., Malamud, B. D., & Xu, W. (2009). Development of a virtual active fire product for Africa through a synthesis of geostationary and polar orbiting satellite data. *Remote Sensing of Environment*, 113(8), 1700–1711, doi: https://doi.org/10.1016/j.rse.2009.03.013.

Freeborn, P. H., Wooster, M. J., Roy, D. P., & Cochrane, M. A. (2014). Quantification of MODIS fire radiative power (FRP) measurement uncertainty for use in satellite-based active fire characterization and biomass burning estimation. *Geophysical Research Letters*, 41, 1988–1994, doi: https://doi.org/10.1002/2013GL059086.

French, N. H. F., Kasischke, E. S., Hall, R. J., Murphy, K. A., Verbyla, D. L., Hoy, E. E., & Allen, J. L. (2008). Using Landsat data to assess fire and burn severity in the north American boreal forest region: An overview and summary of results. *International Journal of Wildland* Fire, 17(4), 443–462, doi: https://doi.org/10.1071/WF08007.

Ghimire, B., Williams, C. A., Collatz, G. J., & Vanderhoof, M. (2012). Fire-induced carbon emissions and regrowth uptake in western U.S. forests: Documenting variation

across forest types, fire severity, and climate regions. *Journal of Geophysical Research*, 117, G03036, doi: https://doi.org/10.1029/2011JG001935.

Giglio, L. (2013). MODIS Collection 5 active fire product User's guide, version 2.5, available at: http://modis-fire.umd.edu/files/MODIS_Fire Users_Guide_2.5.pdf, last accessed on 1/30/2018.

Giglio, L., Descloitres, J., Justice, C. O., & Kaufman, Y. J. (2003). An enhanced contextual fire detection algorithm for MODIS. *Remote Sensing of Environment*, 87(2-3), 273–282, doi: https://doi.org/10.1016/S0034-4257(03)00184-6.

Hawbaker, T. J., Vanderhoof, M. K., Beal, Y.-J., Takacs, J. D., Schmidt, G. L., Falgout, J. T., et al. (2017). Mapping burned areas using dense time series of Landsat data. *Remote Sensing of Environment*, 198, 504–522, doi: https://doi.org/10.1016/j.rse.2017.06.027.

Hély, C., Alleaume, S., Swap, R. J., Shugart, H. H., & Justice, C. O. (2003). SAFARI-2000 characterization of fuels, fire behavior, combustion completeness, and emissions from experimental burns in infertile grass savannas in western Zambia. *Journal of Arid Environments*, 54(2), 381–394, doi: https://doi.org/10.1006/jare.2002.1097.

Heward, H., Smith, A. M. S., Roy, D. P., Tinkham, W. T., Hoffman, C. M., Morgan, P., & Lannom, K. O. (2013). Is burn severity related to fire intensity? Observations from landscape scale remote sensing. *International Journal of Wildland Fire*, 22(7), 910–918, doi: https://doi.org/10.1071/WF12087.

Homer, C. G., Dewitz, J. A., Yang, L., Jin, S., Danielson, P., Xian, G., et al. (2015). Completion of the 2011 National Land Cover Database for the Conterminous United

States—Representing a decade of land cover change information. *Photogrammetric Engineering and Remote Sensing*, 81(5), 345–354.

Hudak, A. T., Dickinson, M. B., Bright, B. C., Kremens, R. L., Loudermilk, E. L., O'Brien, J. J., et al. (2016). Measurements relating fire radiative energy density and surface fuel consumption – RxCADRE 2011 and 2012. *International Journal of Wildland Fire*, 25(1), 25–37, doi: https://doi.org/10.1071/WF14159.

Ichoku, C., & Kaufman, Y. J. (2005). A method to derive smoke emission rates from MODIS fire radiative energy measurements. *IEEE Transactions on Geoscience and Remote Sensing*, 43(11), 2636–2649, doi: https://doi.org/10.1109/TGRS.2005.857328.

IPCC (2006). 2006 IPCC guidelines for National Greenhouse Gas Inventories. In H. S. Eggleston, et al. (Eds.), Prepared by the National Greenhouse gas Inventories Programme (Chap. 2, pp. 1–59). IGES, Japan.

Ito, A., & Penner, J. E. (2004). Global estimates of biomass burning emissions based on satellite imagery for the year 2000. *Journal of Geophysical Research*, 109, D14S05, doi: https://doi.org/10.1029/2003JD004423.

Kaiser, J. W., Heil, A., Andreae, M. O., Benedetti, A., Chubarova, N., Jones, L., et al. (2012). Biomass burning emissions estimated with a global fire assimilation system based on observed fire radiative power. *Biogeosciences*, 9(1), 527–554, doi: https://doi.org/10.5194/bg-9-527-2012.

Kasischke, E. S., Loboda, T., Giglio, L., French, N. H. F., Hoy, E. E., de Jong, B., & Riano, D. (2011). Quantifying burned area for North American forests: Implications

for direct reduction of carbon stocks. *Journal of Geophysical Research*, 116, G04003, doi: https://doi.org/10.1029/2011JG001707.

Kaufman, Y. J., Remer, L., Ottmar, R., Ward, D., Li, R.-R., Kleidman, R., et al. (1996). Relationship between remotely sensed fire intensity and rate of emission of smoke: SCAR-C experiment. In J. Levin (Ed.), Global Biomass Burning (pp. 685–696). Cambridge MA: The MIT Press.

Kaufman, Y. J., Justice, C. O., Flynn, L. P., Kendall, J. D., Prins, E. M., Giglio, L., et al. (1998). Potential global fire monitoring from EOS-MODIS. *Journal of Geophysical Research*, 103(D24), 32,215–32,238, doi: https://doi.org/10.1029/98JD01644.

Keeley, J. E. (2009). Fire intensity, fire severity and burn severity: A brief review and suggested usage. *International Journal of Wildland Fire*, 18(1), 116–126, doi: https://doi.org/10.1071/WF07049.

Key, C. H., &Benson, N. C. (2005). Landscape assessment: Remote sensing of severity, the normalized burn ratio, Rep., LA1-LA51 pp, Ogden, UT.

Key, C. H., & Benson, N. C. (2006). Landscape assessment (LA), FIREMON: Fire effects monitoring and inventory system. Gen. Tech. Rep. RMRSGTR-164-CD, Fort Collins, CO: US Department of Agriculture, Forest Service, Rocky Mountain Research Station.

Konovalov, I. B., Berezin, E. V., Ciais, P., Broquet, G., Beekmann, M., Hadji-Lazaro, J., et al. (2014). Constraining CO2 emissions from open biomass burning by satellite observations of co-emitted species: A method and its application to wildfires in

Siberia. *Atmospheric Chemistry and Physics*, 14(19), 10383–10410, doi: https://doi.org/10.5194/acp-14-10383-2014.

Kremens, R. L., Dickinson, M. B., & Bova, A. S. (2012). Radiant flux density, energy density and fuel consumption in mixed-oak forest surface fires. *International Journal of Wildland Fire*, 21(6), 722–730, doi: https://doi.org/10.1071/WF10143.

Kumar, S. S., Roy, D. P., Boschetti, L., & Kremens, R. (2011). Exploiting the power law distribution properties of satellite fire radiative power retrievals: A method to estimate fire radiative energy and biomass burned from sparse satellite observations. *Journal of Geophysical Research*, 116, D19303, doi: https://doi.org/10.1029/2011JD015676.

Lentile, L. B., Holden, Z. A., Smith, A. M. S., Falkowski, M. J., Hudak, A. T., Morgan, P., et al. (2006). Remote sensing techniques to assess active fire characteristics and post-fire effects. *International Journal of Wildland Fire*, 15(3), 319–345, doi: https://doi.org/10.1071/WF05097.

Lentile, L. B., Smith, A. M. S., Hudak, A. T., Morgan, P., Bobbitt, M. J., Lewis, S. A., & Robichaud, P. R. (2009). Remote sensing for prediction of 1-year post-fire ecosystem condition. *International Journal of Wildland Fire*, 18(5), 594–608, doi: https://doi.org/10.1071/WF07091.

Loveland, T. R., Reed, B. C., Brown, J. F., Ohlen, D. O., Zhu, Z., Yang, L., & Merchant, J. W. (2000). Development of a global land cover characteristics database and IGBP DISCover from 1 km AVHRR data. *International Journal of Remote Sensing*, 21(6-7), 1303–1330, doi: https://doi.org/10.1080/014311600210191.

Lutes, D. C., Keane, R. E., & Caratti, J. F. (2009). A surface fuel classification for estimating fire effects. *International Journal of Wildland Fire*, 18(7), 802–814, doi: https://doi.org/10.1071/WF08062.

Lydersen, J. M., Collins, B. M., Ewell, C. M., Reiner, A. L., Fites, J. A., Dow, C. B., et al. (2014). Using field data to assess model predictions of surface and ground fuel consumption by wildfire in coniferous forests of California. *Journal of Geophysical Research: Biogeosciences*, 119, 223–235, doi: https://doi.org/10.1002/2013JG002475.

Mathews, B. J., Strand, E. K., Smith, A.M. S., Hudak, A. T., Hudak, A. T., Dickinson, B., & Kremens, R. L. (2016). Laboratory experiments to estimate interception of infrared radiation by tree canopies. *International Journal of Wildland Fire*, 25(9), 1009–1014, doi: https://doi.org/10.1071/WF16007.

Meigs, G. W., Donato, D. C., Campbell, J. L., Martin, J. G., & Law, B. E. (2009). Forest fire impacts on carbon uptake, storage, and emission: The role of burn severity in the eastern cascades, Oregon. *Ecosystems*, 12(8), 1246–1267, doi: https://doi.org/10.1007/s10021-009-9285-x.

Moody, J. A., Martin, D. A., Haire, S. L., & Kinner, D. A. (2008). Linking runoff response to burn severity after a wildfire. *Hydrological Processes*, 22(13), 2063–2074, doi: https://doi.org/10.1002/hyp.6806.

Ottmar, R. D., Prichard, S. J., Vihnanek, R. E., & Sandberg, D. V. (2006). Modification and validation of fuel consumption models for shrub and forested lands in the

Southwest, Pacific Northwest, Rockies, Midwest, Southeast and Alaska, Joint Fire Science Program. Seattle Washington.

Ottmar, R. D., Sandberg, D. V., Riccardi, C. L., & Prichard, S. J. (2007). An overview of the Fuel Characteristic Classification System—Quantifying, classifying, and creating fuelbeds for resource planning, This article is one of a selection of papers published in the special forum on the fuel characteristic classification system. *Canadian Journal of Forest Research*, 37(12), 2383–2393, doi: https://doi.org/10.1139/X07-077.

Pellizzaro, G., Cesaraccio, C., Duce, P., Ventura, A., & Zara, P. (2007). Relationships between seasonal patterns of live fuel moisture and meteorological drought indices for Mediterranean shrubland species. *International Journal of Wildland Fire*, 16(2), 232–241, doi: https://doi.org/10.1071/WF06081.

Peterson, D., Wang, J., Ichoku, C., Hyer, E., & Ambrosia, V. (2013). A sub-pixel-based calculation of fire radiative power from MODIS observations 1: Algorithm development and initial assessment. *Remote Sensing of Environment*, 129(0), 262–279, doi: https://doi.org/10.1016/j.rse.2012.10.036.

Pettinari, M. L., & Chuvieco, E. (2016). Generation of a global fuel data set using the Fuel Characteristic Classification System. *Biogeosciences*, 13(7), 2061–2076, doi: https://doi.org/10.5194/bg-13-2061-2016.

Price, O. F., & Gordon, C. E. (2016). The potential for LiDAR technology to map fire fuel hazard over large areas of Australian forest. *Journal of Environmental Management*, 181, 663–673, doi: https://doi.org/10.1016/j.jenvman.2016.08.042.

Prichard, S. J., Sandberg, D. V., Ottmar, R. D., Eberhardt, E., Andreu, A., Eagle, P., & Swedin, K. (2013). Fuel characteristic classification system version 3.0: Technical documentation Rep., 79 pp, U.S. Department of Agriculture, Forest Service, Pacific Northwest Research Station.

Prichard, S. J., Kennedy, M. C., Wright, C. S., Cronan, J. B., & Ottmar, R. D. (2017). Predicting forest floor and woody fuel consumption from prescribed burns in southern and western pine ecosystems of the United States. *Forest Ecology and Management*, 405, 328–338, doi: https://doi.org/10.1016/j.foreco.2017.09.025.

Prins, E. M., Feltz, J. M., Menzel, W. P., & Ward, D. E. (1998). An overview of GOES-8 diurnal fire and smoke results for SCAR-B and 1995 fire season in South America. *Journal of Geophysical Research*, 103(D24), 31,821–31,835, doi: https://doi.org/10.1029/98JD01720.

Randerson, J. T., Chen, Y., van der Werf, G. R., Rogers, B. M., & Morton, D. C. (2012). Global burned area and biomass burning emissions from small fires. *Journal of Geophysical Research*, 117, G04012, doi: https://doi.org/10.1029/2012JG002128.

Roberts, G. J., & Wooster, M. J. (2008). Fire detection and fire characterization over Africa using Meteosat SEVIRI. *IEEE Transactions on Geoscience and Remote Sensing*, 46(4), 1200–1218, doi: https://doi.org/10.1109/TGRS.2008.915751.

Roberts, G., & Wooster, M. J. (2014). Development of a multi-temporal Kalman filter approach to geostationary active fire detection & fire radiative power (FRP) estimation. *Remote Sensing of Environment*, 152(0), 392–412, doi: https://doi.org/10.1016/j.rse.2014.06.020.

Roberts, G., Wooster, M. J., Perry, G. L. W., Drake, N., Rebelo, L. M., & Dipotso, F. (2005). Retrieval of biomass combustion rates and totals from fire radiative power observations: Application to southern Africa using geostationary SEVIRI imagery. *Journal of Geophysical Research*, 110, D21111, doi: https://doi.org/10.1029/2005JD006018.

Rocha, A. V., & Shaver, G. R. (2011). Burn severity influences postfire CO2 exchange in arctic tundra. *Ecological Applications*, 21(2), 477–489, doi: https://doi.org/10.1890/10-0255.1.

Roy, D. P., & Landmann, T. (2005). Characterizing the surface heterogeneity of fire effects using multi-temporal reflective wavelength data. *International Journal of Remote Sensing*, 26(19), 4197–4218, doi: https://doi.org/10.1080/01431160500112783.

Roy, D. P., Boschetti, L., & Trigg, S. N. (2006). Remote sensing of fire severity: Assessing the performance of the normalized burn ratio. *IEEE Geoscience and Remote Sensing Letters*, 3(1), 112–116, doi: https://doi.org/10.1109/LGRS.2005.858485.

Roy, D. P., Boschetti, L., Maier, S. W., & Smith, A. M. S. (2010). Field estimation of ash and char colour-lightness using a standard grey scale. *International Journal of Wildland Fire*, 19(6), 698–704, doi: https://doi.org/10.1071/WF09133.

Schmidt, C. C., & Prins, E. M. (2003). GOES wildfire ABBA applications in the western hemisphere. Paper presented at 2nd International Wildland Fire Ecology and Fire Management Congress and 5th Symp. on Fire and Forest Meteorology, Citeseer.

Seiler, W., & Crutzen, P. (1980). Estimates of gross and net fluxes of carbon between the biosphere and the atmosphere from biomass burning. *Climatic Change*, 2(3), 207–247, doi: https://doi.org/10.1007/BF00137988.

Smith, A. M. S., & Hudak, A. T. (2005). Estimating combustion of large downed woody debris from residual white ash. *International Journal of Wildland Fire*, 14(3), 245–248, doi: https://doi.org/10.1071/WF05011.

Smith, A. M. S., & Wooster, M. J. (2005). Remote classification of head and backfire types from MODIS fire radiative power and smoke plume observations. *International Journal of Wildland Fire*, 14(3), 249–254, doi: https://doi.org/10.1071/WF05012.

Smith, A. M. S., Tinkham, W. T., Roy, D. P., Boschetti, L., Kremens, R. L., Kumar, S. S., et al. (2013). Quantification of fuel moisture effects on biomass consumed derived from fire radiative energy retrievals. *Geophysical Research Letters*, 40, 6298–6302, doi: https://doi.org/10.1002/2013GL058232

Sofiev, M., Vankevich, R., Lotjonen, M., Prank, M., Petukhov, V., Ermakova, T., et al. (2009). An operational system for the assimilation of the satellite information on wild-land fires for the needs of air quality modelling and forecasting. *Atmospheric Chemistry and Physics*, 9(18), 6833–6847, doi: https://doi.org/10.5194/acp-9-6833-2009.

Sparks, A. M., Boschetti, L., Smith, A. M. S., Tinkham, W. T., Lannom, K. O., & Newingham, B. A. (2015). An accuracy assessment of the MTBS burned area product for shrub–steppe fires in the northern Great Basin, United States. *International Journal of Wildland Fire*, 24(1), 70–78, doi: https://doi.org/10.1071/WF14131.

Steel, Z. L., Safford, H. D., & Viers, J. H. (2015). The fire frequency-severity relationship and the legacy of fire suppression in California forests. *Ecosphere*, 6(1), art8–ar23, doi: https://doi.org/10.1890/ES14-00224.1.

van der Werf, G. R., Randerson, J. T., Giglio, L., Collatz, G. J., Mu, M., Kasibhatla, P. S., et al. (2010). Global fire emissions and the contribution of deforestation, savanna, forest, agricultural, and peat fires (1997–2009). *Atmospheric Chemistry and Physics*, 10(23), 11,707–11,735, doi: https://doi.org/10.5194/acp-10-11707-2010.

van Leeuwen, T. T., van der Werf, G. R., Hoffmann, A. A., Detmers, R. G., Rücker, G., French, N. H. F., et al. (2014). Biomass burning fuel consumption rates: A field measurement database. *Biogeosciences*, 11(24), 7305–7329, doi: https://doi.org/10.5194/bg-11-7305-2014.

Veraverbeke, S., & Hook, S. J. (2013). Evaluating spectral indices and spectral mixture analysis for assessing fire severity, combustion completeness and carbon emissions. *International Journal of Wildland Fire*, 22(5), 707–720, doi: https://doi.org/10.1071/WF12168.

Vermote, E., Ellicott, E., Dubovik, O., Lapyonok, T., Chin, M., Giglio, L., & Roberts, G. J. (2009). An approach to estimate global biomass burning emissions of organic and black carbon from MODIS fire radiative power. *Journal of Geophysical Research*, 114, D18205, doi: https://doi.org/10.1029/2008JD011188.

Waltz, A. E. M., Stoddard, M. T., Kalies, E. L., Springer, J. D., Huffman, D. W., & Meador, A. S. (2014). Effectiveness of fuel reduction treatments: Assessing metrics

of forest resiliency and wildfire severity after the Wallow Fire, AZ. *Forest Ecology and Management*, 334, 43–52, doi: https://doi.org/10.1016/j.foreco.2014.08.026.

Ward, D. E., Hao, W. M., Susott, R. A., Babbitt, R. E., Shea, R. W., Kauffman, J. B., & Justice, C. O. (1996). Effect of fuel composition on combustion efficiency and emission factors for African savanna ecosystems. *Journal of Geophysical Research*, 101(D19), 23,569–23,576, doi: https://doi.org/10.1029/95JD02595.

Wickham, J. D., Stehman, S. V., Gass, L., Dewitz, J., Fry, J. A., & Wade, T. G. (2013). Accuracy assessment of NLCD 2006 land cover and impervious surface. *Remote Sensing of Environment*, 130, 294–304, doi: https://doi.org/10.1016/j.rse.2012.12.001.

Wolfe, R. E., Roy, D. P., & Vermote, E. (1998). MODIS land data storage, gridding, and compositing methodology: Level 2 grid. *IEEE Transactions on Geoscience and Remote Sensing*, 36(4), 1324–1338, doi: https://doi.org/10.1109/36.701082.

Wolfe, R. E., Nishihama, M., Fleig, A. J., Kuyper, J. A., Roy, D. P., Storey, J. C., & Patt, F. S. (2002). Achieving sub-pixel geolocation accuracy in support of MODIS land science. *Remote Sensing of Environment*, 83(1-2), 31–49, doi: https://doi.org/10.1016/S0034-4257(02)00085-8.

Wooster, M. J. (2002). Small-scale experimental testing of fire radiative energy for quantifying mass combusted in natural vegetation fires. *Geophysical Research Letters*, 29(21), 2027, doi: https://doi.org/10.1029/2002GL015487.

Wooster, M. J., Zhukov, B., & Oertel, D. (2003). Fire radiative energy for quantitative study of biomass burning: Derivation from the BIRD experimental satellite and

comparison to MODIS fire products. *Remote Sensing of Environment*, 86(1), 83–107, doi: https://doi.org/10.1016/S0034-4257(03)00070-1.

Wooster, M. J., Roberts, G., Perry, G. L. W., & Kaufman, Y. J. (2005). Retrieval of biomass combustion rates and totals from fire radiative power observations: FRP derivation and calibration relationships between biomass consumption and fire radiative energy release. *Journal of Geophysical Research*, 110, D24311, doi: https://doi.org/10.1029/2005JD006318.

Xu, W., Wooster, M. J., Roberts, G., & Freeborn, P. (2010). New GOES imager algorithms for cloud and active fire detection and fire radiative power assessment across North, South and Central America. *Remote Sensing of Environment*, 114(9), 1876–1895, doi: https://doi.org/10.1016/j.rse.2010.03.012.

Yokelson, R. J., Burling, I. R., Gilman, J. B., Warneke, C., Stockwell, C. E., de Gouw, J., et al. (2013). Coupling field and laboratory measurements to estimate the emission factors of identified and unidentified trace gases for prescribed fires. *Atmospheric Chemistry and Physics*, 13(1), 89–116, doi: https://doi.org/10.5194/acp-13-89-2013.

Zhang, X., Kondragunta, S., Schmidt, C., & Kogan, F. (2008). Near real time monitoring of biomass burning particulate emissions (PM2.5) across contiguous United States using multiple satellite instruments. *Atmospheric Environment*, 42(29), 6959–6972, doi: https://doi.org/10.1016/j.atmosenv.2008.04.060.

Zhang, X., Kondragunta, S., Ram, J., Schmidt, C., & Huang, H.-C. (2012). Near-real-time global biomass burning emissions product from geostationary satellite

constellation. *Journal of Geophysical Research*, 117, D14201, doi: https://doi.org/10.1029/2012JD017459.

Zhang, X., Kondragunta, S., & Roy, D. P. (2014). Interannual variation in biomass burning and fire seasonality derived from geostationary satellite data across the contiguous United States from 1995 to 2011. *Journal of Geophysical Research: Biogeosciences*, 119, 1147–1162, doi: https://doi.org/10.1002/2013JG002518.

Zhang, F., Wang, J., Ichoku, C., Hyer, E. J., Yang, Z., Ge, C., et al. (2014). Sensitivity of mesoscale modeling of smoke direct radiative effect to the emission inventory: A case study in northern sub-Saharan African region. *Environmental Research Letters*, 9(7), 075002, doi: https://doi.org/10.1088/1748-9326/9/7/075002.

CHAPTER 3: Estimation of Biomass-Burning Emissions by Fusing the Fire Radiative Power Retrievals from Polar-Orbiting and Geostationary Satellites across the Conterminous United States

Li, F., X. Zhang, D. P. Roy, and S. Kondragunta, Estimation of biomass-burning emissions by fusing the fire radiative power retrievals from polar-orbiting and geostationary satellites across the conterminous United States, a paper is in preparation for a peer-reviewed journal.

This chapter address Hypothesis #2: *Diurnal FRP cycles can be reconstructed from polar-orbiting and geostationary satellites FRP retrievals to improve emissions estimation.*

Abstract

Biomass burning is an important source of atmospheric greenhouse gases and aerosols, and its emissions can be estimated using Fire Radiative Power (FRP) retrievals from polar-orbiting and/or geostationary satellites. Accurate and timely estimation of biomass-burning emissions (BBE) requires high-spatiotemporal-resolution FRP that is characterized by accurate diurnal FRP cycle. This study is to estimate hourly reliable BBE in a 0.25°×0.3125° grid across the conterminous United States (CONUS) to be used in chemical transport models for air quality forecast. To do this, this study for the first time fused FRP retrievals from the Geostationary Operational Environmental Satellite (GOES) with those from Moderate Resolution Imaging Spectroradiometer (MODIS) Collection 6 after GOES FRP was angularly adjusted and was further calibrated against MODIS FRP. The FRP data was obtained from Terra and Aqua MODIS 1-km active fire products with fire observations of four times a day and from 4km GOES WF_ABBA (WildFire Automated Biomass Burning Algorithm) fire products for GOES-W (GOES-11 and 15) and GOES-E (GOES-13) with observations every 5-15 min across the CONUS from 2011-2015. The diurnal FRP cycles at an interval of 15 min for a grid were reconstructed using the ecosystem-specific diurnal FRP climatology and actually available fused FRP, which were applied to estimate hourly BBE across the CONUS. The results indicate that the reconstructed diurnal FRP cycle varied significantly in magnitude and shape among 45 CONUS ecosystems. The biomass burning released 690 Gg particulate matter (smaller than 2.5 μm in diameter, PM2.5) in the CONUS each year; however, it presented significant temporal (diurnal, seasonal, and interannual) and spatial variations. Finally, the BBE estimates were evaluated using available data sources and

compared well (difference < 30%) with emissions derived from Landsat burned areas in the western CONUS and with hourly carbon monoxide emissions simulated using a biogeochemical model over the Rim Fire in California (difference < 30%). The BBE estimates showed similar seasonal variation to six available BBE inventories but with variable magnitude.

3.1. Introduction

Biomass burning from wildfires emits a significant amount of trace gases and aerosols that profoundly impact climate, weather, carbon budget, and public health (Akimoto, 2003; Bowman et al., 2009; Johnston et al., 2016; Kaufman et al., 2002). Global wildfires, on average, annually burn approximately 350 Mha of land (Giglio et al., 2013) and release 2.2 Pg carbon (approximately 23% of fossil-fuel carbon emissions in 2014 (Boden et al., 2017)) into the atmosphere (van der Werf et al., 2017), which has been projected to cause a net global warming of 0.4 K over 20 years by 2026 (Jacobson, 2014). Smoke aerosols (i.e., black carbon and organic carbon) emitted from biomass burning is thought to have cooled the Earth by 0.06-1.30 $W \cdot m^{-2}$ in the industrial era (Bond et al., 2013). Smoke aerosols threaten human health by degrading local to regional air quality. For example, fire-related fine particulate matter smaller than 2.5 μm in diameter (PM2.5) cause several hundreds of thousands of premature deaths worldwide annually (Johnston et al., 2016; Lelieveld et al., 2015). Biomass-burning emissions (BBE) significantly influence the accuracy of atmospheric models and numerical weather models for forecasting air quality and meteorological conditions (Reid et al., 2009). Accurate and

timely estimation of BBE is needed for climate, weather, environment, and air quality applications.

BBE has been estimated since the 1980s as the product of burned area, biomass fuel load, the fraction of biomass burned, and emission factors (Seiler and Crutzen, 1980; van der Werf et al., 2017). The degree to which these four parameters are estimated determines the accuracy of BBE estimates. Prior to the satellite era, BBE was highly uncertain and was estimated by statistical extrapolation of results from local experiments to regions and worldwide (Seiler & Crutzen, 1980; Crutzen & Andreae, 1990; Hao et al., 1990). In the satellite era, the burned area and hotspots retrieved from satellite observations have elevated the capability of quantifying BBE. Particularly, with the availability of the global systematically generated Moderate Resolution Imaging Spectroradiometer (MODIS) fire products (Justice et al., 2002), regional and global BBE products have been widely produced, including the Global Fire Emissions Database (GFED) (van der Werf et al., 2017), the Fire Locating and Modeling of Burning Emissions (FLAMBE) (Reid et al., 2009), the Fire INventory from NCAR (FINN) (Wiedinmyer et al., 2011), and the Wildland Fire Emissions Information System (WFEIS) (French et al., 2011). Although large improvements have been achieved in the estimation of burned area (Mouillot et al., 2014; Giglio et al. 2018), it is still challenging to accurately estimate BBE using the conventional model. This is due to the fact that burned areas are often underestimated by moderate-resolution satellite (Boschetti et al., 2004; Kasischke et al., 2011), and fuel loadings are static and may differ by more than 35% among different fuel datasets (Zhang et al., 2008).

Retrieval of the fire-released radiative energy from satellite radiance provides alternative ways to estimate BBE. Controlled fires experiments in laboratory and landscape demonstrated that the instantaneous radiative energy or Fire Radiative Power (FRP) is related to the rate of biomass combustion, and the total biomass combusted in a fire event is a function of the temporal integration of FRP, termed Fire Radiative Energy (FRE), and FRE biomass combustion coefficient (FBCC) (Freeborn et al., 2008; Hudak et al., 2016; Kremens et al., 2012; Wooster, 2002; Wooster et al., 2005). This empirical relationship was also confirmed in wildfires based on surface biomass consumption and satellite-derived FRP and emissions retrievals (Konovalov et al., 2014; Li et al., 2018), in which FRP is retrieved from radiances of fire pixel and non-fire ambient background at the 4-μm band (Wooster et al., 2003). The relationship has been frequently used to estimate regional to global BBE using FRP retrievals from polar-orbiting satellites and geostationary satellites (Ellicott et al., 2009; Kaiser et al., 2012; Roberts et al., 2009; Vermote et al., 2009; Zhang et al., 2012). For instance, daily global BBE is operationally produced using FRP retrievals from MODIS and global geostationary satellites in the Quick Fire Emissions Dataset (QFED) (Darmenov & Silva, 2015), the Global Fire Simulating System (GFAS)(Kaiser et al., 2012), and the Global Geostationary Satellite Biomass Burning Emissions Product (GBBEP-Geo)(Zhang et al., 2012). Another approach is to relate BBE rates directly to FRP using smoke emission coefficients (Freeborn et al., 2008; Ichoku & Kaufman, 2005). Smoke emission coefficients in a 0.1° grid globally are available in the Fire Energetics and Emissions Research (FEER) product, which can be used to convert FRP to the rate of biomass-burning emissions (Ichoku & Ellison, 2014). These smoke emission coefficients have been further refined

based on MODIS Aerosol Optical Depth (AOD) and Meteosat SEVIRI FRP retrievals and applied to estimate BBE across Africa continent (Mota & Wooster, 2017).

BBE will be estimated more reliably if satellite-based FRP is available at high spatiotemporal resolution. Sensors onboard the geostationary satellites (e.g., Meteosat SEVIRI and Geostationary Operational Environmental Satellite (GOES-11, 13, and 15) Imager) generally observe fires once from every 5-15 min. The high-temporal FRP retrievals enable to establish diurnal FRP variation (cycle), to estimate FRE and BBE at an hourly-to-daily resolution. However, their coarse spatial resolution (e.g., nominal 4 km at nadir for GOES) limits the capability of detecting small and cool fires (e.g., SEVIRI is unable to detect fires with FRP < 50 MW (Roberts & Wooster., 2008)), which could result in underestimation of FRE by 50% (Freeborn et al., 2009) and BBE by a factor of up to four (Roberts et al., 2009; Zhang et al., 2012). On the other hand, the polar-orbiting MODIS Aqua and Terra are able to sense relatively smaller and cooler fires (e.g., fire pixel with FRP > 10 MW (Roberts & Wooster., 2008)) due to higher spatial resolution of MODIS (nominal 1 km) than geostationary sensors, but each MODIS sensor only observes the same location twice a day. Thus, the polar-orbiting sensors (e.g., MODIS) are incapable of characterizing the diurnal FRP variation. Because fires have temporal fluctuations in fire radiant power, the FRE estimated by numerical integration of satellite FRP measurements is sensitive to satellite FRP undersampling during temporal gaps between two-successive fire observations (Boschetti & Roy, 2009; Kumar et al., 2011). Obviously, neither of present satellites is able to characterize the diurnal variations in FRP, or diurnal FRP cycle, accurately. Note that “diurnal FRP cycle” here is referred to as the diurnal variation of FRP per grid cell, which differs from the term of “diurnal fire

cycle" that represents the diurnal variation in the total number of active fire detections in a given region (Giglio, 2007).

Two general strategies have been attempted to derive high-spatiotemporal-resolution FRP. The first is to approximate diurnal FRP cycles with predefined Gaussian functions, and fit them to MODIS FRP retrievals (Andela et al., 2015; Ellicott et al., 2009; Konovalov et al., 2014; Vermote et al., 2009). These predefined Gaussian functions may work well for some particular regions rather than the continental to global extents because diurnal FRP cycle varies with fuel types and seasons (Andela et al., 2015; Roberts et al., 2009). The second strategy is to predict the MODIS-equivalent FRP estimates from 15-min SEVIRI FRP retrievals using the optimized SEVIRI-to-MODIS FRP ratio (Freeborn et al., 2009). However, derivation of the optimized FRP ratio requires a large number of samples cumulated in large spatiotemporal windows (i.e., 5°grid and 15 min, or 1°grid and one month) (Freeborn et al., 2009) that hardly meet the requirements of operational and near-real-time emissions inventories (Andela et al., 2015).

This study is to develop a new algorithm to estimate hourly BBE at a 0.25° latitude by 0.3125° longitude grid across the conterminous United States (CONUS) by fusing FRP from Terra and Aqua MODIS and GOES-E and GOES-W observations. This dataset is to match the spatiotemporal resolution used as emissions input in chemical transport models (e.g. GEOS-CHEM) (Bey et al., 2001; Eastham and Jacob, 2017) and in NOAA (National Oceanic and Atmospheric Administration) Environmental Modeling System (NEMS) for Global Aerosol Forecasting (Lu et al., 2016). To estimate hourly BBE, the following activities were conducted. An empirical model was developed to

adjust GOES FRP retrievals at large view zenith angle (VZA) and the adjusted GOES FRP values were further calibrated against MODIS FRP retrievals. The calibrated GOES FRP was applied to establish the diurnal FRP climatology for 45 ecosystems at a grid level, which extended the simple diurnal cycle of FRP climatology (Zhang et al, 2012). Diurnal FRP cycles at a 15-min interval in a grid were then reconstructed by fitting the ecosystem-specific diurnal FRP climatology to the fused GOES and MODIS FRP estimates, which were applied to estimate hourly BBE of PM2.5 and carbon monoxide (CO) in a grid. Finally, the BBE estimates were evaluated and validated using fire emissions calculated from fuel loadings and burned areas over 60 Landsat burned areas, obtained from eight available inventories across the CONUS, and modeled by the WRF-Chem model over the Rim Fire in California, respectively.

3.2. Methods

3.2.1. Fire Radiative Power from Polar-Orbiting and Geostationary Satellites

3.2.2.1. MODIS FRP

The MODIS active fire products provide fire detections at the satellite overpass times (Giglio et al., 2016). Terra and Aqua respectively cross the equator at approximately 10:30 AM and 1:30 PM local time during daytime and 10:30 PM and 1:30 AM during nighttime. The MODIS Level 2 active fire products (abbreviated MOD14 for Terra and MYD14 for Aqua) contain for each fire pixel the detection time, geographical coordinate, confidence (low, nominal, and high), fire radiative power (units: MW per pixel), brightness temperature at the MODIS band 21 (3.660-3.840 μm) and band 31

(10.780-11.280 μm), and average brightness temperature of the surrounding non-fire pixels at bands 21 and 31 (Giglio, 2015). FRP estimates in MODIS Collection 6 (C6) active fire product are retrieved following the method developed by Wooster et al. (2003) using the radiances of a fire pixel and its ambient background non-fire pixels at the band 21, and the fire pixel area (Giglio et al., 2016).

This study obtained the MODIS C6 Level 2 active fire products (MOD14 and MYD14) for the period of 2011-2015 from NASA Level-1 and Atmosphere Archive & Distribution System (LAADS) (https://ladsweb.modaps.eosdis.nasa.gov/). This product is defined in the MODIS sensing geometry (a 5-min granule) that covers an area of approximately 2340 by 2030 km along the scan and track directions, respectively. The MODIS scans 10 1-km lines per mirror rotation over ±55°. The pixel dimension increases from 1 km at nadir to 2.01 km and 4.83 km along the track and scan directions at the scan edge, respectively, which results in oversampling between adjacent scans by up to 50% from the scan angles of 24° to scan edge (Wolfe et al., 2002; Wolfe et al., 1998). As a result, fires can be repeatedly detected (Freeborn et al., 2014; Peterson et al., 2013). Further, the duplicate fire detections can also result from the triangle-shaped point spread function (PSF) of MODIS (Freeborn et al., 2014). Accordingly, this study corrected the inter-scan duplicate fire detections using the approach proposed by Li et al (2018a). Specifically, fire pixels were considered as duplicate detections in consecutive scans (one detection per scan) if they met the following conditions: (1) Fires were detected at the same satellite view angles. (2) Time difference between any two detections was less than 8 seconds because the same point on the Earth surface could be sensed by up to three temporally MODIS adjacent scans at the scan edge during a time period of 4.431seconds

(1.477 seconds per scan × 3 scans) (Wolfe et al., 2002). (3) The distance between the centers of any pair of fire detections was shorter than the along-track dimension of the fire pixels because adjacent scans primarily overlapped each other along the track direction. For each pair of duplicate detections, one of them remained while the other was removed, in which the average FRP was used for the retained detection.

3.2.2.2. GOES FRP

The WildFire Automated Biomass Burning Algorithm (WF_ABBA Version 65) active fire product is produced from observations by the Imager sensor onboard the GOES satellites located at 135° W (GOES-W) and 75° W (GOES-E) above the equator, respectively (Schmidt and Prins, 2003). The pixel size in GOES-W (GOES-11 and 15) and GOES-E (GOES-13) increases from 4 to 8 km as the associated view zenith angle (VZA) varies from 30° to 70° across the CONUS. On routine-scanning schedule, the GOES-W senses the central and Western CONUS every 5-15 min (the 0th, 10th, 15th, 30th, 40th, and 45th min of every hour approximately), and the GOES-E observes the whole CONUS every 15 min (the 0th, 15th, 30th, and 45th min of every hour approximately) (http://www.ospo.noaa.gov/Operations/GOES/schedules.html). The WF_ABBA detects active fires from all these observations. In WF_ABBA, false alarms due to cloud impacts, very large VZA, and sensor noise are reduced by applying a temporal filter that considers a new fire pixel as a false alarm if it has been detected less than twice during the past 12 hours (Schmidt and Prins, 2003). The GOES WF_ABBA product provides, for each fire pixel, fire location (longitude and latitude), time, FRP,

VZA, pixel size, brightness temperature at the 4 μm and 11 μm bands, fire temperature, fire size, ecosystem type, and quality flag. The quality flag is divided into six categories: flag 0 – a good quality fire detection, flag 1 – a fire detection with saturated brightness temperature of the 4-μm band, flag 2 – a fire detection contaminated by clouds or thick smoke plumes, flag 3 – a high possibility fire detection, flag 4 – a moderate possibility fire detection, and flag 5 – a low possibility fire detection. FRP is not retrieved for a detection classified as flags 1, 2, or 5. The ecosystem type for a fire pixel is determined based on the U.S. Geological Survey (USGS) Global Land Cover Characterization (GLCC) data set, which contains 100 ecosystem types globally and 45 primary ecosystems across the CONUS. The GLCC was generated using 1-km AVHRR (advanced very high resolution radiometer) data from April 1992 to March 1993 (Brown et al., 1999).

This study obtained the filtered GOES WF_ABBA active fire product for the period of 2011-2015 from NOAA (http://satepsanone.nesdis. noaa.gov/pub/FIRE/forPo/). Note that the WF_ABBA fire data from July to August 2012 was missing due to the failure of collecting it from NOAA operational website so that the analyses for the year 2012 were excluded. Hereafter, the period of 2011-2015 represents 2011, 2013, 2014, and 2015. This product contains fire detections from GOES-W (GOES-11, replaced by GOES-15 since December 2011) and GOES-E (GOES-13). Approximately 56% of GOES fire detections from 2011 to 2015 were classified as low possibility fire detections (flag 5) which were false alarms in most cases. Therefore, fire pixels with quality flags of 0, 1, 2, or 3 were used and a fire pixel categorized as flag 4 or 5 was considered only if it was detected at least three times per day or at least once with a flag value < 3.

3.2.2. Adjustment of GOES FRP at Large View Zenith Angles

The variation of GOES FRP with satellite view zenith angle (VZA) was investigated and adjusted because the FRP over large VZA might be influenced by the increased radiance contributed by non-fire background over a large pixel. To do this, GOES-W FRP and GOES-E FRP were compared by selecting the contemporaneous fire pixels that were detected by these two satellites within ±5 min in a 0.1° grid (~7 - 10 km across latitudes 10° - 50°). The comparison was conducted in two steps. First, all spatiotemporally coincident fire detections were obtained if the VZA was the same from GOES-W and GOES-E during 2013 - 2014 in order to verify the similarity of their FRP retrievals. These fire detections were located within 0.1° grids around the105° W longitude line. The selected samples demonstrated that FRP observations from the two GOES satellites were equivalent with a slope of 0.96 and a coefficient of determination of 0.94 (Figure 3-1).

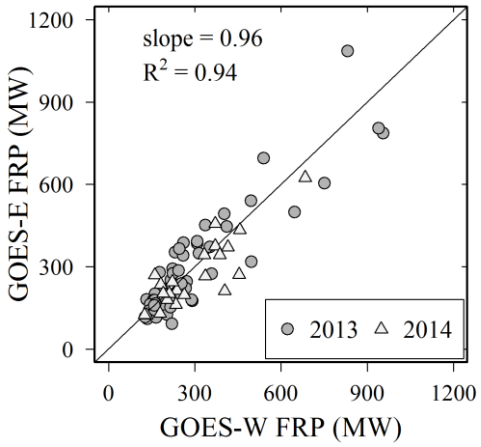

Figure 3-1. Comparison of GOES-E FRP with GOES-W FRP for coincident detections (within ±5 min) collected within 0.1° grids around the 105° W longitude line from 2013 to 2014. The solid line is the 1:1 line.

Second, the contemporaneous fire detections were selected from GOES-W with VZA ranging from 40° to 50° (pixel size from 4.8 to 5.5 km) and GOES-E with VZA varying from 30° to 70° (pixel size from 4 to 8 km) in order to quantify the FRP variation with VZA. Considering GOES-W FRP as a reference and ignoring the small variation of VZA-related pixel size, the ratio of GOES-E to GOES-W FRP was compared to the VZA variation from 30° to 70° (Figure 3-2). Then the empirical model was established as:

$$R(\theta) = \frac{FRP_E}{FRP_W} = a + \frac{b}{c\theta + d} \tag{3}$$

where $R(\theta)$ is the ratio of GOES-E FRP (FRP_E) to GOES-W FRP (FRP_W), θ is GOES-E VZA (radian), and the parameters (a, b, c, and d) are coefficients obtained by fitting median FRP ratio (Figure 3-2).

Giving that GOES-E FRP and GOES-W FRP are equivalent at the same VZA as demonstrated in Figure 3-1, the FRP influenced by VZA could be adjusted using the equation (4) that was deduced from equation (3):

$$FRP_{adj} = \frac{FRP_\theta}{R(\theta)} \tag{4}$$

where FRP_{adj} is the adjusted FRP and FRP_θ is the GOES fire FRP observed at VZA of θ. For convenient purpose, hereafter the adjusted GOES FRP is simply referred to as GOES FRP.

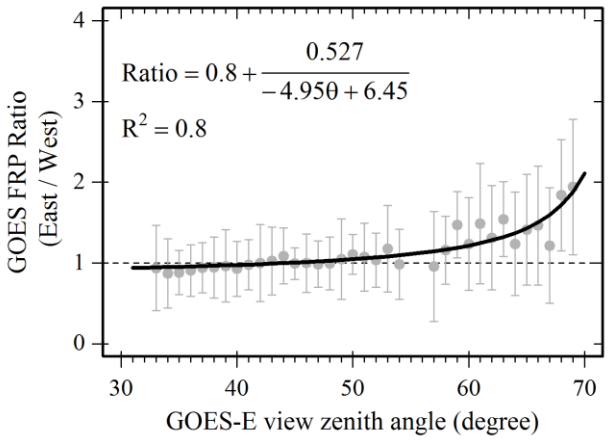

Figure 3-2. FRP ratio of GOES-E to GOES-W as a function of GOES-E VZA. The filled gray cycles are the median ratio at every 1-degree VZA from 30° to 70°, and one standard deviation was added as error bars. The black solid line is the fitted model and the dashed line is the FRP ratio with a value of 1.0.

3.2.3. Calibration of GOES FRP against MODIS FRP

GOES FRP was calibrated by comparing with MODIS FRP. It is due to the fact that MODIS FRP is of higher quality and capable of representing relatively small and cool fires (Schroeder et al., 2010; Xu et al., 2010). To establish calibration models (or coefficients), GOES FRP was compared to MODIS FRP, where both the GOES and MODIS FRP were contemporaneously detected over 628 fire events that occurred during three years from 2013 to 2015 across the CONUS. The burned area perimeters of these fire events, ranging from 2.3 km^2 to 884.4 km^2, were obtained from the Monitoring Trends in Burn Severity (MTBS) project (http://www.mtbs.gov/), which were determined

using 30 m Landsat Thematic Mapper (TM) or Enhanced Thematic Mapper Plus (ETM+) datasets (Eidenshink et al., 2007). The 628 MTBS burned areas were further stratified based on the dominant land cover type in a burned area: forests, shrublands, savannas, grasslands, and croplands. For each MTBS burned area, the contemporaneous GOES and MODIS FRP retrievals were obtained from the active fire pixels that were detected by GOES and MODIS with a time difference of less than 5 min within the MTBS burned area and its surrounding 5-km buffer zone. As a result, all the contemporaneous GOES and MODIS FRP retrievals around four MODIS observations (at 1:30 AM, 10:30 AM, 1:30 PM, and 10:30 PM local time) were selected each day. The contemporaneous GOES and MODIS FRP retrievals were further aggregated, respectively, for each of the 628 MTBS burned areas.

The land-cover specific calibration coefficients for GOES FRP were derived using a simple ordinary least squares regression with the aggregated MODIS FRP estimate as a dependent variable and the aggregated GOES FRP as an independent variable in each group of the stratified MTBS burned areas (Table 3-1).

Table 3-1. Calibration coefficients for five land cover types

Land cover type	Calibration coefficient	r^2	Number of fires
Forest	2.06*	0.90	304
Shrublands	1.45*	0.92	55
Savannas	1.77*	0.95	46
Grasslands	1.12*	0.81	176
Croplands	1.13*	0.90	47

* *p*-value < 0.001

Finally, the calibration coefficients were applied to calibrate GOES FRP at a 0.25°×0.3125° grid. In a grid cell, GOES FRP with the same GLCC ecosystem observed at a given time was aggregated from detections. The aggregated FRP was then calibrated using calibration coefficients (Table 3-1) after each GLCC ecosystem was reclassified to one of the five land cover types by a cross-walking method. Hereafter the resultant GOES FRP at a 0.25°×0.3125° grid resolution was simply referred to as calibrated GOES FRP.

3.2.4. Fusion of MODIS FRP with the Calibrated GOES FRP

MODIS FRP was aggregated at a 0.25°×0.3125° grid and fused with the calibrated grid GOES FRP in the same GLCC ecosystem. Similar to the aggregation of GOES FRP at a given time, MODIS FRP was aggregated by summing FRP from all MODIS detections with the same GLCC ecosystem within each grid cell, which was referred to as grid MODIS FRP hereafter. Then, the grid FRP from MODIS and GOES was fused in each 15-min bin during a day using the following equation:

$$\overline{FRP} = \frac{FRP_{MODIS} + FRP_{GOES}}{n} \tag{4}$$

where $\overline{FRP}$ is the fused grid FRP within a 15-min bin, FRP_{MODIS} and FRP_{GOES} are respectively the grid MODIS FRP and the calibrated grid GOES FRP, n=2 if both FRP_{MODIS} and FRP_{GOES} are valid, and n=1 if only FRP_{MODIS} or FRP_{GOES} was available.

3.2.5. Reconstruction of Diurnal FRP Cycles

3.2.5.1. Establishment of diurnal FRP climatology

The climatology of diurnal GOES FRP was established to predict FRP for temporally missing observations caused by obscuration of clouds, very thick smoke plume, and detection capability of sensors. Because fire properties and behaviors could differ greatly among ecosystems, which are related to fuel characterizations (availability, amount, and spatial distribution, etc.) and thus are linked to fire activity (e.g., fire type and intensity) (Pausas and Ribeiro, 2013), the diurnal FRP climatology was investigated separately for different GLCC ecosystems. Since more than 95% of GOES active fires were observed in 18 of 45 primary GLCC ecosystems across the CONUS, the related 18 ecosystems were selected separately, and the rest (37 types) was combined into one type. Thus, a total of 19 ecosystem types were divided. The diurnal FRP climatology for each ecosystem was generated based on the following steps. First, for each 15-min bin, the calibrated GOES FRP values in each grid cell across the CONUS from 2011 to 2015 were grouped at an interval of every 20MW. Next, the probability density of FRP observations in each group was estimated using a kernel density estimation approach (Venables and Ripley, 2002). The groups with GOES FRP density less than 0.05% of the maximal group density within a specific 15-min bin were then removed because small samples could greatly bias FRP estimates. Finally, the mean FRP was calculated from the remaining GOES FRP values every 15 min, which was used to determine the diurnal FRP climatology for each ecosystem.

The monthly maximum diurnal burning duration (MMDBD, hours) was further calculated, which was used to quantify the potential fire duration during a day. The MMDBD was defined as the longest period that active fires could be detected by satellites during a day, which represents the temporal boundaries of the satellite

detectable fires. The MMDBD could vary with fuel, fire weather, and fire types. The climatological MMDBD was calculated by extracting the mean timings of the earliest and latest ten GOES fire detections (including fire detections without FRP retrievals) during 2011-2015. As a result, the MMDBD was also calculated for the 19 ecosystem types.

In addition, the hourly and monthly possibility of GOES fire detection was also derived for the 19 ecosystem types. It is the percentage of fire detections sensed by GOES every hour during a day or every month in a year, which indicates the diurnal and seasonal possibilities of the occurrences of fires.

Both the ecosystem-specific MMDBD and the hourly and monthly possibility of GOES fire detection provide statistical information to determine the potential burning duration of a fire in Section 2.5.2.

3.2.5.2. Reconstructing diurnal FRP cycles

Diurnal FRP cycles were reconstructed from the fused grid FRP and diurnal FRP climatology at a 0.25°×0.3125° grid for each ecosystem based on the following two steps:

1. The fused grid FRP ($\overline{FRP}$, see section 2.4) was fitted to the FRP climatology in the same ecosystem by shifting an offset. By assuming that the shapes of diurnal FRP cycles were similar for a given ecosystem, the offset was calculated using a least square method from a set of $\overline{FRP}$ observations and the corresponding values on the diurnal FRP climatology curve. Thus, the shifted FRP climatology represents the potential diurnal FRP curve for the $\overline{FRP}$ observations.

2. Missing FRP values in temporal gaps were predicted using the shifted FRP climatology. A temporal FRP gap was the period of one or more consecutive 15-min bins in which $\overline{FRP}$ observations were not available. Because fires (except for large forest fires) could only burn continuously a few hours instead of an entire day in a grid, the length of a temporal gap was determined based on the ecosystem-specific MMDBD and the hourly and monthly possibility of GOES fire detection. The possibility of fire occurrence generally is stronger in the early afternoon and during fire seasons when fire weather is more favorable for combustion, and more fuels are available to burn (Giglio et al., 2006; Giglio 2007). Therefore, a fire most likely burns longer during the time periods with the stronger possibility of fire detections than the other time periods. For each $\overline{FRP}$ observation, a fire was assumed to burn continuously for:

   (a) one hour before and after the fire observation (with and/or without FRP retrievals), respectively, if the observation was collected in the early afternoon (13:00-15:00 local solar time) during fire seasons;

   (b) 30 minutes if the observation was collected in other hours during fire and non-fire seasons, and it was located within MMDBD (section 2.5.1);

   (c) 15 minutes if the observation was located outside of MMDBD. This is because a fire seldom occurs (or too small/cool to be detected) in hours beyond the MMDBD.

   At these temporal gaps, the shifted FRP climatology was selected as predictions. Finally, a diurnal FRP cycle was obtained from a combination of actual $\overline{FRP}$ observations and $\overline{FRP}$ predictions.

3.2.6. Estimation of FRE and Biomass-Burning Emissions

FRE was estimated for each grid cell from diurnal FRP cycles. Fires in each 15-min bin were assumed to burn consistently with a $\overline{FRP}$ value so that the total hourly FRE in a grid was estimated as:

$$FRE = \sum_{i=1}^{p} FRE_i = \sum_{i=1}^{p} \left[\sum_{j=1}^{q} (\overline{FRP}_{i,j} \times 900) \right] \quad (5)$$

where *FRE* is the hourly fire radiative energy (FRE), FRE_i is hourly GOES-MODIS FRE in the *i*th ecosystem, *p* (p=19) is the number of ecosystems where active fires were detected in a grid by GOES and/or MODIS, $\overline{FRP}_{i,j}$ is the reconstructed diurnal fire radiative power (MW) in the *j*th 15-min bin (900 s) and the *i*th ecosystem, and *q* (*q*=4) is total number of 15-min bin within one hour.

The FRE estimated from diurnal $\overline{FRP}$ cycles is referred as to "GOES-MODIS FRE". It was used to calculate grid-level biomass-burning emissions, which is referred as to "GOES-MODIS BBE", using the following equation:

$$BBE_{FRE} = \sum_{i=1}^{p} \left(BC_i \times EF_i \right) = \sum_{i=1}^{p} \left(\beta \times FRE_i \times EF_i \right) \quad (6)$$

where BBE_{FRE} is total hourly emissions (kg) for a grid cell, BC_i and EF_i are hourly biomass consumption (kg) and PM2.5 or CO emissions factor for the *i*th ecosystem (a total of *p* ecosystems that is the same as equation (5)) in a grid cell, respectively. The emission factor was adopted from the GFED4 (Table 3-2) (van der Werf et al., 2017) that were compiled based on (Akagi et al., 2011; Andreae and Merlet, 2001). Because

emission factor is only available for five land cover types (Table 3-2), the ecosystem specific emission factor in equation (6) was obtained by cross-walking GLCC classes to these land cover types. β is the FRE biomass combustion coefficients (FBCC, 0.368 kg/MJ) (Wooster et al., 2005), and FRE_i is hourly GOES-MODIS FRE in the ith ecosystem. Note that both PM2.5 and CO estimates present very similar temporal and spatial pattern because their only difference is emission factors so that only PM2.5 estimates are presented in detail in the result section. The CO is only discussed in order to improve the evaluation of GOES-MODIS BBE estimates (c.f. Sections 2.7.3 and 3.5).

Table 3-2. Emission factors (units: $g \cdot kg^{-1}$) of PM2.5 and CO

Emission species	Forest	Savanna, Shrubs, grasslands	Croplands
PM2.5	12.9	7.17	6.26
CO	88.0	63.0	102.0

3.2.7. Evaluations of Biomass-Burning Emissions

Because of the lack of ground truth emissions, GOES-MODIS BBE was evaluated by comparing with other datasets. These datasets were: (1) BBE modeled using Landsat burned area and fuel loadings, which was called Landsat BBE; (2) existing emissions inventories; (3) the hourly BBE simulated by a biogeochemical model.

Comparison of GOES-MODIS BBE with Landsat BBE

GOES-MODIS BBE was first evaluated by comparing with Landsat BBE using the simple ordinary least squares regression. Because estimations of GOES-MODIS BBE and Landsat BBE applied the same emission factors, the evaluation of GOES-MODIS

BBE was conducted by comparing GOES-MODIS FRE based biomass consumption (BC) with Landsat burned area based BC. Landsat BC was calculated in a set of burned areas. Specifically, a Landsat burned area (corresponding to a fire event) was selected if the MODIS and GOES active fire detections covered more than 95% of the burned area, which minimized the effect of missing detections from MODIS and GOES observations. As a result, a total of 60 qualified burned areas were extracted in 2013 and 2014, which were located in the Western CONUS.

In a Landsat burned area, the BC was estimated using the conventional model (*Seiler and Crutzen*, 1980) as:

$$BC_{Landsat} = \sum_{t=1}^{n} \sum_{k=1}^{3} A_{t,k} M_{t,k} C_{t,k} \quad (7)$$

where $BC_{Landsat}$ is the total biomass consumption (kg), A is the Landsat burned area (km^2), M is FCCS (Fuel Characteristic Classification System) fuel loading ($kg \cdot m^{-2}$), C is the combustion completeness (unitless: 0-1), t is FCCS fuelbed category, n is the number of fuelbed categories, and k is MTBS burn severity class.

The three parameters in equation (7) were calculated in the same way as Li et al (2018b). Specifically, the burned area A was calculated from three Landsat MTBS severity classes (low, moderate, and high). Fuel loading M was obtained from the FCCS 3.0 that provides a 30-m fuelbed map and an associated lookup table of fuel loadings (http://www.fs.fed.us/pnw/fera/fccs/maps.shtml) for the year 2008. The FCCS 3.0 has 250 fuelbeds, and each fuelbed is separated into one or up to 18 categories (Ottmar et al., 2006). The study used the burn-severity-specific combustion completeness values (Li et al., 2018b) that were obtained by summarizing the published values associated with burn

severity (Campbell et al., 2007; Ghimire et al., 2012) because burn severity reflects the degree of above-ground organic matter consumption from fire and relates to changes in living and dead biomass (Eidenshink et al., 2007; Keeley, 2009).

3.2.7.1. Comparison of GOES-MODIS BBE with existing emissions inventories

The monthly and annual PM2.5 in GOES-MODIS BBE from 2011 to 2015 were compared to existing six global emission inventories (GFED4, GFASv1.0 and v1.2, QFEDv2.4r6, and FINNv1.5, FEERv1.0g1.2, and FLAMBE) and two regional inventories (WFEIS0.5, and NEI 2011&2014) across the CONUS (Table 3-3). Note that the GFAS product contains two different versions for the period of 2011-2015: GFASv1.0 is available from January 2011 to September 2014 and the GFASv1.2 with better quality control covers from October 2014 to December 2015.

Table 3-3. Six global and two United States emissions inventories.

Inventories	Scale & Resolution	Source data	References & products sites
GFED4	Global 0.25˚×0.25˚, monthly	Burned area (MCD64A1), Fuel loadings (biogeochemical modeled)	van der Werf et al., 2017 Giglio et al., 2013 http://www.falw.vu/~gwerf/GFED/GFED4/
GFASv1.0&1.2	Global 0.5˚×0.5˚ & 0.1˚×0.1˚, daily	MODIS FRP (MOD14/MYD14)	Kaiser et al., 2012 http://join.iek.fz-juelich.de/macc/access
FINNv1.5	Global 1 km, daily	Burned area (MOD14/MYD14, MCD12Q1), Fuel loadings (literatures)	Wiedinmyer et al., 2011 http://bai.acom.ucar.edu/Data/fire/
FLAMBE	Global 1-4 km, hourly	Burned area (WF_ABBA GOES, MOD14/MYD14), Fuel loadings (literatures)	Reid et al., 2009 (personal communication)
QFED2.4r6	Global 0.25˚×0.3125˚, daily	MODIS FRP (MOD14/MYD14)	Darmenov and Silva., 2015 ftp://ftp.nccs.nasa.gov/aerosol/emissions/QFED/v2.4r6/
FEERv1.0g1.2	Global 0.1˚×0.1˚, daily	GFAS1.2 FRP flux, emissions coefficients	Ichoku and Ellison., 2014 http://feer.gsfc.nasa.gov/data/emissions/
WFEISv0.5	United States (CONUS & Alaska)	Burned area (MCD64A1) Fuel loadings (FCCS)	French et al., 2014 http://wfis.mtri.org
NEI	United States (county & States), annual	Observations from ground facilities and satellites	https://www.epa.gov/air-emissions-inventories/

3.2.7.2. Comparison of GOES-MODIS BBE with model-simulated BBE

GOES-MODIS BBE was further evaluated using the model-simulated BBE in the Rim Fire. The Rim Fire is the third largest fire event in the California fire records. The model-simulated hourly BBE (CO emissions) was estimated using the Weather Research and Forecasting model coupled with Chemistry (WRF-Chem) (Saide et al., 2015), in which aerosol optical depth (AOD) was observed from ground-based Aerosol Robotic Network (AERONET), airborne sensors, and MODIS over the Rim Fire from 21 to 27 August 2013. The airborne observations (AOD and CO) were collected by the NASA DC-8 flights during eight hours from 26 (18:00 UTC) to 27 (02:00 UTC) August 2013 (Toon et al., 2016). This BBE dataset was obtained by personal communication. The model-simulated CO emissions were compared to GOES-MODIS BBE (CO) on an hourly basis.

3.3. Results

3.3.1. Fusion of GOES FRP with MODIS FRP

Fused FRP greatly improves the FRP values in GOES observations. Figure 3-3, as an example, shows that GOES FRP is smaller than MODIS FRP by 62%, but the magnitude of fused FRP is similar to that of MODIS FRP with a difference of 13% in the Rim fire 2013. The fused FRP is temporally distributed every 15 min while the observations in MODIS FRP are only around four times a day.

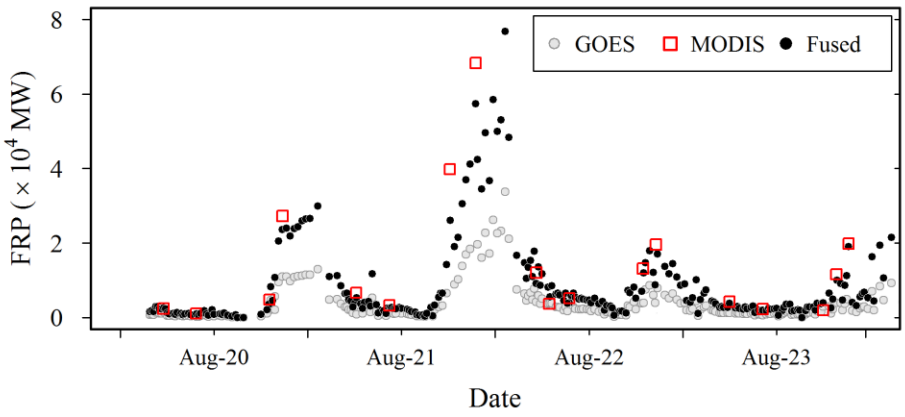

Figure 3-3. Diurnal variations of GOES FRP, MODIS FRP, and fused FRP ($\overline{FRP}$) over the Rim Fire from 20 to 23 August 2013.

3.3.2. Diurnal FRP Cycles

Diurnal FRP climatology varies among 18 ecosystems (Figure 3-4a-c) and the combination of other 37 ecosystems (Figure 3-4d). The climatology typically presents a peak during 13:00-16:00 (local solar time) and a trough during 6:00-8:00 (local solar time). Diurnal variations of FRP climatology are large in the cool conifer forest ecosystem and shrub-related ecosystems (Figure 3-4a-b) while they are small in the deciduous broadleaf forests, mixed forests, and crop-related ecosystems (Figure 3-4a, c).

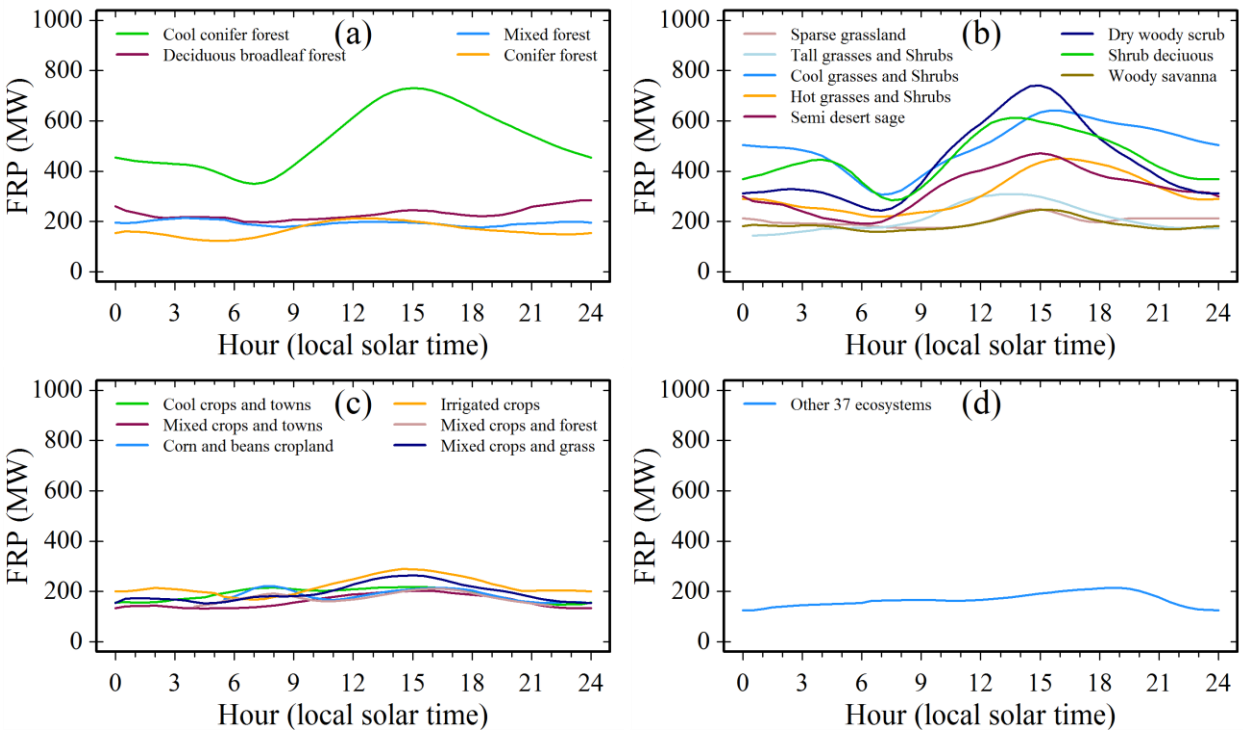

Figure 3-4. Ecosystem-specific diurnal FRP climatology across the CONUS: (a) four GLCC forest ecosystems, (b) eight GLCC grass, shrub, and savanna ecosystems, (c) six GLCC crop ecosystems, and (d) the combination of other GLCC 37 ecosystems.

Monthly maximum diurnal burning duration (MMDBD) varies temporally among ecosystems. The variation is illustrated using the example of MMDBD in three ecosystems (Figure 3-5). Generally, MMDBD is longer in peak fire season. The longest MMDBD is mainly from 6:00 to 21:00 (local time) in tall grasses and shrubs, and 0:00-24:00 (local time) in both mixed forests and cool conifer forests. However, MMDBD in cool conifer forests on average is longer than that in mixed forest, and fires burn more frequently in evening and early morning in cool conifer forests than mixed forests. The seasonal variation in MMDBD is very large in tall grasses and shrubs and mixed forests.

For instance, MMDBD in mixed forests during winter months can be 6 hours shorter than that in summer months.

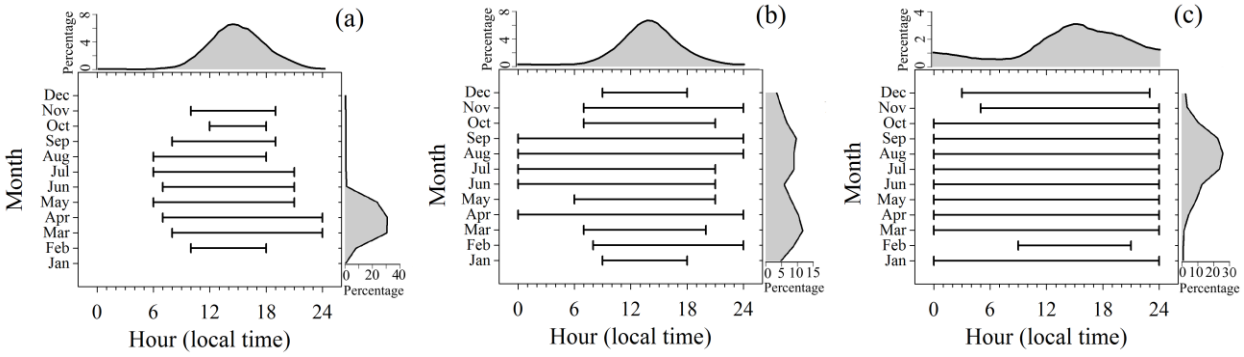

Figure 3-5. Monthly maximum diurnal burning duration (MMDBD) and hourly and monthly density of GOES active fire detections in three ecosystems: (a) tall grasses and shrubs, (b) mixed forests, and (c) cool conifer forests. The black lines are MMDBD, and the horizontal and vertical densities are proportions (in percentage) of GOES active fire detections at an interval of an hour and a month, respectively.

The reconstructed diurnal FRP cycle consists of the fused FRP and the predicted FRP in temporal gaps. Figure 3-6 shows a diurnal FRP cycle reconstructed from the fused FRP and the associated diurnal FRP climatology for a wildfire burned on 2 August 2014 in a grid in Northern California. The climatological FRP is smaller than the fused FRP by 51 MW on average. FRP is predicted for a total of 52 15-min gaps that mainly resulted from many fire observations without FRP retrievals due to the obscuration of thick smoke plumes, especially during the period between 14:00 and 19:00.

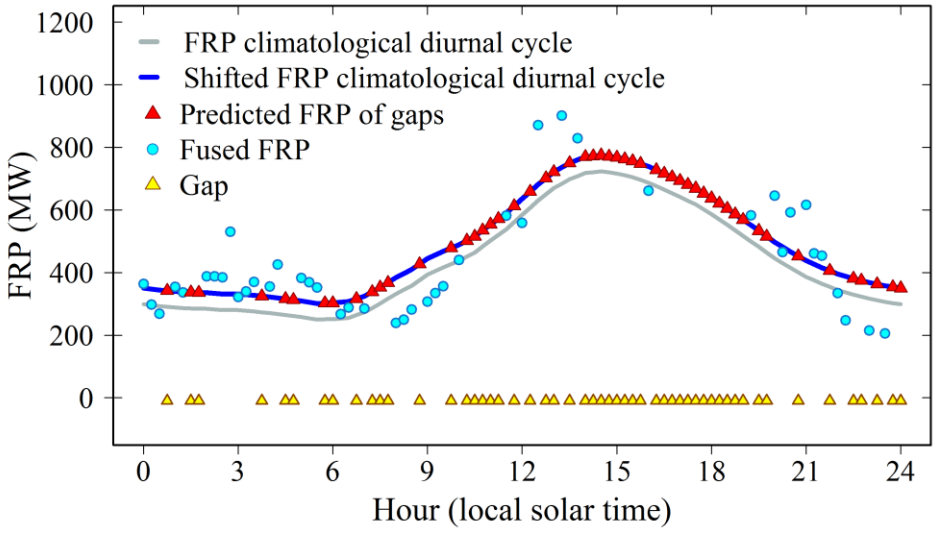

Figure 3-6. An example of reconstructing diurnal FRP cycle for a wildfire burned on 2 August 2014 in a grid centered at (41.375°N, 122.968°W) in Northern California. The grid is dominated by the cool conifer ecosystem. The reconstructed diurnal FRP cycle consists of the fused FRP (blue cycles) and the predicted FRP (red triangles) in 15-min gaps (yellow triangles).

3.3.3. Spatial Distribution of the PM2.5 Emissions

Biomass burnings annually release on average 690 Gg PM2.5 emissions across the CONUS in the four years of 2011, 2013, 2014, and 2015 (Figure 3-7). The PM2.5 emissions are spatially contributed by a mixture of fires in forests, shrubs, and grasses in the Western CONUS (382 Gg or 55%), agriculture and forest fires in the southeastern CONUS (110 Gg or 16%), prairie grass fires in Kansas and Oklahoma states (37 Gg or 5.4%) in the central CONUS, and agriculture burnings in the Mississippi River Valley (48 Gg or 7%) in the central south CONUS. However, the PM2.5 emissions are very limited in the northeastern CONUS.

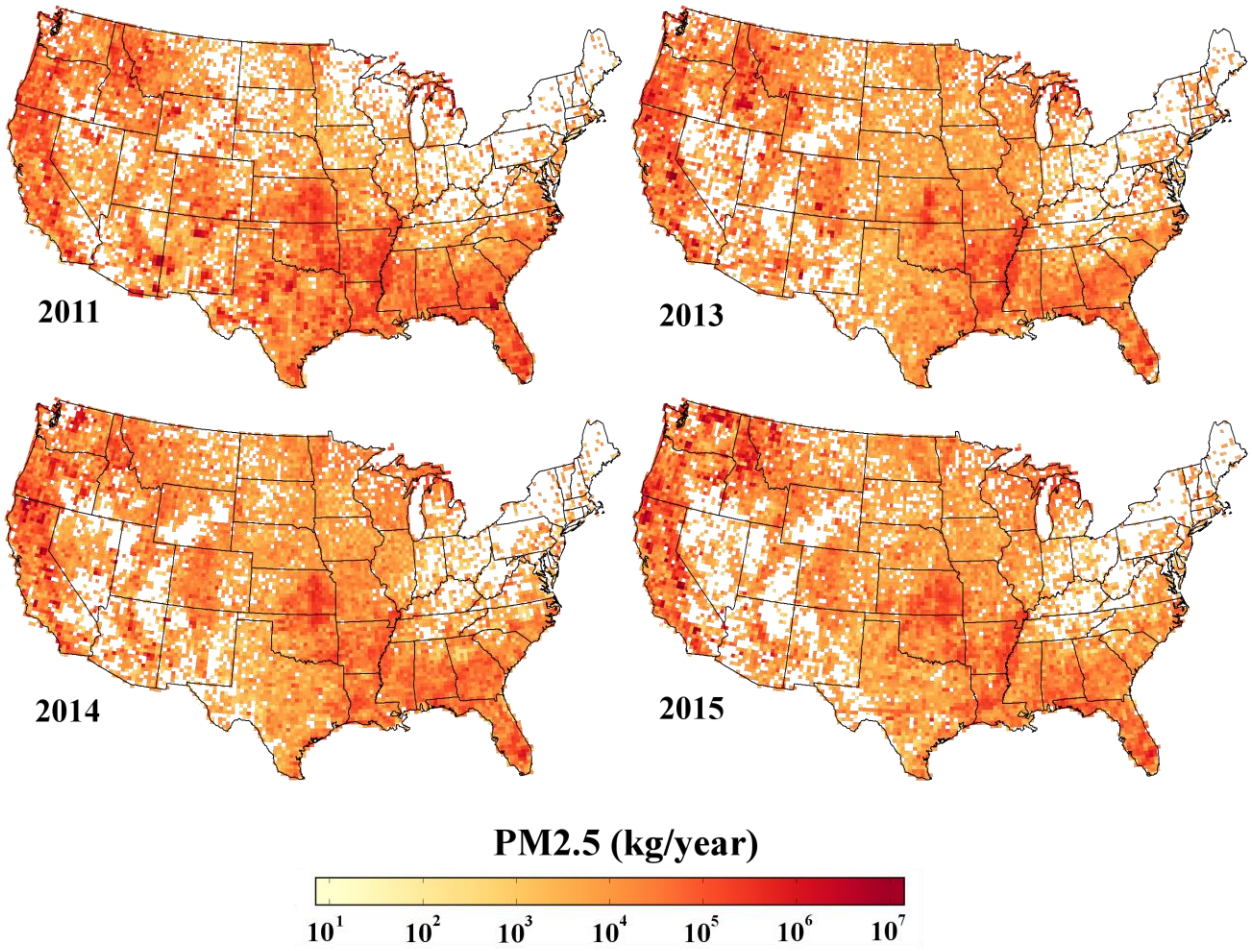

Figure 3-7. Annual PM2.5 emissions at a 0.25°×0.3125° grid across the CONUS in four years of 2011, 2013, 2014, and 2015.

PM2.5 emissions vary greatly among CONUS states (Figure 3-8). The high mean annual PM2.5 emission appears in five Pacific Northwest states: California (105 Gg), Idaho (51 Gg), Washington (49 Gg), Oregon (39 Gg), and Montana (34 Gg). The total PM2.5 emissions in these states and California alone accounts for 40% and 13.6% of the annual PM2.5 in the CONUS, respectively. They are followed by the PM2.5 emissions in three southwest states (Texas: 43 Gg, Arizona: 34 Gg, and New Mexico: 21 Gg), and three southeast states (Florida: 34 Gg, Arkansas: 30 Gg, and Georgia: 26 Gg). During the

four years, the highest PM2.5 appears in 2015 and 2011, particularly in the Pacific Northwest states, and most southwest and southeast states.

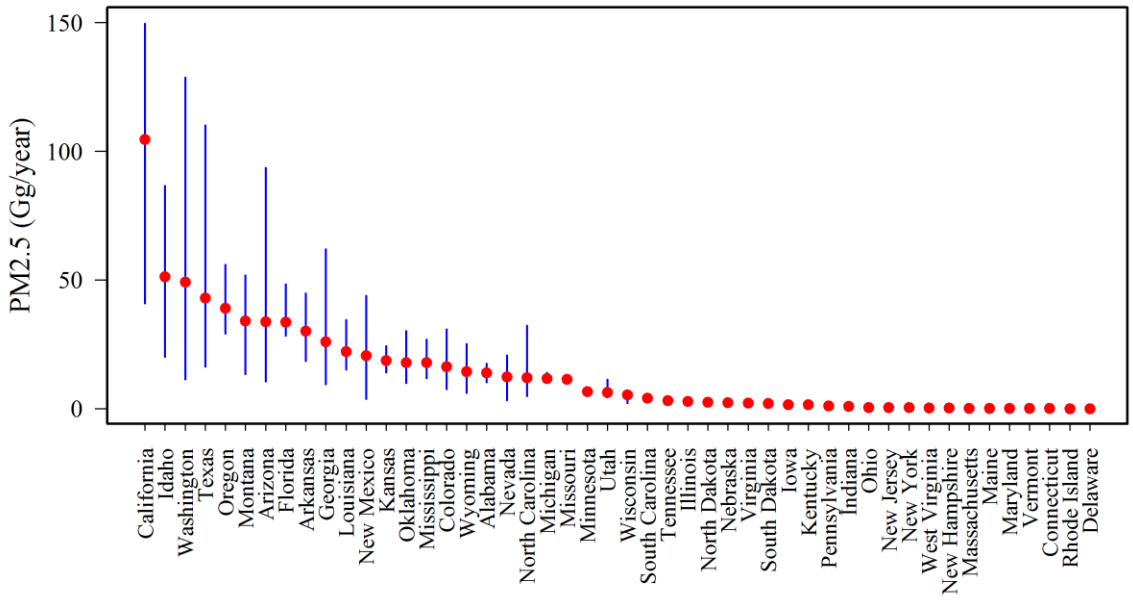

Figure 3-8. Annual mean PM2.5 emissions in 48 states in four years of 2011, 2013, 2014, and 2015. The red dots represent annual mean PM2.5 emission and the vertical bars (in blue) show the maximum and minimum of annual PM2.5 emission in each state.

Annual PM2.5 emissions differ among land cover types (Figure 3-9). The biomass burnings are on average 6.5% (45 Gg), 23% (158Gg), and 70.5% (487 Gg) in the croplands, grasslands-shrublands-savannas, and forests, respectively.

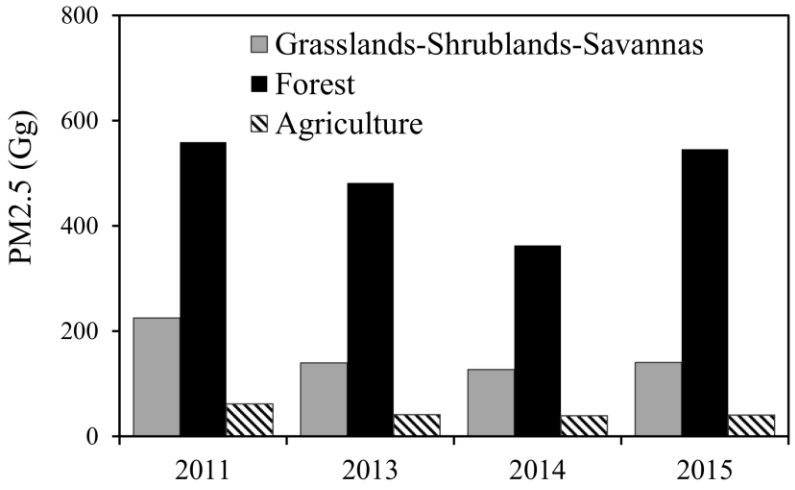

Figure 3-9. Annual PM2.5 emissions in land cover types: croplands, forests, and grasslands-shrublands-savannas in four years of 2011, 2013, 2014, and 2015.

3.3.4. Temporal Variation in the PM2.5 Emissions

PM2.5 emissions display a strong diurnal variation across the CONUS (Figure 3-10). The PM2.5 emissions with all ecosystems as a whole show a unimodal diurnal variation, which increases sharply at local time 9:00, reach the peak between 13:00 and 14:00, and then decrease until the midnight. The diurnal variations in forests, croplands, and savannas-shrublands-grasslands display a single peak approximately between 13:00 and 14:00. The PM2.5 estimates in daytime (6:00-18:00) differ considerably from the nighttime (18:00-6:00). Overall, the daytime PM2.5 emissions are 274% of the nighttime emissions but this discrepancy varies with ecosystem. The daytime emissions account for 83% in grasslands, savannas and shrublands, and 94% in croplands. In forests, approximately 90% and 10% of PM2.5 emissions are released during daytime and nighttime, respectively, in the eastern CONUS, whereas the nighttime burnings

(especially from 18:00 to 24:00) in the Western CONUS contribute 34% of PM2.5 emissions.

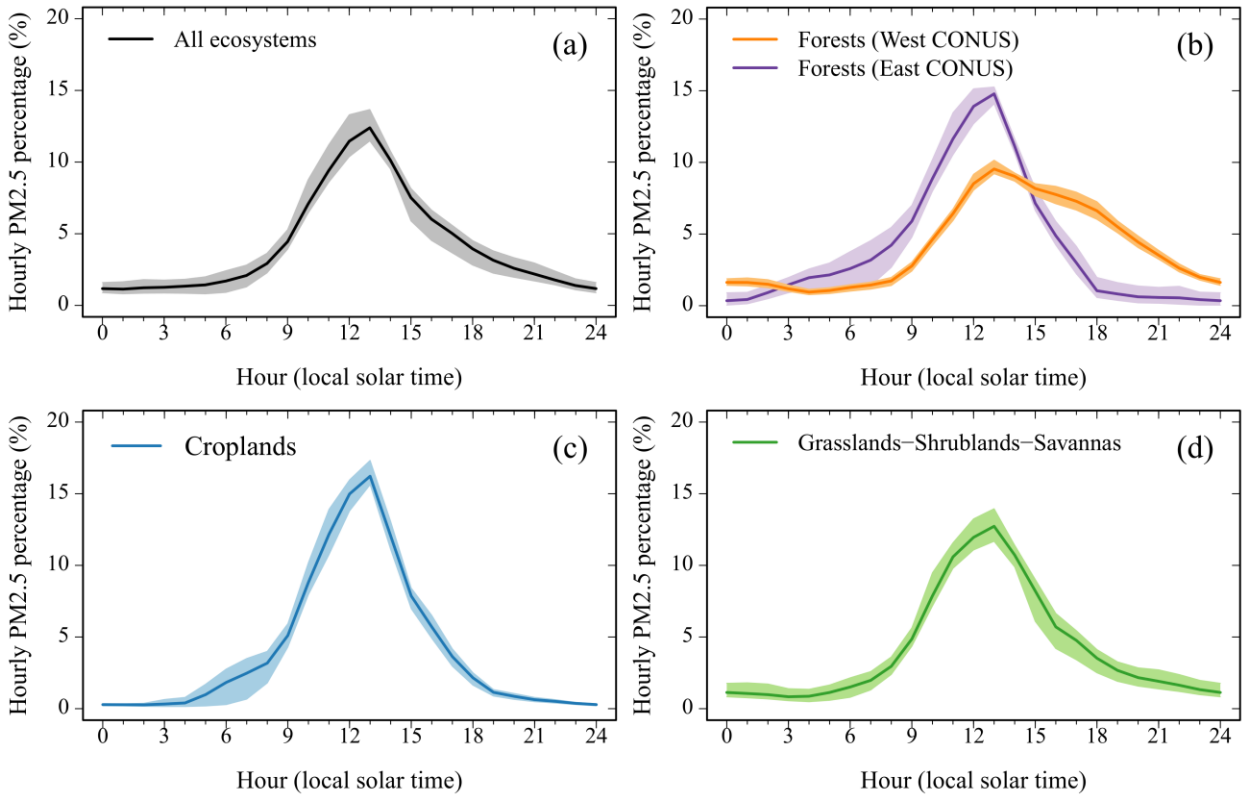

Figure 3-10. Diurnal variation of PM2.5 emissions across the CONUS. The solid line is the four-year mean PM2.5 emissions in every hour, and the shading area represents inter-annual variation. (a) All ecosystems, (b) forests (forests were divided by 100°W longitude line into two groups: west and eastern CONUS because of the distinct difference in fire characteristics in two groups (Malamud et al., 2005)), (c) croplands, and (d) a combination of grasslands, shrublands, and savannas.

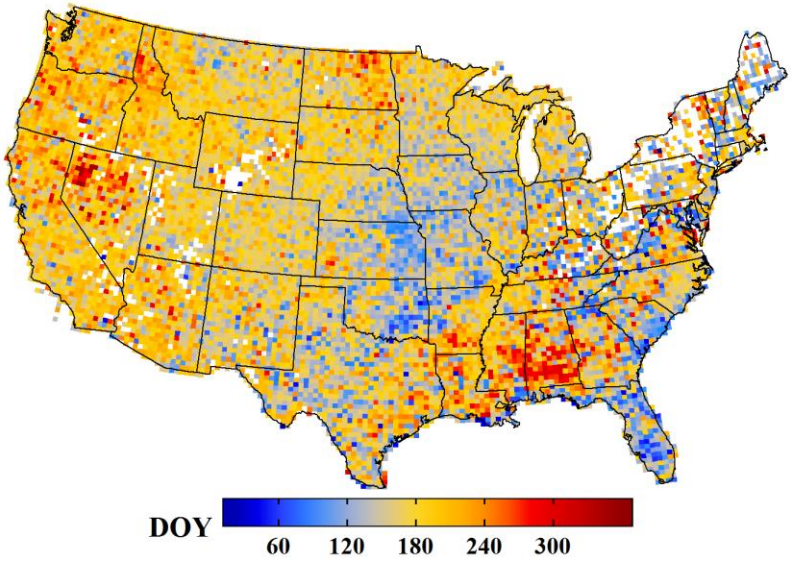

Figure 3-11. Four-year mean seasonal peak time (day of year (DOY)) of the PM2.5 emissions at a 0.25°×0.3125° grid.

The peak time of seasonal PM2.5 emissions shows strong variations across the CONUS (Figure 3-11). In the Western CONUS, the emissions mainly reach peaks during July-September although the peak appears through winter and early spring months in a very small portion of areas. In the central CONUS, there are two main peak time periods: March to April in the middle central states (Kansas, Oklahoma, Missouri, Iowa, and Nebraska states), and July to September in other states. The peak time periods in the eastern CONUS are complex. Emissions reach the peak during the period from January to early April in most areas in Florida, August and September in the Mississippi river valley, and winter months in the south Mississippi and south Alabama.

3.3.5. Evaluation of Biomass-Burning Emissions Estimated from GOES-MODIS FRE

Total biomass consumption estimates calculated from the GOES-MODIS FRE (BC_{FRE}) are comparable with those estimated from 30m Landsat burned areas and FCCS fuel loadings ($BC_{Landsat}$) (Figure 3-12). BC_{FRE} in the 60 selected fire events, which ranges from 0.05 - 3.5 Tg, is significantly correlated to $BC_{Landsat}$ (R^2=0.84, p<0.001) that ranges from 0.02 - 4.8 Tg. BC_{FRE} is relatively underestimated over large fires but overestimated in some small fires compared to $BC_{Landsat}$. Overall, BC_{FRE} is 29% less than $BC_{Landsat}$.

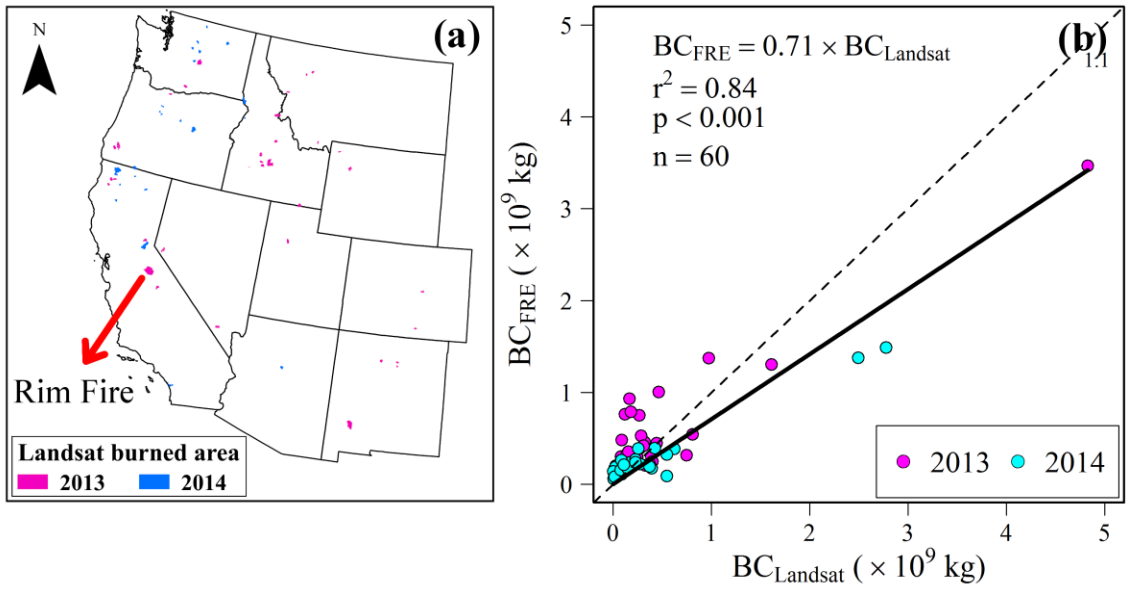

Figure 3-12. Comparison between the GOES-MODIS-FRE based total biomass consumption (BC_{FRE}) and the Landsat-burned-area-based total biomass consumption ($BC_{Landsat}$) across the Western CONUS. (a) Distribution of the 60 selected fire events from 2013 to 2014. (b) Scatterplot of BC_{FRE} against $BC_{Landsat}$.

The monthly GOES-MODIS PM2.5 reveals seasonal similarity and discrepancy with six global emission inventories (Figure 3-13). The overall similarity is found that the emissions generally increase from January, reach the first peak in March or April, decrease in May, but climb up again rapidly and reach the second peak in August, and

then decrease until the end of a year. However, differences are remarkable in an individual year among inventories. For instance, the highest peak in FEERv1.0g1.2 PM2.5 occurred in April in 2011 and 2014, which contrasts sharply with the GOES-MODIS PM2.5 and all other inventories. Moreover, FINNv1.5 PM2.5 does not show distinctive fire season as other inventories, especially in 2011, 2013, and 2014. Overall, the seasonal pattern in the GOES-MODIS PM2.5 estimates matches the best with FLAMBE.

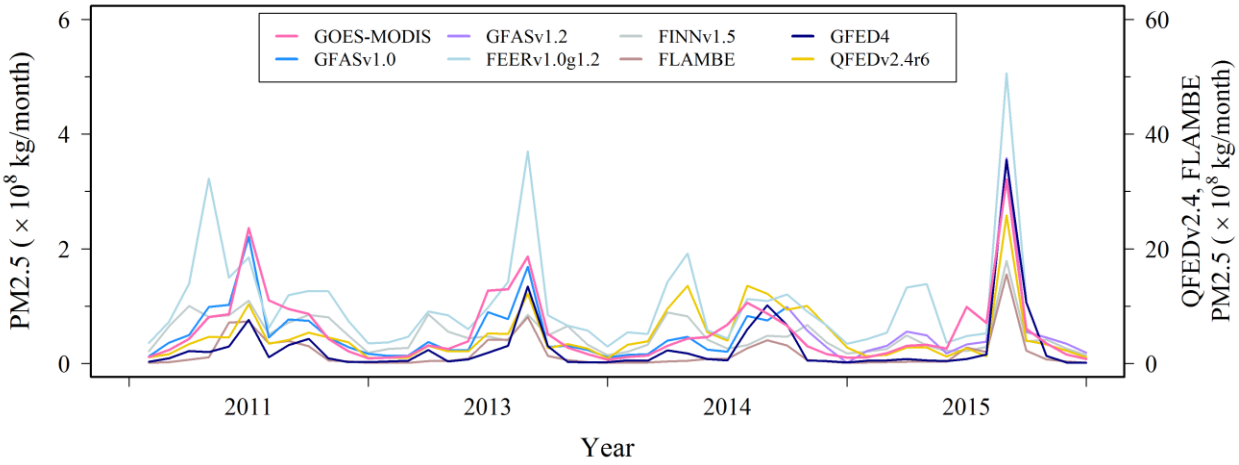

Figure 3-13. Comparison of the monthly total GOES-MODIS PM2.5 emissions with other six inventories across the CONUS in four years of 2011, 2013, 2014, and 2015. The right y-axis represents QFEDv2.4v6 and FLAMBE.

The mean monthly PM2.5 emissions varied largely among various BBE datasets (Table 3-4). The GOES-MODIS PM2.5 is similar to GFAS1.x and FINNv1.5 with a difference less than 12%. The GFED4 are the smallest among all BBE data sets, but comparable with the GOES-MODIS PM2.5 from October to following February (Figure 3-13). In contrast, the FEERv1.0g1.2, FLAMBE, and QFEDv2.4r6 are approximately

1.7, 3.2, and 8.4 times of the GOES-MODIS PM2.5, respectively. Moreover, compared to two annual inventories of WFEISv0.5 and NEI, the annual GOES-MODIS PM2.5 is approximately 11% larger than WFEISv0.5 in 2011 and 2013, but 54% smaller than NEI in 2011 and 2014.

Table 3-4. The mean monthly PM2.5 emissions (Gg) of the GOES-MODIS and six inventories

GOES-MODIS	GFED4	FINNv1.5	GFASv1.x	FEERv1.0g1.2	FLAMBE	QFEDv2.4
57.6	28.2	50.5	55.3	100.2	181.6	485.6

The hourly CO estimates from the GOES-MODIS and the WRF-Chem model show overall similar temporal patterns although their magnitude values differ in two periods in the 2013 Rim Fire, California (Figure 3-14). During 21-27 August (excluding eight hours within two gray dash lines in Figure 3-14) when the WRF-Chem model was constrained only by ground-based observations, the GOES-MODIS CO on hourly average is 47% and 237% of the model-simulated CO during the daytime (14:00-24:00 UTC) and nighttime (1:00-13:00 UTC), respectively. On a daily average, the GOES-MODIS CO is 30% smaller than the model-simulated CO. However, during the eight hours from 18:00 UTC (26 August) to 02:00 UTC (27 August) when the WRF-Chem model was constrained by both the airborne-based and ground-based observations, the GOES-MODIS CO is almost the same as the model-simulated CO. Their difference is less than 13% on an hourly average.

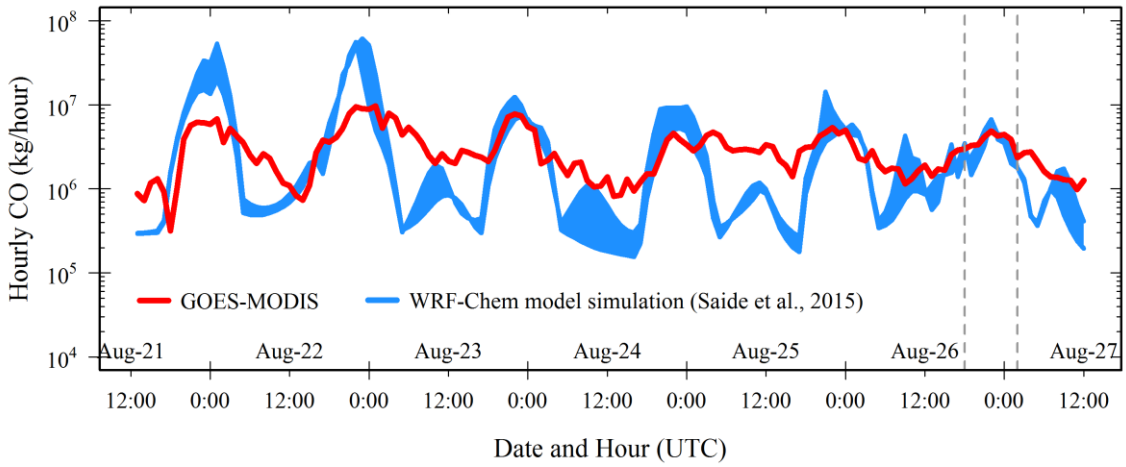

Figure 3-14. Comparison of hourly CO emissions in the Rim Fire. The red line is the GOES-MODIS CO estimates, and the light blue area represents the estimates simulated by the WRF-Chem model. CO simulation from WRF-Chem model was performed using both ground- and airborne-based observations during the time period within two gray dash lines (18:00 UTC on 26 to 02:00 UTC on 27 August) while only the ground observations during the rest time period.

3.4. Discussion

Satellite-based FRP offers a potential tool for improving the accuracy of BBE estimates in near real time, which elevates the application capability of BBE in modeling air quality, and environmental and metrological conditions (Kaufman et al., 1998; Roberts and Wooster, 2008; Wooster, 2002; Wooster et al., 2005; Zhang et al., 2012). High-quality BBE could be calculated from diurnal FRP variations if FRP observations are available at a high spatiotemporal resolution. However, the existing solutions of FRP from either MODIS or geostationary satellites alone hardly produce BBE that satisfies models for forecasting air quality and environmental changes (Andela et al., 2015). By fusing the high temporal GOES FRP with high spatial MODIS FRP observations, this

study reconstructed diurnal FRP cycles every 15 min to estimate hourly BBE at a 0.25°×0.3125° grid across the CONUS from 2011 to 2015.

This study indicates the importance of diurnal FRP cycles in the estimation of BBE. MODIS FRP has been commonly used to calculate daily mean FRP flux and thereafter estimate daily FRE and BBE (Darmenov and Silva, 2015; Kaiser et al., 2012), or directly related to BBE estimates (Ichoku and Ellison, 2014; Ichoku and Kaufman, 2005) by assuming that MODIS observations can capture the structure of diurnal fire activities. Comparisons of 4-time MODIS FRP during a day with 15-min GOES FRP show that MODIS observations frequently fail to capture both peaks and troughs in diurnal FRP cycles even in very large forest fires over the Western CONUS (Figure 3-3 and Figure 3-4a,b). Similar situations were also identified in the shrubland fires in Portugal and savanna fires in Africa by comparing MODIS FRP and 15-min FRP from SEVIRI (Spinning Enhanced Visible and InfraRed Imager) (Andela et al., 2015). Although the MODIS diurnal FRP cycle could be established by assuming that FRP follows a Gaussian-shaped diurnal model (Andela et al., 2015; Ellicott et al., 2009; Konovalov et al., 2014; Vermote et al., 2009), this study demonstrates that the diurnal FRP cycle varies with ecosystems rather than presenting a simple uniform shape (Figure 3-4). As a result, high uncertainties in characterizing diurnal variations in MODIS FRP result in the low quality in estimating FRE and BBE.

This study also reveals the difference in spatiotemporal patterns of emissions from wildfires and agriculture burnings across the CONUS. The major sources of wildfires emissions vary spatially in the Western CONUS interannually (Figure 3-7). In California, for example, the annual PM2.5 has increased by approximately 300% from

2011 - 2011(Figure 3-8), which is most likely related to the exceptional drought underwent in the same periods (Asner et al., 2016; Griffin and Anchukaitis, 2014; Robeson, 2015). The big drought occurred in 2011 in the southWestern CONUS (Texas, Arizona, and New Mexico) elevated PM2.5 emissions by 487% that accounted for 30.8% (201Gg) of the annual PM2.5 in the CONUS (Figure 8) (Nielsen-Gammon, 2011). In contrast, the agriculture burnings (the Mississippi River Valley and the Florida Everglades) burn annually (Figure 3-7) with very small inter-annual variation in PM2.5 emissions (Figure 3-8), which is similar to the small interannual variation in cropland burned areas across the CONUS (McCarty et al., 2009; Randerson et al., 2012; Zhang and Kondragunta, 2008). Moreover, the average diurnal variation of PM2.5 demonstrates that the major emissions from agriculture burning mainly released from 9:00 to 18:00 local solar time (Figure 5a and Figure 10c), which is most likely related to timings of agriculture burning practices (Brenner and Wade, 2003; Kim Oanh et al., 2011; McRae et al., 1994). However, wildfires can burn during nighttime and contribute a significant portion of emissions compared to daytime emissions (Figure 3-5c and Figure 3-10b).

The GOES-MODIS BBE estimates and the Landsat based BBE estimates are overall comparable, although the GOES-MODIS BBE is relatively larger than the Landsat based estimates in some small fires but smaller in large fires. These difference may be attributed to two possible reasons: (a) the assumed consistent burning period for temporal gaps (section 2.5.2) is longer than the real burning period for small fire events; and (b) long-time period obscuration of clouds or thick smokes in some large fires likely cause the underestimation of FRE (e.g., fire-storms in the Rim fire (Peterson et al., 2015)). Nevertheless, for the largest fire event, Rim fire in California, both the GOES-

MODIS based biomass consumption (3.5 Tg) and the Landsat based estimate (4.8 Tg) are similar to the Lidar-and-Landsat based estimates of biomass consumption (3.93 - 6.58 Tg) in (Garcia et al., 2017).

Although comparisons show similarities and discrepancies among BBE inventories, the novelty of algorithm developed in this study is to calculate the GOES-MODIS emissions by improving diurnal FRP and FRE quantification while most other methods focus on tuning the coefficients or scaling factors to convert FRP to fire emissions. Generally, the emissions from QFEDv2.4r6 and FEERv1.0g1.2 are larger than the conventional-method-based emissions estimates by a factor of 2-8, which has also been found in regional (Zhang et al., 2014) to global emissions estimates (Ichoku and Ellison, 2014; Kaiser et al., 2012; Zhang et al., 2012). It is likely due to the fact that both the QFED and FEER use large coefficients (converting FRP to emissions) that are adjusted using AOD observations for atmospheric models (Darmenov and Silva, 2015; Ichoku and Ellison, 2014). Moreover, the seasonal FEER emissions produce unreasonable peaks during spring months in 2011 and 2014 (Figure 3-13), which is associated with relatively low-quality control and moderate confidence of the FEER emissions coefficients (Ichoku and Ellison, 2014). Though the GOES-MODIS PM2.5 emissions quantitatively compare well with GFASv1.x (Table 3-4), the mean annual total FRE of GOES-MODIS is 141% of FRE estimated from GFASv1.x (this result did not show here). This discrepancy in FRE is most likely offset by the much larger biomass combustion factors used in GFASv1.x. The GOES-MODIS PM2.5 is also numerically similar to FINNv1.5 (Table 3-4) but FINNv1.5 emissions estimates are highly uncertain due to several uncertainty sources, especially the burned area that is simply estimated

from MODIS active fire counts (Wiedinmyer et al., 2011). Among all conventional-method-based inventories, the FLAMBE is larger by a factor of 2-4 than the other inventories (Table 3-4), which is similar to the previous finding obtained by comparing FLAMBE with GFED across the CONUS (Reid et al., 2009). The FLAMBE emission estimates could be overestimated in large fires in the Western CONUS because large fires (or fire clusters) greatly boost up FLAMBE emissions in Northern Africa (Zhang et al., 2014). Nevertheless, the seasonal variation of the GOES-MODIS matches the best with FLAMBE (Figure 3-13), which is likely attributed to the use of GOES WF_ABBA data in both approaches. In contrast, GFED4 is the smallest (less by a factor of 1-4 than the other inventories), which could be related to the underestimates of MODIS burned areas. The EPA NEI is larger than all other conventional-method-based inventories (except FLAMBE) by a factor of 2-3, which may suggest that the ground-based observations include many more fires than satellites detected fires (Short, 2015). However, the NEI only produces annual emissions calculated from fuel loadings and burned area reported from federal, state, and local agencies, which is lack of validations. To sum up, the differences in either models of emissions estimation or the methods of parameterization can result in significant discrepancy among inventories.

The 15-min diurnal FRP cycles reconstructed from the fused GOES and MODIS FRP have several advantages. First, FRP in small fires (10-30 MW) that are missed by GOES (Roberts and Wooster, 2008; Xu et al., 2010) are compensated by calibrating GOES FRP against MODIS FRP. Second, the reconstructed diurnal FRP cycles partially mitigate the underestimation of FRE due to omission errors in FRP retrievals from GOES and MODIS because of dynamic transitions of combustion phases and obscurations of

clouds. During transitions of combustion phase, a fire is detectable from GOES or MODIS when it burns intensely in favorable conditions while it is omitted when it is cooling down and smoldering (Giglio et al., 2003; Wooster et al., 2003). Third, the reconstructed diurnal FRP cycles represent well diurnal variations of fires in most ecosystems. This was demonstrated by the good agreement of hourly CO emissions between the GOES-MODIS estimates and the WRF-Chem model simulation in the Rim Fire. It is particularly true compared to the WRF-Chem simulation that is constrained by both ground- and airborne-based measurements during 26 - 27 August 2013 (Figure 3-14).

The fused FRP from MODIS and GOES retrievals and the reconstructed diurnal FRP cycles evidently enhance the capability of BBE estimates in near real-time; however, some uncertainties could still remain as the data processing is mostly empirical. However, the algorithm developed in this study is expected to reconstruct more accurate diurnal FRP cycles and improve BEE estimates by fusing FRP from new polar-orbiting and geostationary satellites in future. The Visible Infrared Imaging Radiometer Suite (VIIRS) onboard the Suomi National Polar-Orbiting Partnership (NPP) satellite is producing FRP at a spatial resolution of 750 m (at nadir), which can capture much smaller fires than MODIS does (Csiszar et al., 2014). On the other hand, the Advanced Baseline Imager (ABI) onboard GOES-R is to retrieve FRP at a spatial resolution of 2 km (at nadir) every 5 min (Schmidt et al., 2012), which is significantly improved relative to FRP from current GOES Imager.

3.5. Conclusions

We reconstructed ecosystem-specific diurnal FRP cycles by fusing high temporal resolution GOES FRP with high spatial resolution MODIS FRP to estimate BBE across the CONUS. The reliable diurnal FRP cycles are essential to accurately calculate FRE that plays a key role in BBE estimation. It is due to the fact that the estimation of BBE using limited daily observations of polar-orbiting satellites raises considerable uncertainties. The hourly GOES-MODIS BBE can be effectively estimated from diurnal FRP cycles in a 0.25°×0.3125° grid, which could provide reliable inputs for modeling and forecasting air quality in near real time. The GOES-MODIS BBE is comparable with the estimates using burned areas and fuel loadings in Landsat burned areas, and hourly emissions simulated using the WRF-Chem model with an overall uncertainty less than 30%. The seasonal variation in GOES-MODIS BBE also shows good agreement with existing inventories, and the magnitude values are reasonable compared to existing inventories (difference <12% with two products).

It is recommended to apply the algorithm developed in this study to fuse FRP retrievals from VIIRS and GOES-R ABI. In this way, the diurnal FRP cycle with much higher temporal and spatial resolutions could be reconstructed and the BBE estimates could be greatly improved.

Acknowledgments

The authors thank Dr. Pablo E. Saide for sharing the WRF-Chem model simulated CO emissions in California Rim fire, and Dr. Edward J. Hyer and Dr. Luke T. Ellison for providing and discussing in uses of FLAMBE and FEER emissions inventories. The

authors also want to thank all groups who contribute and make emissions inventories in Table 3-3 available to the public. The manuscript contents are solely the opinions of the author(s) and do not constitute a statement of policy, decision, or position on behalf of NOAA or the U. S. Government. MODIS active fire data is available from NASA Level-1 and Atmosphere Archive & Distribution System (LAADS) (https://ladsweb.modaps.eosdis.nasa.gov/), and the WF_ABBA GOES active fire data is available at NOAA (http://satepsanone.nesdis. noaa.gov/pub/FIRE/forPo/).

References

Akagi, S. K., R. J. Yokelson, C. Wiedinmyer, M. J. Alvarado, J. S. Reid, T. Karl, J. D. Crounse, and P. O. Wennberg (2011), Emission factors for open and domestic biomass burning for use in atmospheric models, *Atmos. Chem. Phys.*, *11*(9), 4039-4072, doi: https://doi.org/10.5194/acp-11-4039-2011.

Akimoto, H. (2003), Global Air Quality and Pollution, *Science*, *302*(5651), 1716-1719, doi: https://doi.org/10.1126/science.1092666.

Andela, N., J. W. Kaiser, G. R. van der Werf, and M. J. Wooster (2015), New fire diurnal cycle characterizations to improve fire radiative energy assessments made from MODIS observations, *Atmos. Chem. Phys.*, *15*(15), 8831-8846, doi: https://doi.org/10.5194/acp-15-8831-2015.

Andreae, M. O., and P. Merlet (2001), Emission of trace gases and aerosols from biomass burning, *Global Biogeochemical Cycles*, *15*(4), 955-966, doi: https://doi.org/10.1029/2000GB001382.

Asner, G. P., P. G. Brodrick, C. B. Anderson, N. Vaughn, D. E. Knapp, and R. E. Martin (2016), Progressive forest canopy water loss during the 2012–2015 California drought, *Proceedings of the National Academy of Sciences*, *113*(2), E249-E255, doi: https://doi.org/10.1073/pnas.1523397113.

Baucum, L., R. Rice, and T. Schueneman (2002), An overview of Florida sugarcane, *Agronomy Department, Florida Cooperative Extension Service, Institute of Food and Agricultural Sciences, University of Florida. Publication# SS-AGR-232*.

Bey, I., D. J. Jacob, R. M. Yantosca, J. A. Logan, B. D. Field, A. M. Fiore, Q. Li, H. Y. Liu, L. J. Mickley, and M. G. Schultz (2001), Global modeling of tropospheric chemistry with assimilated meteorology: Model description and evaluation, *Journal of Geophysical Research: Atmospheres*, *106*(D19), 23073-23095, doi: https://doi.org/10.1029/2001JD000807.

Boden, T. A., G. Marland, and R. J. Andres (2017), Global, Regional, and National Fossil-Fuel CO2 Emissions, edited by O. R. N. L. Carbon Dioxide Information Analysis Center, U.S. Department of Energy, Oak Ridge, Tenn., U.S.A., doi: https://doi.org/10.3334/CDIAC/00001_V2017.

Bond, T. C., et al. (2013), Bounding the role of black carbon in the climate system: A scientific assessment, *Journal of Geophysical Research: Atmospheres*, *118*(11), 5380-5552, doi: https://doi.org/10.1002/jgrd.50171.

Boschetti, L., and D. P. Roy (2009), Strategies for the fusion of satellite fire radiative power with burned area data for fire radiative energy derivation, Journal of

Geophysical Research: Atmospheres, 114(D20), D20302, doi: https://doi.org/ https://doi.org/10.1029/2008JD011645.

Boschetti, L., H. D. Eva, P. A. Brivio, and J. M. Grégoire (2004), Lessons to be learned from the comparison of three satellite-derived biomass burning products, *Geophysical Research Letters, 31*(21), L21501, doi: https://doi.org/10.1029/2004GL021229.

Bowman, D. M. J. S., et al. (2009), Fire in the Earth System, *Science, 324*(5926), 481-484, doi: https://doi.org/10.1126/science.1163886.

Brenner, Jim; Wade, Dale. 2003. Florida's Revised Prescribed Fire Law: Protection For Responsible Burners. Pages 132-136 in K.E.M. Galley, R.C. Klinger, and N.G. Sugihara (eds.). Proceedings of Fire Conference 2000: The First National Congress on Fire Ecology, Prevention, and Management. Publication No. 13, Tall Timbers Research Station, Tallahassee, FL.

Brown, J. F., T. R. Loveland, D. O. Ohlen, and Z.-L. Zhu (1999), The global land-cover characteristics database: the users' perspective, *Photogrammetric Engineering and Remote Sensing*, *65*(9), 1069-1074.

Burling, I. R., R. J. Yokelson, S. K. Akagi, S. P. Urbanski, C. E. Wold, D. W. T. Griffith, T. J. Johnson, J. Reardon, and D. R. Weise (2011), Airborne and ground-based measurements of the trace gases and particles emitted by prescribed fires in the United States, *Atmos. Chem. Phys.*, 11(23), 12197-12216, doi: https://doi.org/10.5194/acp-11-12197-2011.

Campbell, J., D. Donato, D. Azuma, and B. Law (2007), Pyrogenic carbon emission from a large wildfire in Oregon, United States, *Journal of Geophysical Research: Biogeosciences*, *112*(G4), G04014, doi: https://doi.org/10.1029/2007JG000451.

Chuvieco, E., C. Yue, A. Heil, F. Mouillot, I. Alonso-Canas, M. Padilla, J. M. Pereira, D. Oom, and K. Tansey (2016), A new global burned area product for climate assessment of fire impacts, *Global Ecology and Biogeography*, *25*(5), 619-629, doi: https://doi.org/10.1111/geb.12440.

Crutzen, P. J., and M. O. Andreae (1990), Biomass Burning in the Tropics: Impact on Atmospheric Chemistry and Biogeochemical Cycles, *Science*, *250*(4988), 1669-1678, doi: https://doi.org/10.1126/science.250.4988.1669.

Csiszar, I., W. Schroeder, L. Giglio, E. Ellicott, K. P. Vadrevu, C. O. Justice, and B. Wind (2014), Active fires from the Suomi NPP Visible Infrared Imaging Radiometer Suite: Product status and first evaluation results, *Journal of Geophysical Research: Atmospheres*, 119(2), 2013JD020453, doi: https://doi.org/10.1002/2013JD020453.

Darmenov, A. S., and A. d. Silva (2015), The Quick Fire Emissions Dataset (QFED): Documentation of versions 2.1, 2.2 and 2.4 *Rep. TM–2015–104606,* 212 pp, NASA, Goddard Space Flight Center Greenbelt, MD.

Eastham, S. D., and D. J. Jacob (2017), Limits on the ability of global Eulerian models to resolve intercontinental transport of chemical plumes, *Atmos. Chem. Phys.*, *17*(4), 2543-2553, doi: https://doi.org/10.5194/acp-17-2543-2017.

Eidenshink, J., B. Schwind, K. Brewer, Z. Zhu, B. Quayle, and S. Howard (2007), A project for monitoring trends in burn severity, *Fire Ecology*, *3*(1), 19, doi: https://doi.org/10.4996/fireecology.0301003

Ellicott, E., E. Vermote, L. Giglio, and G. Roberts (2009), Estimating biomass consumed from fire using MODIS FRE, *Geophysical Research Letters*, *36*(13), L13401, doi: https://doi.org/10.1029/2009GL038581.

Freeborn, P. H., M. J. Wooster, W. M. Hao, C. A. Ryan, B. L. Nordgren, S. P. Baker, and C. Ichoku (2008), Relationships between energy release, fuel mass loss, and trace gas and aerosol emissions during laboratory biomass fires, *Journal of Geophysical Research: Atmospheres*, *113*(D1), D01301, doi: https://doi.org/ 10.1029/2007jd008679.

Freeborn, P. H., M. J. Wooster, G. Roberts, B. D. Malamud, and W. Xu (2009), Development of a virtual active fire product for Africa through a synthesis of geostationary and polar orbiting satellite data, *Remote Sensing of Environment*, *113*(8), 1700-1711, doi: https://doi.org/10.1016/j.rse.2009.03.013.

Freeborn, P. H., M. J. Wooster, D. P. Roy, and M. A. Cochrane (2014), Quantification of MODIS fire radiative power (FRP) measurement uncertainty for use in satellite-based active fire characterization and biomass burning estimation, *Geophysical Research Letters*, *41*(6), 2013GL059086, doi: https://doi.org/10.1002/2013GL059086.

French, N. H. F., et al. (2011), Model comparisons for estimating carbon emissions from North American wildland fire, *Journal of Geophysical Research: Biogeosciences*, *116*(G4), G00K05, doi: https://doi.org/10.1029/2010JG001469.

Garcia, M., S. Saatchi, A. Casas, A. Koltunov, S. Ustin, C. Ramirez, J. Garcia-Gutierrez, and H. Balzter (2017), Quantifying biomass consumption and carbon release from the California Rim fire by integrating airborne LiDAR and Landsat OLI data, Journal of Geophysical Research: Biogeosciences, 122(2), 340-353, doi: https://doi.org/10.1002/2015JG003315.

Ghimire, B., C. A. Williams, G. J. Collatz, and M. Vanderhoof (2012), Fire-induced carbon emissions and regrowth uptake in western U.S. forests: Documenting variation across forest types, fire severity, and climate regions, *Journal of Geophysical Research: Biogeosciences*, *117*(G3), G03036, doi: https://doi.org/10.1029/2011JG001935.

Giglio, L. (2007), Characterization of the tropical diurnal fire cycle using VIRS and MODIS observations, Remote Sensing of Environment, 108(4), 407-421, doi: https://doi.org/https://doi.org/10.1016/j.rse.2006.11.018.

Giglio, L. (2015), MODIS Collection 6 Active Fire Product User's Guide, https://cdn.earthdata.nasa.gov/conduit/upload/3865/MODIS_C6_Fire_User_Guide_A.pdf, last accessed on 1/24/2018.

Giglio, L., Boschetti, L., Roy, D.P., Humber, M.L., Justice, C.O., 2018, The Collection 6 MODIS Burned Area Mapping Algorithm and Product, Remote Sensing of Environment. In Review

Giglio, L., J. Descloitres, C. O. Justice, and Y. J. Kaufman (2003), An Enhanced Contextual Fire Detection Algorithm for MODIS, *Remote Sensing of Environment*, *87*(2–3), 273-282, doi: https://doi.org/10.1016/S0034-4257(03)00184-6.

Giglio, L., J. T. Randerson, and G. R. van der Werf (2013), Analysis of daily, monthly, and annual burned area using the fourth-generation global fire emissions database (GFED4), *Journal of Geophysical Research: Biogeosciences*, *118*(1), 317-328, doi: https://doi.org/10.1002/jgrg.20042.

Giglio, L., W. Schroeder, and C. O. Justice (2016), The collection 6 MODIS active fire detection algorithm and fire products, Remote Sensing of Environment, 178, 31-41, doi: https://doi.org/10.1016/j.rse.2016.02.054.

Griffin, D., and K. J. Anchukaitis (2014), How unusual is the 2012–2014 California drought?, *Geophysical Research Letters*, *41*(24), 9017-9023, doi: https://doi.org/10.1002/2014GL062433.

Hao, W. M., M.-H. Liu, and P. J. Crutzen (1990), Estimates of Annual and Regional Releases of CO2 and Other Trace Gases to the Atmosphere from Fires in the Tropics, Based on the FAO Statistics for the Period 1975–1980, in *Fire in the Tropical Biota: Ecosystem Processes and Global Challenges*, edited by J. G. Goldammer, pp. 440-462, Springer Berlin Heidelberg, Berlin, Heidelberg, doi: https://doi.org/10.1007/978-3-642-75395-4_20.

Hudak, A. T., M. B. Dickinson, B. C. Bright, R. L. Kremens, E. L. Loudermilk, J. J. O'Brien, B. S. Hornsby, and R. D. Ottmar (2016), Measurements relating fire radiative energy density and surface fuel consumption – RxCADRE 2011 and 2012, *International Journal of Wildland Fire*, *25*(1), 25-37, doi: https://doi.org/10.1071/WF14159.

Ichoku, C., and L. Ellison (2014), Global top-down smoke-aerosol emissions estimation using satellite fire radiative power measurements, *Atmos. Chem. Phys.*, *14*(13), 6643-6667, doi: https://doi.org/10.5194/acp-14-6643-2014.

Ichoku, C., and Y. J. Kaufman (2005), A method to derive smoke emission rates from MODIS fire radiative energy measurements, *Geoscience and Remote Sensing, IEEE Transactions on*, *43*(11), 2636-2649, doi: https://doi.org/10.1109/TGRS.2005.857328.

Jacobson, M. Z. (2014), Effects of biomass burning on climate, accounting for heat and moisture fluxes, black and brown carbon, and cloud absorption effects, *Journal of Geophysical Research: Atmospheres*, *119*(14), 2014JD021861, doi: https://doi.org/10.1002/2014JD021861.

Johnston, F. H., S. Melody, and D. M. J. S. Bowman (2016), The pyrohealth transition: how combustion emissions have shaped health through human history, *Philosophical Transactions of the Royal Society B: Biological Sciences*, *371*(1696), doi: https://doi.org/10.1098/rstb.2015.0173.

Justice, C. O., L. Giglio, S. Korontzi, J. Owens, J. T. Morisette, D. Roy, J. Descloitres, S. Alleaume, F. Petitcolin, and Y. Kaufman (2002), The MODIS fire products, Remote Sensing of Environment, 83(1–2), 244-262, doi: https://doi.org/https://doi.org/10.1016/S0034-4257(02)00076-7.

Kaiser, J., M. Suttie, J. Flemming, J. Morcrette, O. Boucher, and M. Schultz (2009), Global real-time fire emission estimates based on space-borne fire radiative power observations, paper presented at AIP conference proceedings.

Kaiser, J. W., et al. (2012), Biomass burning emissions estimated with a global fire assimilation system based on observed fire radiative power, *Biogeosciences, 9*(1), 527-554, doi: https://doi.org/10.5194/bg-9-527-2012.

Kasischke, E. S., T. Loboda, L. Giglio, N. H. F. French, E. E. Hoy, B. de Jong, and D. Riano (2011), Quantifying burned area for North American forests: Implications for direct reduction of carbon stocks, *Journal of Geophysical Research: Biogeosciences*, *116*(G4), G04003, doi: https://doi.org/10.1029/2011JG001707.

Kaufman, Y. J., C. O. Justice, L. P. Flynn, J. D. Kendall, E. M. Prins, L. Giglio, D. E. Ward, W. P. Menzel, and A. W. Setzer (1998), Potential global fire monitoring from EOS-MODIS, *Journal of Geophysical Research: Atmospheres*, *103*(D24), 32215-32238, doi: https://doi.org/10.1029/98JD01644.

Kaufman, Y. J., D. Tanre, and O. Boucher (2002), A satellite view of aerosols in the climate system, *Nature*, *419*(6903), 215-223, doi: https://doi.org/10.1038/nature01091.

Keeley, J. E. (2009), Fire intensity, fire severity and burn severity: a brief review and suggested usage, *International Journal of Wildland Fire*, *18*(1), 116-126, doi: https://doi.org/ 10.1071/WF07049.

Kim Oanh, N. T., B. T. Ly, D. Tipayarom, B. R. Manandhar, P. Prapat, C. D. Simpson, and L. J. Sally Liu (2011), Characterization of particulate matter emission from open burning of rice straw, *Atmospheric Environment*, *45*(2), 493-502, doi: https://doi.org/10.1016/j.atmosenv.2010.09.023.

Konovalov, I. B., E. V. Berezin, P. Ciais, G. Broquet, M. Beekmann, J. Hadji-Lazaro, C. Clerbaux, M. O. Andreae, J. W. Kaiser, and E. D. Schulze (2014), Constraining CO2 emissions from open biomass burning by satellite observations of co-emitted species: a method and its application to wildfires in Siberia, *Atmos. Chem. Phys.*, *14*(19), 10383-10410, doi: https://doi.org/10.5194/acp-14-10383-2014.

Kremens, R. L., M. B. Dickinson, and A. S. Bova (2012), Radiant flux density, energy density and fuel consumption in mixed-oak forest surface fires, *International Journal of Wildland Fire*, *21*(6), 722-730, doi: https://doi.org/10.1071/WF10143.

Kumar, S. S., D. P. Roy, L. Boschetti, and R. Kremens (2011), Exploiting the power law distribution properties of satellite fire radiative power retrievals: A method to estimate fire radiative energy and biomass burned from sparse satellite observations, Journal of Geophysical Research: Atmospheres, 116(D19), D19303, doi: https://doi.org/ https://doi.org/10.1029/2011JD015676.

Lelieveld, J., J. S. Evans, M. Fnais, D. Giannadaki, and A. Pozzer (2015), The contribution of outdoor air pollution sources to premature mortality on a global scale, *Nature*, *525*(7569), 367-371, doi: https://doi.org/10.1038/nature15371.

Li, F., X. Zhang, S. Kondragunta, and I. Csiszar (2018a), Li, F., Comparison of Fire Radiative Power Estimates From VIIRS and MODIS Observations, Journal of Geophysical Research: Atmospheres, 123(9), 4545-4563, doi: https://doi.org/10.1029/2017JD027823.

Li, F., X. Zhang, S. Kondragunta, and D. P. Roy (2018b), Investigation of the Fire Radiative Energy Biomass Combustion Coefficient: A Comparison of Polar and

Geostationary Satellite Retrievals Over the Conterminous United States, Journal of Geophysical Research: Biogeosciences, 123(2), 722-739, doi: https://doi.org/10.1002/2017JG004279.

Littell, J. S., D. L. Peterson, K. L. Riley, Y. Liu, and C. H. Luce (2016), A review of the relationships between drought and forest fire in the United States, *Global Change Biology*, 22(7), 2353-2369, doi: https://doi.org/10.1111/gcb.13275.

Lu, S., Wang, J., Bhattacharjee, P., Zhang, X., Kondragunta, S., da Silva, A., McQueen, J., Moorthi, S., Hou, Y., Tallapragada, V., Harris, A., and Koner, P., 2016. The Implementation of NEMS GFS Aerosol Component (NGAC) Version 2: Global Aerosol Forecasting at NCEP Using Satellite-Based Smoke Emissions, *Joint Center for Satellite Data Assimilation Quarterly*, 53, 5-8, doi: https://doi.org/10.7289/V50C4SS7.

Malamud, B. D., J. D. A. Millington, and G. L. W. Perry (2005), Characterizing wildfire regimes in the United States, *Proceedings of the National Academy of Sciences of the United States of America*, *102*(13), 4694-4699, doi: https://doi.org/10.1073/pnas.0500880102.

McCarty, J. L., S. Korontzi, C. O. Justice, and T. Loboda (2009), The spatial and temporal distribution of crop residue burning in the contiguous United States, *Science of The Total Environment*, *407*(21), 5701-5712, doi: https://doi.org/10.1016/j.scitotenv.2009.07.009.

McRae, D. J., T. J. Lynham, and R. J. Frech (1994), Understory prescribed burning in red pine and white pine, *The Forestry Chronicle, 70*(4), 395-401, doi: https://doi.org/10.5558/tfc70395-4.

Mota, B., and M. J. Wooster (2018), A new top-down approach for directly estimating biomass burning emissions and fuel consumption rates and totals from geostationary satellite fire radiative power (FRP), Remote Sensing of Environment, 206, 45-62, doi: https://doi.org/10.1016/j.rse.2017.12.016.

Mouillot, F., M. G. Schultz, C. Yue, P. Cadule, K. Tansey, P. Ciais, and E. Chuvieco (2014), Ten years of global burned area products from spaceborne remote sensing—A review: Analysis of user needs and recommendations for future developments, *International Journal of Applied Earth Observation and Geoinformation*, *26*, 64-79, doi: https://doi.org/10.1016/j.jag.2013.05.014.

Nielsen-Gammon, J. W., 2011: The 2011 Texas Drought: A Briefing Packet for the Texas Legislature. 43 pp. http://climatexas.tamu.edu/files/2011_drought.pdf, last accessed on 4/11/2017.

Ottmar, R. D., S. J. Prichard, R. E. Vihnanek, and D. V. Sandberg (2006), Modification and Validation of Fuel Consumption Models for Shrub and Forested lands in the Southwest, Pacific Northwest, Rockies, Midwest, Southeast and Alaska, Seattle Washington, https://www.firescience.gov/projects/98-1-9-06/project/98-1-9-06_final_report.pdf, last accessed on 4/11/2017.

Pausas, J. G., and E. Ribeiro (2013), The global fire–productivity relationship, *Global Ecology and Biogeography*, 22(6), 728-736, doi: https://doi.org/10.1111/geb.12043.

Peterson, D. A., E. J. Hyer, J. R. Campbell, M. D. Fromm, J. W. Hair, C. F. Butler, and M. A. Fenn (2015), The 2013 Rim Fire: Implications for Predicting Extreme Fire Spread, Pyroconvection, and Smoke Emissions, Bulletin of the American Meteorological Society, 96(2), 229-247, doi: https://doi.org/10.1175/bams-d-14-00060.1.

Peterson, D., J. Wang, C. Ichoku, E. Hyer, and V. Ambrosia (2013), A sub-pixel-based calculation of fire radiative power from MODIS observations: 1: Algorithm development and initial assessment, *Remote Sensing of Environment*, *129*(0), 262-279, doi: https://doi.org/10.1016/j.rse.2012.10.036.

Randerson, J. T., Y. Chen, G. R. van der Werf, B. M. Rogers, and D. C. Morton (2012), Global burned area and biomass burning emissions from small fires, *Journal of Geophysical Research: Biogeosciences*, *117*(G4), G04012, doi: https://doi.org/10.1029/2012JG002128.

Reid, J. S., et al. (2009), Global Monitoring and Forecasting of Biomass-Burning Smoke: Description of and Lessons From the Fire Locating and Modeling of Burning Emissions (FLAMBE) Program, *Selected Topics in Applied Earth Observations and Remote Sensing, IEEE Journal of*, *2*(3), 144-162, doi: https://doi.org/10.1109/JSTARS.2009.2027443.

Roberts, G., M. J. Wooster, and E. Lagoudakis (2009), Annual and diurnal african biomass burning temporal dynamics, *Biogeosciences*, *6*(5), 849-866, doi: https://doi.org/10.5194/bg-6-849-2009.

Roberts, G. J., and M. J. Wooster (2008), Fire Detection and Fire Characterization Over Africa Using Meteosat SEVIRI, *Geoscience and Remote Sensing, IEEE Transactions on*, *46*(4), 1200-1218, doi: https://doi.org/10.1109/TGRS.2008.915751.

Robeson, S. M. (2015), Revisiting the recent California drought as an extreme value, *Geophysical Research Letters*, *42*(16), 6771-6779, doi: https://doi.org/10.1002/2015GL064593.

Saide, P. E., et al. (2015), Revealing important nocturnal and day-to-day variations in fire smoke emissions through a multiplatform inversion, *Geophysical Research Letters*, *42*(9), 2015GL063737, doi: https://doi.org/10.1002/2015GL063737.

Schmidt, C. C., and E. M. Prins (2003), GOES wildfire ABBA applications in the western hemisphere, paper presented at 2nd International Wildland Fire Ecology and Fire Management Congress and 5th Symp. on Fire and Forest Meteorology, Citeseer.

Schroeder, W., I. Csiszar, L. Giglio, and C. C. Schmidt (2010), On the use of fire radiative power, area, and temperature estimates to characterize biomass burning via moderate to coarse spatial resolution remote sensing data in the Brazilian Amazon, *Journal of Geophysical Research: Atmospheres*, 115(D21), D21121, doi: https://doi.org/10.1029/2009JD013769.

Seiler, W., and P. Crutzen (1980), Estimates of gross and net fluxes of carbon between the biosphere and the atmosphere from biomass burning, *Climatic Change*, *2*(3), 207-247, doi: https://doi.org/10.1007/BF00137988.

Short, K. C. (2015), Sources and implications of bias and uncertainty in a century of US wildfire activity data, *International Journal of Wildland Fire*, 24(7), 883-891, doi: https://doi.org/10.1071/WF14190.

Toon, O. B., et al. (2016), Planning, implementation, and scientific goals of the Studies of Emissions and Atmospheric Composition, Clouds and Climate Coupling by Regional Surveys (SEAC4RS) field mission, *Journal of Geophysical Research: Atmospheres*, 121(9), 2015JD024297, doi: https://doi.org/10.1002/2015JD024297.

Tosca, M. G., J. T. Randerson, and C. S. Zender (2013), Global impact of smoke aerosols from landscape fires on climate and the Hadley circulation, *Atmos. Chem. Phys.*, *13*(10), 5227-5241, doi: https://doi.org/10.5194/acp-13-5227-2013.

van der Werf, G. R., J. T. Randerson, L. Giglio, T. T. van Leeuwen, Y. Chen, B. M. Rogers, M. Mu, M. J. E. van Marle, D. C. Morton, G. J. Collatz, R. J. Yokelson, and P. S. Kasibhatla (2017), Global fire emissions estimates during 1997–2016, Earth Syst. Sci. Data, 9(2), 697-720, doi: https://doi.org/10.5194/essd-9-697-2017.

Venables, W. N., and B. D. Ripley (2002), Modern applied statistics with S, Fourth ed., Springer Science & Business Media.

Vermote, E., E. Ellicott, O. Dubovik, T. Lapyonok, M. Chin, L. Giglio, and G. J. Roberts (2009), An approach to estimate global biomass burning emissions of organic and black carbon from MODIS fire radiative power, *Journal of Geophysical Research: Atmospheres*, *114*(D18), D18205, doi: https://doi.org/10.1029/2008JD011188.

Wiedinmyer, C., S. K. Akagi, R. J. Yokelson, L. K. Emmons, J. A. Al-Saadi, J. J. Orlando, and A. J. Soja (2011), The Fire INventory from NCAR (FINN): a high

resolution global model to estimate the emissions from open burning, *Geosci. Model Dev.*, *4*(3), 625-641, doi: https://doi.org/10.5194/gmd-4-625-2011.

Wolfe, R. E., M. Nishihama, A. J. Fleig, J. A. Kuyper, D. P. Roy, J. C. Storey, and F. S. Patt (2002), Achieving sub-pixel geolocation accuracy in support of MODIS land science, *Remote Sensing of Environment*, *83*(1–2), 31-49, doi: https://doi.org/10.1016/S0034-4257(02)00085-8.

Wolfe, R. E., D. P. Roy, and E. Vermote (1998), MODIS land data storage, gridding, and compositing methodology: Level 2 grid, *Geoscience and Remote Sensing, IEEE Transactions on*, *36*(4), 1324-1338, doi: https://doi.org/10.1109/36.701082.

Wooster, M. J. (2002), Small-scale experimental testing of fire radiative energy for quantifying mass combusted in natural vegetation fires, *Geophysical Research Letters*, *29*(21), 2027, doi: https://doi.org/10.1029/2002GL015487.

Wooster, M. J., G. Roberts, G. L. W. Perry, and Y. J. Kaufman (2005), Retrieval of biomass combustion rates and totals from fire radiative power observations: FRP derivation and calibration relationships between biomass consumption and fire radiative energy release, *Journal of Geophysical Research: Atmospheres*, *110*(D24), D24311, doi: https://doi.org/10.1029/2005jd006318.

Xu, W., M. J. Wooster, G. Roberts, and P. Freeborn (2010), New GOES imager algorithms for cloud and active fire detection and fire radiative power assessment across North, South and Central America, *Remote Sensing of Environment*, *114*(9), 1876-1895, doi: https://doi.org/10.1016/j.rse.2010.03.012.

Zhang, F., J. Wang, C. Ichoku, E. J. Hyer, Z. Yang, C. Ge, S. Su, X. Zhang, S. Kondragunta, and J. W. Kaiser (2014), Sensitivity of mesoscale modeling of smoke direct radiative effect to the emission inventory: a case study in northern sub-Saharan African region, *Environmental Research Letters*, 9(7), 075002, doi: https://doi.org/10.1088/1748-9326/9/7/075002.

Zhang, X., S. Kondragunta, J. Ram, C. Schmidt, and H.-C. Huang (2012), Near-real-time global biomass burning emissions product from geostationary satellite constellation, *Journal of Geophysical Research: Atmospheres*, *117*, D14201, doi: https://doi.org/10.1029/2012jd017459.

Zhang, X., and S. Kondragunta (2008), Temporal and spatial variability in biomass burned areas across the USA derived from the GOES fire product, *Remote Sensing of Environment*, 112(6), 2886-2897, doi: https://doi.org/10.1016/j.rse.2008.02.006.

Zhang, X., S. Kondragunta, C. Schmidt, and F. Kogan (2008), Near real time monitoring of biomass burning particulate emissions (PM2.5) across contiguous United States using multiple satellite instruments, *Atmospheric Environment*, *42*(29), 6959-6972, doi: https://doi.org/ 10.1016/j.atmosenv.2008.04.060.

CHAPTER 4: Comparison of Fire Radiative Power Estimates from VIIRS and MODIS Observations

Li, F., X. Zhang, S. Kondragunta, and I. Csiszar (2018), Comparison of Fire Radiative Power Estimates From VIIRS and MODIS Observations, Journal of Geophysical Research: Atmospheres, 123(9), 4545-4563, doi:10.1029/2017JD027823.

This chapter address Hypothesis #3: *The 750-m VIIRS sensor has better capability of characterizing fires than the 1-km MODIS sensor*.

Abstract

Satellite-based active fire data are a viable tool to understand the role of global fires in the biosphere and atmosphere. The Moderate Resolution Imaging Spectroradiometer (MODIS) sensors on Aqua and Terra satellites are nearing the end of their lives. The Visible Infrared Imaging Radiometer Suite (VIIRS) sensor on the Suomi National Polar-orbiting Partnership (Suomi NPP) satellite and the subsequent Joint Polar Satellite System (JPSS) series is expected to extend the MODIS active fire record. Thus, understanding the similarities of and discrepancies between the two datasets during their overlap period is important for existing applications. This study investigated the dependence of the MODIS and VIIRS fire characterization capabilities on satellite view zenith angle (VZA) and the relationship between the two sensors' fire radiative power (FRP) from individual fire clusters to fire data on continental and global scales. The results indicate that the VIIRS fire characterization capability is similar across swath, whereas MODIS is strongly dependent on VZA. Statistical analyses reveal that the VIIRS and MODIS FRP relationship varies between different spatial scales. In fire clusters, MODIS and VIIRS FRP estimates are very comparable, except for large boreal forest fires where VIIRS FRP is approximately 47% smaller. At the continental scale, the contemporaneous FRP retrievals from MODIS and VIIRS are generally comparable and strongly correlated, but VIIRS FRP is slightly larger and their differences vary across seasons. At global 1°×1° grids, the FRP difference between the two sensors is, on average, approximately 20% in fire-prone regions but varies significantly in fire-limited regions.

4.1. Introduction

Satellite-detected active fire data have been widely used to study regional and global wildfire activity and its impacts on air quality and environmental changes during the last few decades (Flannigan and Haar, 1986; Giglio et al., 2006; Giglio et al., 2003; Prins and Menzel, 1992; Roberts and Wooster, 2008; Schroeder et al., 2014; Csiszar et al., 2014). One of the most important variables for characterizing wildfires is fire radiative power (FRP). This variable is retrieved from the radiance at the 4-μm band of satellite sensors and represents the instantaneous radiative energy that is released from actively burning fires. FRP has been extensively used as a proxy of fire intensity to characterize fire types (Roy and Kumar, 2017; Wooster and Zhang, 2004), fire behaviors (Smith and Wooster, 2005), and fire regimes (Archibald et al., 2013), to predict fire danger (Freeborn et al., 2016), and to investigate interactions among biomass burning, land cover dynamics and hydrological cycles (Ichoku et al., 2016). More importantly, FRP is related to the rate of biomass combustion (Kaufman et al., 1998; Wooster et al., 2003) and the rate of emissions (Ichoku and Kaufman, 2005), which have been subsequently applied to estimate trace gas and aerosol emissions (Kaiser et al., 2012; Kumar et al., 2011; Vermote et al., 2009; Zhang et al., 2012).

FRP retrievals are available from multiple polar-orbiting and geostationary satellites. The Moderate Resolution Imaging Spectroradiometer (MODIS) instrument onboard NASA's Earth Observing System (EOS) Aqua and Terra satellites, for example, has operationally detected active fires globally since 2000. The latest MODIS Collection 6 active fire product provides more scientifically reliable fire detections and FRP retrievals (Giglio et al., 2016a). However, Aqua and Terra MODIS sensors are aging and

nearing the end of their lives. Continuity with Aqua MODIS is provided by the new generation moderate-resolution instrument called the Visible Infrared Imaging Radiometer Suite (VIIRS). The first VIIRS sensor is onboard the Suomi National Polar-orbiting Partnership (Suomi NPP) satellite that was launched in 2011, and subsequent operational VIIRS sensors are planned for the series of Joint Polar Satellite System (JPSS) (Goldberg et al., 2013). (Note that the first operational VIIRS is flown on the NOAA-20 satellite, launched in November 2017. Fire data from this sensor are not included in this study.) Both Suomi NPP and Aqua satellites cross the equator at approximately 1:30 AM (descending orbit) and 1:30 PM (ascending orbit) local times. Compared to the 1-km MODIS bands for fire detection, the VIIRS moderate resolution bands (M-bands) have a similar spectral configuration but higher spatial resolution (750 m) (Cao et al., 2014). The higher spatial resolution in VIIRS relative to MODIS theoretically enables the detection of smaller and cooler fires (Csiszar et al., 2014). VIIRS also applies an onboard aggregation scheme to mitigate the increase in ground sampling distance with satellite scan angle, which strongly affects the detection capability of MODIS at off-nadir (Cao et al., 2014; Freeborn et al., 2014; Peterson et al., 2013; Wolfe et al., 2013; Wolfe et al., 2002). To transition global fire observations from the MODIS era to the VIIRS era, it is essential to understand the similarities of and discrepancies between fire characterizations of the 1-km Aqua MODIS and 750-m VIIRS active fire products for application purposes. These comparisons currently exist only for a few sites between MODIS FRP and the early version VIIRS FRP (Oliva and Schroeder, 2015) that was derived based on the MODIS Collection 4 algorithm (Csiszar et al., 2014).

In this study, we compared one year of FRP retrievals from Aqua MODIS and Suomi NPP VIIRS observations globally. The newly operational 750-m VIIRS fire product is produced by NOAA (National Oceanic and Atmospheric Administration) using a modified algorithm of the MODIS Collection 6 (C6) active fire product (Giglio et al., 2016a); it has been available since April 2016 (Csiszar et al., 2016). This NOAA operational 750-m VIIRS active fire product is hereafter referred to simply as the VIIRS fire product. A comparison of the VIIRS product to the MODIS C6 active fire product should greatly improve our understanding of FRP characterizations for applications, such as estimating biomass-burning emissions. To this end, we conducted the following analyses. First, the active fire detection data from VIIRS and MODIS products were preprocessed to correct duplicate detections in adjacent scans due to the bow-tie effect and repeat detections that were observed from adjacent orbits. Then, the dependences of the two sensors' capabilities of detecting and characterizing fires on satellite view zenith angle were investigated. Finally, comparisons between MODIS and VIIRS FRP estimates were conducted at the local fire-cluster level over different ecosystems, at continental/global scale, and across latitudinal variation.

4.2. Data

4.2.1. MODIS Active Fire Data

The MODIS active fire product detects actively burning fires at the overpass times of the Terra and Aqua satellites (Giglio et al., 2016a). The 1-km Level-2 active fire product (abbreviated MOD14 for Terra and MYD14 for Aqua) provides for each fire

pixel the detection time and coordinates (longitude and latitude) and confidence, fire radiative power, brightness temperatures at the 4-μm and 11-μm bands, and satellite view zenith angle (VZA) (Giglio et al., 2016a). The detection confidence is quantified to a range of 0-100% and is further classified into three categories (high, nominal and low) (Giglio et al., 2003). The fire radiative power in the latest MODIS C6 fire product is retrieved following the method developed by Wooster et al. (2003), which uses parameters including: the radiances of the fire pixel at the 4-μm band , the radiances of the ambient non-fire pixels at the 4-μm band, area of the fire pixel, and a sensor-specific coefficient (3.0×10^{-9} $W \cdot m^{-2} \cdot sr \cdot \mu m^{-1} \cdot K^{-4}$) (Giglio et al., 2016a). The MODIS C6 Level-2 active fire product records FRP retrievals in units of MW (per pixel).

The Level-2 MYD14 product is generated in an Aqua MODIS sensing geometry (Table 4-1) (Wolfe et al., 1998; Wolfe et al., 2002). MODIS scans ten lines of nominal 1-km pixel per mirror rotation over ±55° approximately every 1.477 s, and each scan line is composed of 1354 pixels with a swath width of 2340 km (Wolfe et al., 2002). The nominal pixel dimension increases from ~1 km at nadir to ~2.01 km along the track direction and ~4.83 km along the scan direction at the scan edge (Wolfe et al., 1998). Adjacent scans overlap each other up to 50% from scan angles of 24° to the scan edge (Wolfe et al., 2002), which can result in duplicate fire detections. Furthermore, duplicate fire detections can also result from the triangle-shaped point spread function (PSF) of MODIS (Freeborn et al., 2014). Moreover, MODIS can observe the same fires repeatedly from adjacent orbits at mid-to-high latitudes as its adjacent orbits overlap each other. In addition, MODIS misses observations inside the daily coverage gaps between adjacent orbits along the entire equatorial region between 30°S and 30°N latitudes (Figure 4-1a).

For the comparison with Suomi NPP VIIRS fire data, we obtained the Aqua MODIS C6 Level-2 active fire product (MYD14) and geolocation product (abbreviated MYD03 for Aqua) from NASA's Level-1 and Atmosphere Archive & Distribution System (LAADS) (https://ladsweb.modaps.eosdis.nasa.gov/) for the period from April 2016 to March 2017. The geolocation product MYD03 was used to locate and extract the overlap areas between Aqua MODIS adjacent orbits.

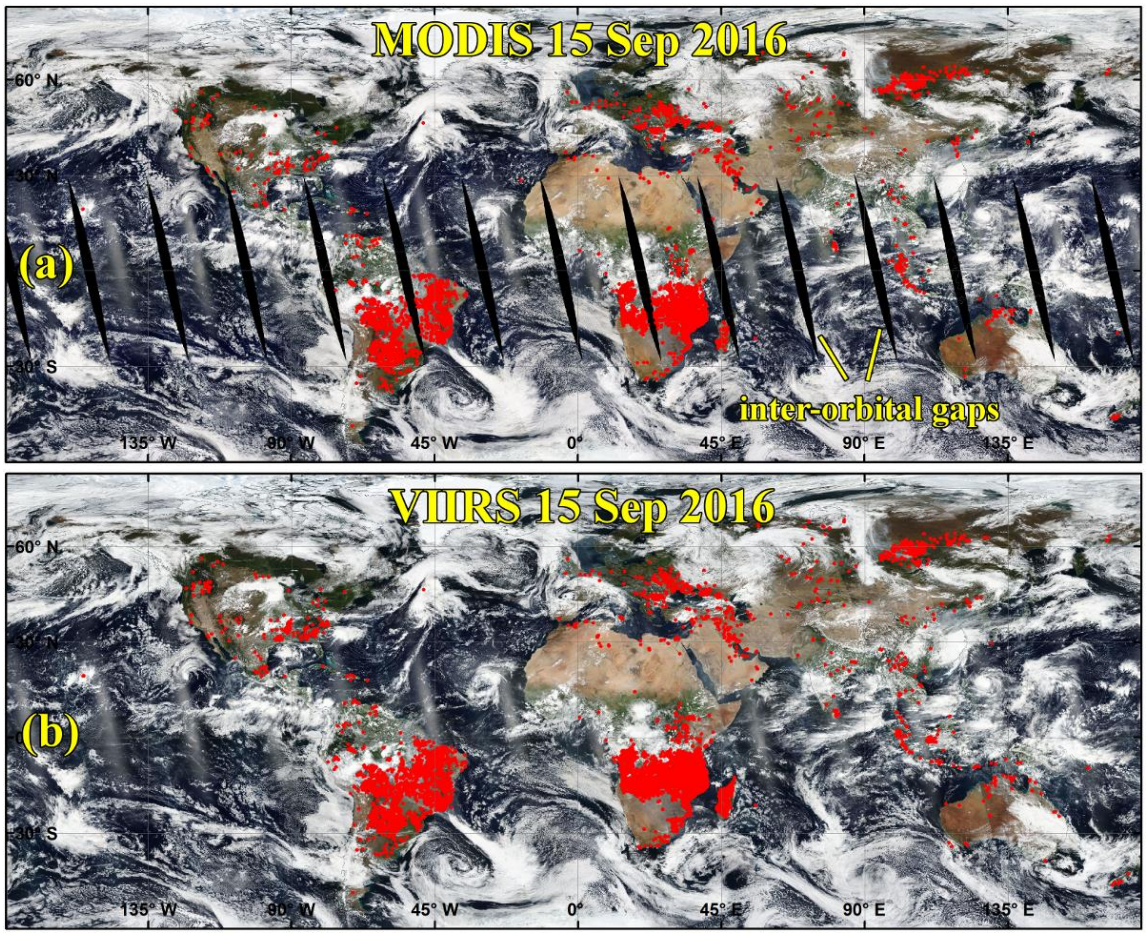

Figure 4-1. Global active fire detections from Aqua MODIS and Suomi NPP VIIRS on 15 September 2016. (a) Daytime Aqua MODIS fire detections (red dots), which miss all fires burning inside the inter-orbital gaps (black narrow ellipses) in the low-latitude regions. (b) Daytime VIIRS fire detections (red dots), which provides daily full coverage of the globe.

4.2.2. VIIRS 750-m Active Fire Data

The newly operational NOAA VIIRS active fire product, the 750m Suomi NPP Data Exploitation Level 2 active fire (NDEAF-L2), provides daily globally active fire data (Csiszar et al., 2016). The VIIRS NDEAF-L2 fire product is built on the modified active fire detection algorithm of the MODIS C6 active fire product (Giglio et al., 2016b) and will extend to the JPSS satellites (Csiszar et al., 2016). This product is also compatible with the 750m VIIRS active fire products generated within NASA's Land Science Investigator-led Processing System (Land SIPS). As with the MODIS active fire product, the VIIRS fire product contains for each fire pixel the detection time and coordinates (longitude and latitude) and confidence, fire radiative power, brightness temperatures at 4-μm and 11-μm bands, and satellite VZA (Csiszar et al., 2016). The FRP (units: MW per pixel) recorded in the VIIRS NDEAF-L2 fire product is also retrieved based on the method proposed by Wooster et al. (2003). Although the algorithms for the VIIRS NDEAF-L2 fire product and the MODIS C6 active fire product are almost the same (Csiszar et al., 2016; Giglio et al., 2016a), MODIS and VIIRS sensors differ in the primary bands that are used for fire detection and FRP retrieval, their wavelengths, saturation temperatures, pixel sizes, and sensor-specific coefficient (Table 4-1).

The VIIRS NDEAF-L2 fire product is produced in the sensing geometry of the VIIRS M-bands (Table 4-1) (Cao et al., 2014; Wolfe et al., 2013). The VIIRS M-bands sense 16 nominal-750-m pixel scan lines per scan with a scan angle range of ±56.28° from nadir approximately every 1.786 s, and each scan line is composed of 3200 pixels

that cover 3000 km along the scan direction (Cao et al., 2014; Wolfe et al., 2013). Thus, the wider swath width, compared to MODIS, provides fully global coverage without gaps (Figure 4-1b). Coverage from adjacent orbits increasingly overlaps away from the Equator toward higher latitudes, which can cause repeat detections of the same fires. Moreover, the nominal VIIRS pixels are generated using an aggregation scheme that determines the radiance value of a pixel from three samples in nadir along the scan direction (scan angle < 31.72°), from two samples in the middle zone of a scan (scan angle: 31.72° - 44.86°), and from one sample at the scan edge (scan angle > 44.86°), respectively. As a result, the growth rate of the VIIRS pixel size with view angle is largely reduced relative to MODIS observations (Wolfe et al., 2013). The pixel size of M-bands generally increases along the scan direction from nominal 0.75 km at nadir to ~1.6 km at the scan edge but decreases abruptly at the ends of aggregation zones (Wolfe et al., 2013). Moreover, the VIIRS onboard bow-tie deletion algorithm removes two and four over-sampling scan lines in the middle aggregation zone and at scan edge, respectively (Wolfe et al., 2013), thereby reducing duplicate fire detections between adjacent scans at off-nadir. This deletion theoretically results in significantly fewer duplicate fire detections than MODIS.

This study collected the VIIRS NDEAF-L2 active fire product and the Moderate Bands Terrain Corrected Geolocation (GMTCO) product from the NOAA Comprehensive Large Array-Data Stewardship System (CLASS) (https://www.class.ncdc.noaa.gov/) for the period of April 2016 to March 2017. The GMTCO product was used to locate and extract the overlap areas between the Suomi NPP VIIRS adjacent orbits.

Table 4-1. Comparison between MODIS and VIIRS data in sensing geometry and the algorithms used for active fire characterization.

Sensor Parameters	MODIS (Aqua)	VIIRS (Suomi NPP)
Orbit altitude	~705 km	~840 km
Equator crossing time	1:30 AM, and 1:30 PM local time	1:30 AM, and 1:30 PM local time
Scan angle range	±55°	±56.28°
Swath width	2340 km (1354 pixels)	3000 km (3200 pixels)
Pixel dimensions	1 km (nadir) - 2.01 km (along track), 1 km (nadir) - 4.83 km (along scan)	750 m (nadir) - 1.60 km (along track), 750 m (nadir) - 1.60 km (along scan)
Swath width	2340 km (1354 pixels)	3000 km (3200 pixels)
Fire detection Primary bands Saturation temperature	B21 (3.929 - 3.989 μm) B22 (3.940 - 4.001 μm) B31 (10.780 - 11.280 μm) B21, B22, and B31 saturate at nearly 500 K, 331 K, and 340 K, respectively.	M13 (3.987 - 4.145 μm) M15 (10.234 - 11.248 μm) M13 nominally saturates at 343K and 634 K at high and low gain settings, respectively; and M15 saturates at 363 K.
Active fire detection algorithm	MODIS Collection 6 (C6) active fire detection algorithm (Giglio et al., 2016a)	The VIIRS NDE fire algorithm keeps the core and main body of MODIS C6 algorithm but it is slightly modified in separating fire pixel from background clear land pixels. To separate fire pixel from background land pixels, the VIIRS NDE uses the fixed thresholds test (see Giglio et al., 2003) while the MODIS C6 combines the same fixed thresholds test and a new dynamic threshold test (see Giglio et al., 2016a).
FRP calculation	Based on Wooster et al (2003), MODIS sensor-specific coefficient (3.0×10^{-9} W m^{-2} sr μm^{-1} K^{-4})	Based on Wooster et al (2003), VIIRS sensor-specific coefficient (2.88×10^{-9} W m^{-2} sr μm^{-1} K^{-4})

4.2.3. Land Cover Data

The MODIS land cover type was collected to determine the ecosystem types of fire occurrences. The primary land cover classification scheme in the MODIS land cover product (MCD12Q1) is provided by an International Geosphere-Biosphere Program (IGBP) (Friedl et al., 2010). This study used the most recent version of the MODIS land cover type product at a spatial resolution of 500m in 2014 to examine the association between the fire detections from MODIS and VIIRS and the ecosystem types.

4.3. Methods

4.3.1. Correction of Inter-Scan Duplicate Fire Detections

The duplicate fire detections between adjacent scans in MODIS and VIIRS fire products were extracted separately and the associated FRP values were corrected. Fire pixels were considered as duplicate detections if they met the following three conditions: (1) Fires are detected at the same satellite view angles. (2) The time difference between any two fire observations is less than 8 s, which is because the same point on the Earth's surface could be sensed by up to three temporally adjacent scans at the scan edge during a time period of 4.431seconds (the time of completing three scans is 3×1.477 s) for MODIS (Wolfe et al., 2002) and 5.358 seconds (3×1.786 s) for VIIRS M-bands, although ground-received VIIRS data are less likely to contain the same surface point from all three adjacent scans due to the onboard deletion algorithm (Wolfe et al., 2013). (3) The

distance between the centers of any two fire pixels is shorter than the along-track dimension of the fire pixels because adjacent scans primarily overlap each other along the track direction. For each pair of duplicate detections, one remained while the other was removed, and the average FRP was used as the corrected FRP value for the retained detection. Figure 4-2 shows an example of correcting MODIS inter-scan duplicate fire detections in nine temporally adjacent scans (117th – 225th) at a satellite view angle from 55° to 58°, where a total of 40 pairs of duplicate fire detections were found and fully corrected.

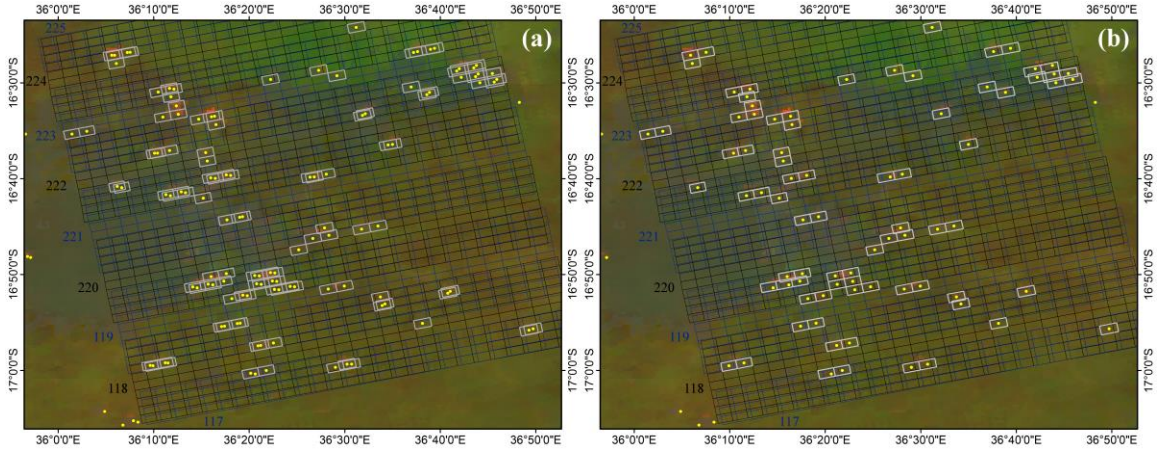

Figure 4-2. An example of correcting MODIS inter-scan duplicate fire detections for savanna fires in southern Africa on 18 September 2016. (a) Before inter-scan correction. Nine temporally adjacent scans (117th – 225th) sensed at 11:50 (UTC) are overlaid on a false-color composite image of 500m Aqua MODIS band 7 (2105-2155 μm), band 2 (841-876 μm), and band 4 (545-565 μm), in which actively burning fires are denoted in red (or orange) color. Adjacent scans are in black and dark blue colors, respectively. Each scan has ten scan lines and only 28 pixels at a view angle from 55° to 58° in each scan line (1354 pixels) are shown here. Pixel boundaries are delineated by black or dark blue polygons and the detected fire pixels are highlighted in white color with centers represented by yellow dots. Obviously, four scan lines in every two of adjacent scans

overlap and the duplicate fire detections are those highlighted overlapping fire pixels with very close pixel centers. (b) After inter-scan correction.

4.3.2. Correction of Inter-Orbital Duplicate Fire Detections

The duplicate detections of the same fires observed by Aqua MODIS and Suomi NPP VIIRS on adjacent orbits were extracted. Due to the overlap of among swaths from adjacent orbits at large VZA (VZA>40°), a fire could be repeatedly detected twice (by two adjacent orbits) across mid-latitudes (Aqua MODIS: 30°S-61°S and 30°N-61°N, VIIRS: 54°S-54°N) and up to four times (by four adjacent orbits) across high latitudes (Aqua MODIS: 61°N-80°N, VIIRS: 54°N-80°N) during either daytime or nighttime every day if the fire is intense and detectable at a large view angle with a large pixel size. Relative to MODIS, the VIIRS sensor has a much higher chance to detect the same fire from adjacent orbits because VIIRS M-bands have a generally consistent pixel size from nadir to the scan edge. To correct the inter-orbital duplicate detections, the daily overlap areas between adjacent orbits of each sensor were first built by spatially matching the associated swaths sensed from the adjacent orbits. Swath boundaries were constructed using the coordinates of the scan edges obtained from geolocation products (MYD03 for Aqua MODIS and GMTCO for VIIRS). Then, for every pair (or group) of the overlapping orbits, the fire pixels from one orbit inside the overlap area were extracted and buffered by a distance of the along-scan pixel dimensions at scan edge (4.83 km for MODIS and 1.6 km for VIIRS). For fire detections from the other orbit (or orbits), the detections located within the buffers were considered to be potential duplicate detections; otherwise, the detections outside the buffers were considered to be new fires. The

buffered detections and their potential duplicate detections from either MODIS or VIIRS were then processed in the following three ways to determine whether the potential duplicate detections could be new fires. (1) Both the buffered and the potential duplicate fires remained if they were detected by both MODIS and VIIRS. (2) Only the fires detected by both MODIS and VIIRS remained if one of the sensors only observed either the buffered or potential duplicate fires. (3) Only the detections with smaller VZA remained if both the buffered and the potential duplicate fires were only detected from either MODIS or VIIRS. The selection of smaller VZA fire detection was based on the fact that the fire-detection capability decreases as the view angle increases (see Section 4.4.2). Additionally, all detections of new fires from the other orbits were also kept.

4.3.3. Comparison between MODIS and VIIRS FRP Retrievals

To provide sufficient understanding of the similarity and discrepancy between MODIS and VIIRS FRP retrievals, we explored the FRP variations in four different ways. First, the dependence of MODIS and VIIRS FRP on VZA was examined and compared because of the differences in sensing geometry between the two sensors (Table 4-1). To ensure both sensors sensed the fires contemporaneously in the same area, the Aqua MODIS granules were matched with the VIIRS granules temporally and spatially. Specifically, for each 5-min Aqua MODIS granule (based on MYD03), VIIRS granules (based on GMTCO) that temporally (±5 min) and spatially (overlapping) matched the MODIS granule were first selected. Then, the fires detected inside the overlap areas between the MODIS granule and the matched VIIRS granules were considered as the

contemporaneous fire detections because the variations of fires and atmosphere within ±5 min could be negligible. This process was repeated for all MODIS and VIIRS granules from April 2016 to March 2017 globally. Finally, the contemporaneous fire detections were grouped with an interval of every 1-degree VZA, and the associated FRP values were then summed in each group for MODIS and VIIRS, respectively. The mean, minimum and maximum FRP (per fire pixel) were further calculated for each sensor for comparisons.

Second, to understand the FRP variation in individual fire clusters, MODIS and VIIRS FRP estimates were compared for individual fire events that occurred during fire seasons in five typical ecosystems (savannas, tropical rainforests, boreal forests, broadleaf forests, and croplands) (Table 4-2 and Figure 4-3). To minimize the effect of differences in observation time and VZA between MODIS and VIIRS, fire detections were extracted from those observed by both MODIS and VIIRS within a time difference of less than 20 min and a VZA difference of less than 15°. Using 20 min instead of 5 min was chosen to collect more contemporaneous fire detections with similar VZA and without cloud obscurations from both MODIS and VIIRS. A fire cluster was then manually enclosed using a polygon as shown in Figure 4-3 (d, g, j, m, and p). For visualization purposes, the extracted fire detections were overlaid with a false-color composite image of 500m MODIS. The fire detections from MODIS and VIIRS were clustered around one or several fire pixels (red or orange color) on the MODIS false-color image. Figures 4-3b-p present examples illustrating the fire clustering of active fire detections from MODIS and VIIRS in five ecosystems, where a large fire event could consist of several fire clusters. To select clusters representing various fire characteristics,

a total number of 619 fire clusters were quantified from 13 regions globally (Table 4-2). For a fire cluster, VZAs were averaged and FRP retrievals were summed from all enclosed fire detections at each overpass for MODIS and VIIRS separately. Finally, the cluster-level FRP estimates from the two sensors were compared for each of the five ecosystems using the Reduced Major Axis (RMA) regression method that minimizes error in both dependent and independent variables (Smith 2009). RMA regression has been widely used to compare measurements or estimates of the same geophysical or biophysical variable by different instruments (Boersma et al., 2009; Cohen et al., 2003; White et al., 2009). In this comparison, the fitted line was forced through the origin because both sensors observed the same fire clusters (or events) contemporaneously. The Pearson's correlation coefficient (r) was also calculated as an indicator of correlation between FRP estimates from the two sensors.

Third, the discrepancy between MODIS FRP and VIIRS FRP was investigated at a continental scale. The extracted contemporaneous fire detections (an overpass difference of within ±5 min) from the two sensors, which were obtained from MODIS and VIIRS granules described in the first paragraph of this section, were separated into two groups by daily overpass times: (1) an early morning group at approximately 1:30 AM local time (nighttime fires) and (2) an early afternoon group at approximately 1:30 PM local time (daytime fires). For each of the daytime and nighttime groups, FRP retrievals of all contemporaneous fire detections from each sensor in the same day were summed separately for the six continents (North America, South America, Europe, Africa, Asia, and Australia). Then, the continental FRP estimates from the two sensors

were statistically compared using the RMA regression. The regression intercept was kept because MODIS and VIIRS were not always able to detect the same fires.

Table 4-2. Selected fire clusters at five typical ecosystems in 13 regions across the globe.

Ecosystem	Region	Fire season*	Cluster number	Observing date	Observing difference	
					Time (min)	VZA (degree)
Savannas	Northern Africa	Nov-Jan	45	02 Nov 2016	15	< 10
	Southern Africa	Jul-Sep	75	22 Aug 2016	15	< 15
	Australia	Apr-May, Oct-Dec	38	15 Oct 2016	0	< 15
Tropical Rainforest	Amazon	Aug-Sep	100	07, 15 Sep 2016	5-10	< 10
	Southeast Asia	Jan-Apr	22	27 Jan, 05 May 2016	5-10	< 10
	East Congo	Aug-Oct	40	11 Jul, 30 Aug 2016	10-15	< 10
Boreal forest	North America	May-Sep	28	02 Jul 2016	15	< 5
	Siberia	May-Sep	58	18 Sep 2016	10	< 5
Broadleaf forest	Chile	Dec-Jan	98	21, 26, 29 Jan 2017	5-20	< 10
Croplands	Southeast United States	Sep-Oct	79	28 Sep, 06, 09, 25 Oct 2016	5-20	< 15
	Ukraine	Jul-Aug	20	13, 26 Jul 2016	5-10	< 15
	Northwest India	May & Oct	16	28 Oct 2016	0	< 10

* Fire seasons were derived based on (Giglio et al., 2006).

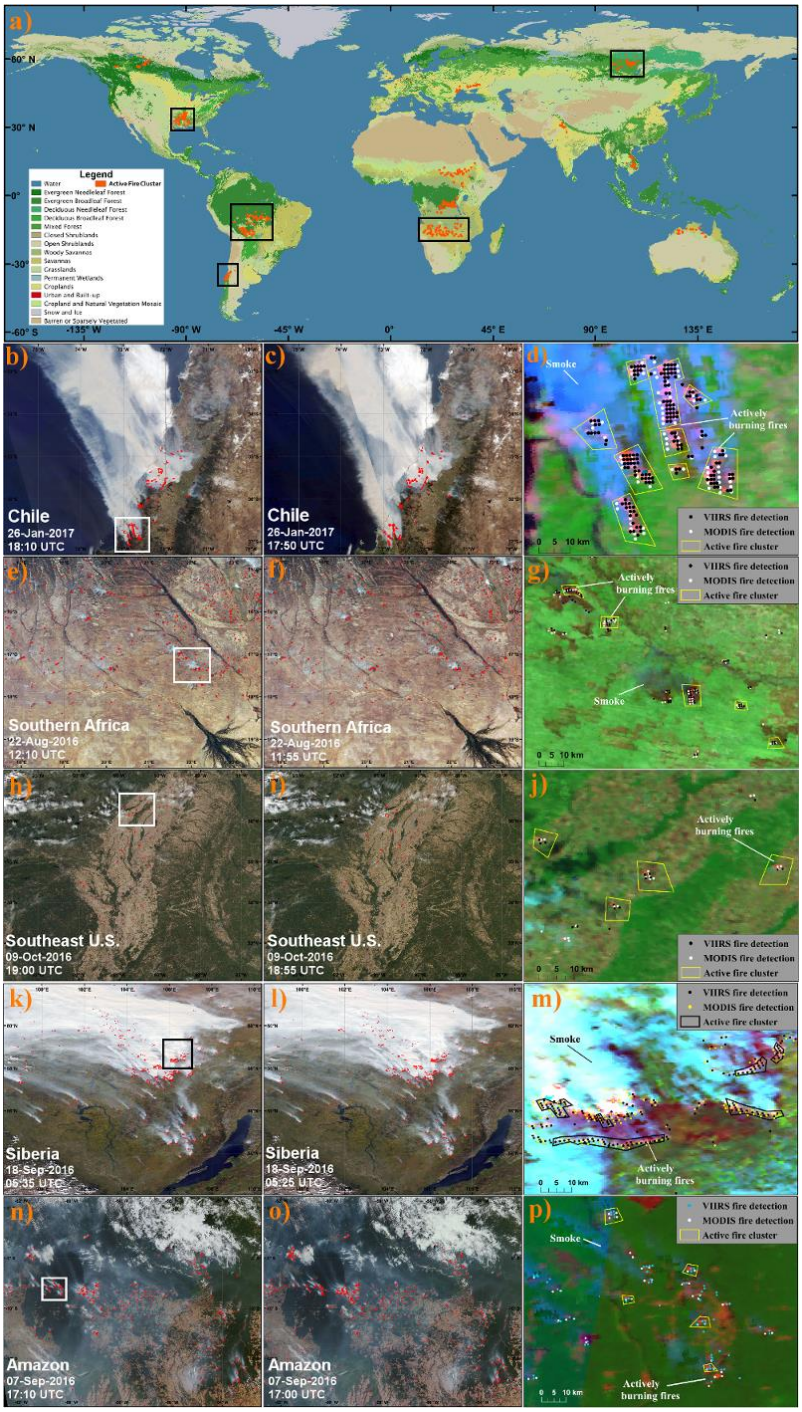

Figure 4-3. Fire clusters in five typical ecosystems selected globally. The top panel (a): the distribution of 619 fire clusters over 13 regions of savannas, tropical rainforest, boreal forests, broadleaf forest, and croplands (Table 4-2). The five black squares highlight the example regions used for illustrating fire clustering in the bottom panel. The bottom panel (b-p): examples of active fire detections by MODIS (the first column: b, e, h, k, and

n) and VIIRS (the second column: c, f, i, l, and o) in one region of every ecosystem, and several manually selected fire clusters (the third column: d, g, j, m, and p) in the areas delineated by the white or black contours in the first column (b, e, h, k, and n). Fire clusters (highlighted by yellow or black polygons) were overlaid with the 500m MODIS false-color composite image of bands 7-2-4 in which actively burning fires are in red (or orange).

Fourth, the discrepancy between MODIS FRP and VIIRS FRP was also investigated spatially at 1° grid cells across the globe. This comparison used all fire detections with the correction of duplicate detections for the following two reasons. First, the samples for statistical analyses were too small in a grid cell and were unrepresentative if only using the contemporaneous fires detections (within ±5min) from MODIS and VIIRS overpasses. Indeed, because of the overpass-time shifts between MODIS and VIIRS orbits, the contemporaneous detections occurred approximately one day every eight days (or ~45 days during an entire year) in the same area. For an area with a fire season approximately 1-2 months, the contemporaneous fire detections only appeared in 3-7 days. In that case, the extracted contemporaneous fires detections could be unable to represent the fire activities. Second, the operational biomass burning emission products, including the Quick Fire Emissions Dataset (QFED) (Darmenov and Silva, 2015), the Global Fire Simulating System (GFAS)(Kaiser et al., 2012) and the Blended Global Biomass Burning Emissions Product from MODIS, VIIRS and Geostationary Satellites (GBBEPx) (Zhang et al., 2014), estimate emissions at grid cells based on daily mean FRP flux (units: $W \cdot m^{-2} \cdot s^{-1}$) that is calculated using daily MODIS FRP retrievals. Therefore, the use of all corrected fire detections helps to understand the uncertainties of estimating emissions from VIIRS and MODIS FRP retrievals. To explore the spatial pattern of the

FRP discrepancy, the VIIRS-to-MODIS FRP ratio was calculated at 1° grid cells by adopting a method that has been developed in previous studies (Ellicott et al., 2009; Freeborn et al., 2009; Roberts and Wooster, 2008; Roberts et al., 2015; Vermote et al., 2009; Wooster et al., 2015), in which the FRP ratio was applied to compare the FRP retrievals between MODIS and the Spinning Enhanced Visible and Infrared Imager (SEVIRI) across Africa and between Aqua MODIS and Terra MODIS across different regions globally in a temporal interval of one week, one month, or one year. In this study, the corrected fires detections from the two sensors were separately gridded into 1° grid cells. Then, the VIIRS-to-MODIS FRP ratio was calculated for every grid cell as,

$$\phi_{FRP} = \frac{\sum_{i_{VIIRS}=1}^{n_{VIIRS}} FRP_{i_{VIIRS}}}{\sum_{i_{MODIS}=1}^{n_{MODIS}} FRP_{i_{MODIS}}} \quad (1)$$

where ϕ_{FRP} is the VIIRS-to-MODIS FRP ratio, i_{VIIRS} and i_{MODIS} are the indices of fire pixel number, and n_{VIIRS} and n_{MODIS} are the total number of corrected fire pixels in a grid cell for VIIRS and MODIS observations, respectively, from April 2016 to March 2017. Note that ϕ_{FRP} was not calculated for grid cells that fewer than 10 fire pixels were observed by either MODIS or VIIRS during the period.

Fire pixel density (units: count · km^{-2}) from VIIRS fire detections was also estimated at 1° grid cells to locate frequent fire occurrences and to investigate its influence on the VIIRS-to-MODIS FRP ratio. The fire pixel density was obtained by

dividing the total fire pixel number by the area of the grid cell following the methods presented in Giglio et al (2006) and Ichoku et al (2008).

Finally, the VIIRS-to-MODIS FRP ratio was calculated using equation (1) for all corrected fires detections that were binned by every 5° latitude to explore the MODIS and VIIRS FRP discrepancy along the latitudinal direction.

4.4. Results

4.4.1. Effect of Duplicate Detections on FRP Estimates

Duplicate fire detections from inter-scans (between adjacent pixels at off-nadir and adjacent scans) account for considerable FRP overestimates (Figure 4-4). These duplicate detections account for as much as 9.8% of total fire count, which account for 18.3% of cumulative Aqua MODIS FRP at a global extent. This is similar to the finding from (Freeborn et al., 2014). In contrast, for VIIRS fire detections during the same period, duplicates account for up to 5.4% of the total fire count and 6.7% of the cumulative FRP.

The effect of the inter-orbital duplicate fire detections on FRP estimates is very limited (Figure 4-4). The repeat MODIS detections inside the overlap areas between the adjacent Aqua orbits only make up 0.18% of the total count of Aqua MODIS detections, which merely account for 0.54% of the cumulative FRP. For VIIRS detections, the inter-orbital duplicate detections account for only 0.8% of the total detections and contribute to 1.3% of the cumulative FRP.

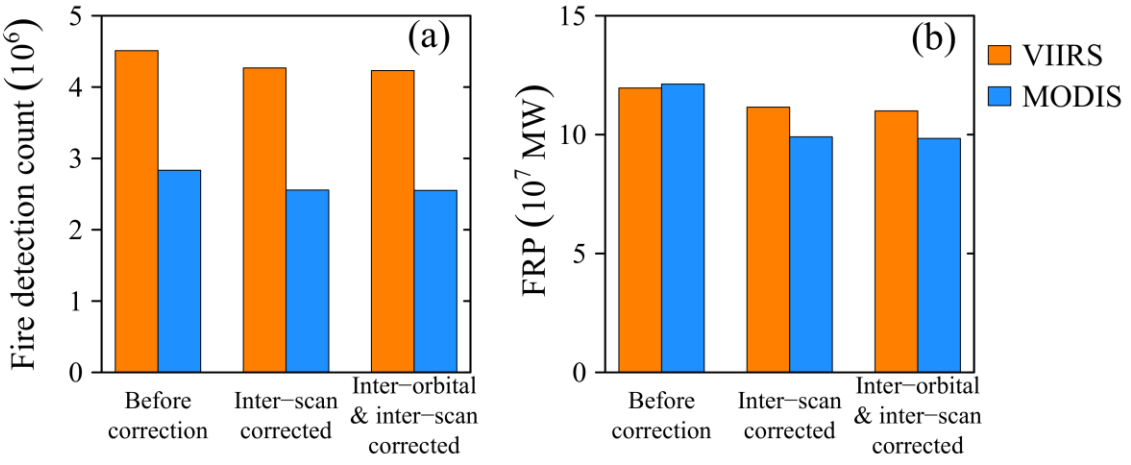

Figure 4-4. Fire detection count and cumulative FRP estimates before and after corrections of inter-scan and inter-orbital duplicate detections during the period from April 2016 to March 2017. (a) Total count of fire detections. (b) Cumulative FRP.

4.4.2. Dependence of FRP Retrievals on Satellite View Zenith Angle

A comparison of the fires that were contemporaneously detected by MODIS and VIIRS shows that the capability of detecting fire across swath is largely variable for MODIS but is relatively consistent for VIIRS (Figure 4-5). The MODIS fire count decreases by 67%, whereas the MODIS mean FRP per detection increases by 300% from 22 MW to 90 MW as VZA increases from nadir to 60° (Figures 4-5a and 4-5b). This variation is attributed to the gradual increase in pixel dimensions as VZA increases (Table 4-1). In contrast, the VIIRS fire count and mean FRP increase minimally by approximately 100% and 110%, respectively, from nadir to scan edge. The peaks of VIIRS fire count (also mean FRP) occur at approximately VZAs of 38° and 54° due to the change in pixel size associated with the onboard aggregation scheme (Wolfe et al., 2013). The discrepancy due to the sensing geometry difference between MODIS and

VIIRS can also be seen in the minimum FRP per detection (in 1° VZA bin) that increases from 1.8 MW to 3.6 MW for VIIRS and 2.5 MW to 17.0 MW for MODIS as VZA increases from nadir to 60° (Figure 4-5c). The maximum FRP per detection from both VIIRS and MODIS shows large variation but generally increases as VZA increases from nadir to 60° (Figure 4-5c). In general, the sum of FRP estimates from VIIRS fire detections is 11% larger than that from MODIS fire detections, except for VZAs between nadir and +20° (Figure 4-5d).

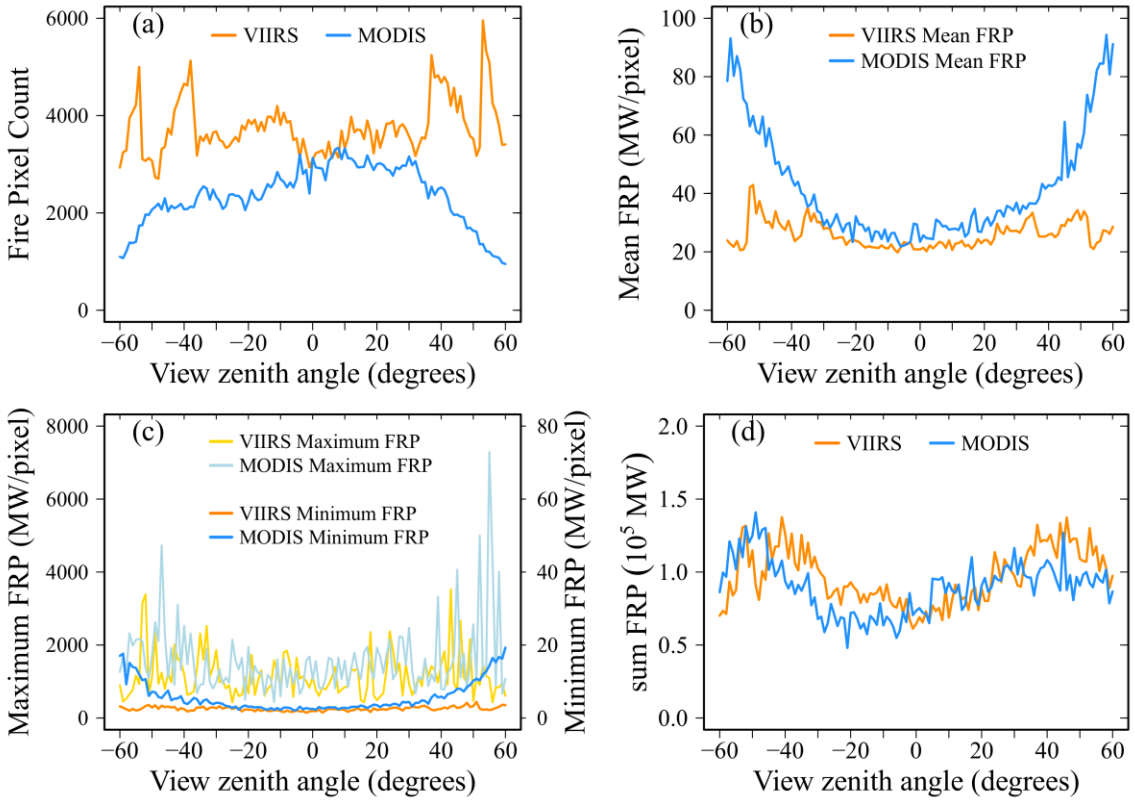

Figure 4-5. Variations of fire pixel count, sum FRP, mean FRP, the minimum and maximum FRP with view zenith angle for the daytime fires contemporaneously detected from MODIS and VIIRS from April 2016 to March 2017 globally. (a) Fire detection count, (b) mean FRP per fire detection, (c) the maximum and minimum FRP per fire detection (the minimum FRP is on the right Y-axis), and (d) sum of fire FRP, in every 1° VZA bin.

4.4.3. Fire Cluster FRP

VIIRS and MODIS FRP estimates are mostly comparable in fire clusters, although there is a dependency on the host ecosystem (Figure 4-6). VIIRS FRP differs from MODIS FRP by approximately 1% in croplands and savannas. The regression coefficient (slope) suggests that the cluster FRP estimates from the two sensors are statistically similar in these two ecosystems with a Pearson's r of 0.72 and 0.81 (Figure 4-6a, b). The MODIS and VIIRS FRP estimates are also similar in broadleaf forests and tropical rainforests with a Pearson's r that is larger than 0.9. The cluster VIIRS FRP is approximately 13% larger than MODIS FRP, although a few cluster samples show larger MODIS FRP estimates in broadleaf forests (Figure 4-6c). A small difference is observed in tropical rainforests where the cluster VIIRS FRP is approximately 8% smaller than MODIS FRP (Figure 4-6d).

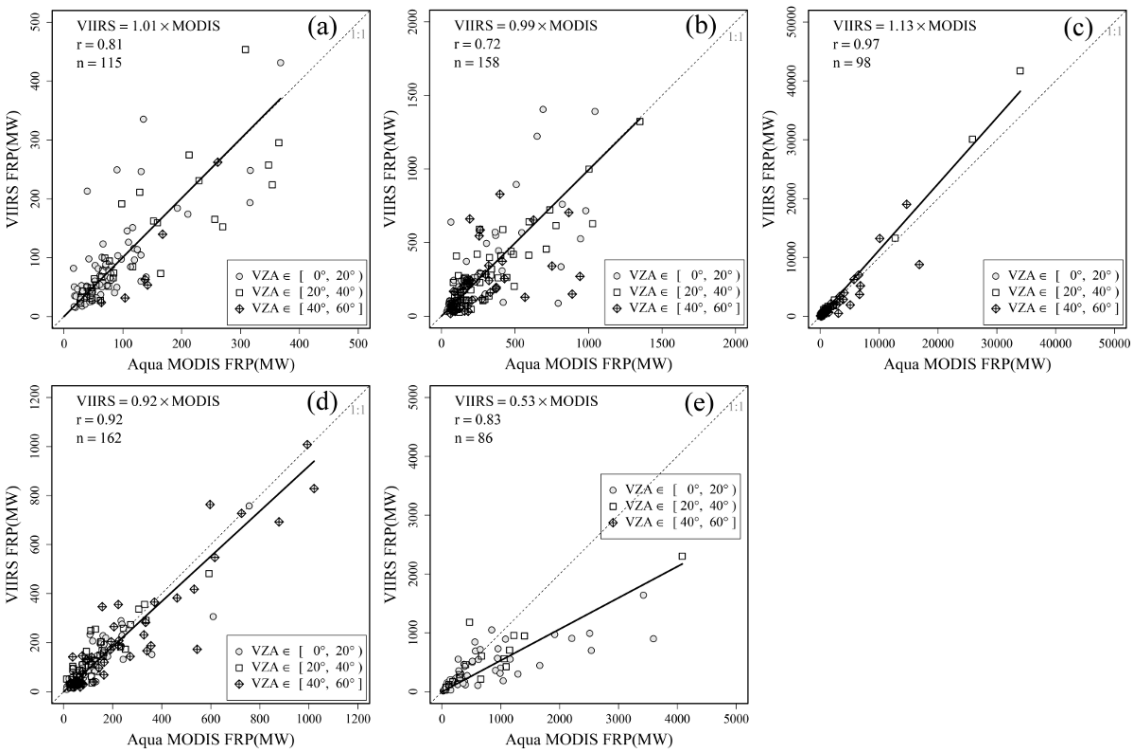

Figure 4-6. Comparison of fire cluster FRP between VIIRS and MODIS estimates in five typical ecosystems. (a) croplands, (b) savannas, (c) broadleaf forests, (d) tropical rainforests, and (e) boreal forests. Each sample represents one fire cluster. All samples are separated into three groups by the associated VZA (0°-20°, 20°-40°, and 40°-60°), and are represented using different symbols. The solid line is the fitted line and the dashed line is the 1:1 line.

However, the cluster VIIRS FRP estimates differ greatly from MODIS FRP in boreal forests (Figure 4-6e). Samples with a cluster FRP estimate less than 1000MW are evenly distributed around the 1:1 line. Nevertheless, MODIS FRP is 47% larger than VIIRS FRP in large cluster FRP samples (cluster FRP > 1000MW).

Although the samples have a VZA variation of 0° to 60°, the relationship of cluster FRP between MODIS and VIIRS retrievals does not show any dependence on VZA. This pattern appears in all five ecosystems.

4.4.4. Continental-Scale FRP

The continental-scale daily daytime FRP retrieved from VIIRS and MODIS contemporaneous fire detections is highly correlated (Pearson's $r \geq 0.98$) in all six continents although slight differences exist (Figure 4-7). In South America, Asia, and Australia, most of the samples are distributed around the 1:1 line with a slope that is close to one and a relatively small intercept, which suggests that the continental FRP differences between MODIS and VIIRS are generally very small. However, an FRP difference is observed in some periods during the year in South America and Australia. For instance, the VIIRS FRP estimates are slightly lower than MODIS FRP during August and September in South America (a time period dominated by deforestation fires) but are slightly larger from October-November (a time period dominated by savanna fires) in Australia.

Although the regression slope between MODIS and VIIRS FRP estimates is close to one in Africa, the fitted line shifts toward the VIIRS side with a moderate systematic bias (Figure 4-7d). This indicates that the VIIRS FRP estimates are overall larger than MODIS FRP. The seasonal variation shows that the VIIRS FRP estimates are larger than MODIS FRP in the periods from January-April and August-December (time periods

dominated by savanna fires in Northern and Southern Africa) but are smaller from May-July (a time period dominated by forest fires in central Africa rainforest).

The regression lines also show that VIIRS FRP is overall larger than MODIS FRP in North America and Europe (Figure 4-7a and 4-7c). In North America, the difference is mostly associated with agricultural burning and grassland fires that primarily occur during the period from March-June in Mexico, as well as the central and southeastern United States. In Europe, the overall larger FRP estimates of VIIRS than MODIS is related to agricultural burnings that begin in June and end in October.

Compared to the daytime continental FRP, the nighttime continental FRP estimates are much smaller and less correlated (Figure 4-8). This difference is likely associated with the much smaller and cooler fires that occur at night compared to daytime fires. Among the six continents, VIIRS FRP is overall larger than MODIS FRP in Europe and Africa but smaller in North America, South America, and Australia. However, FRP estimates between the two sensors are very comparable in most samples in Asia.

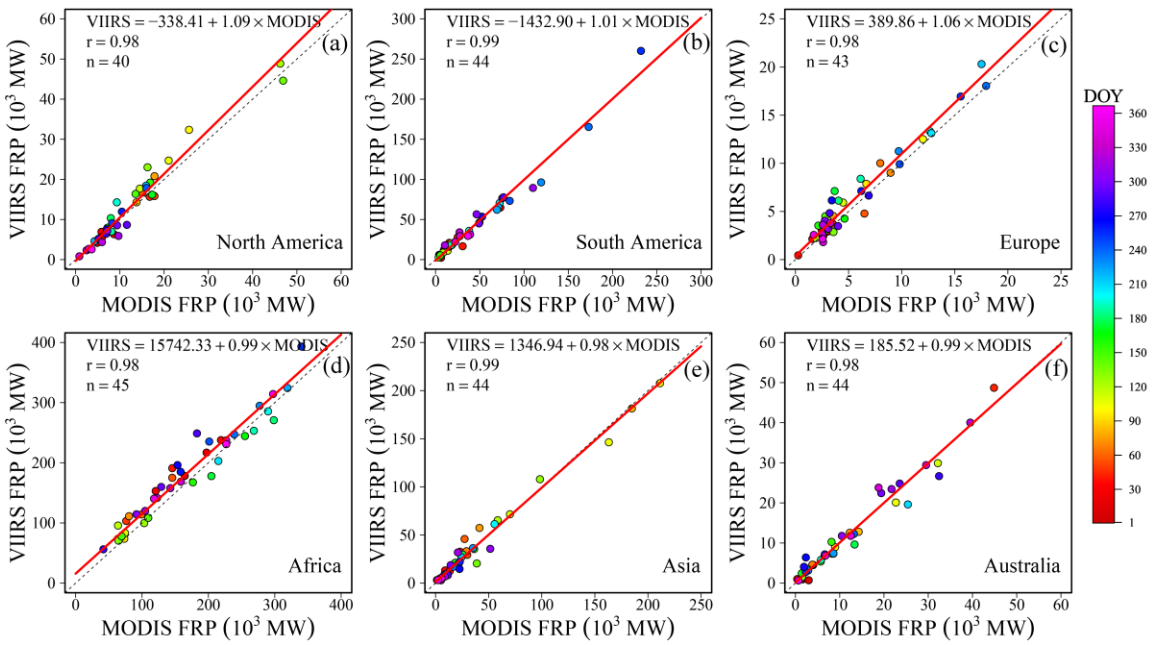

Figure 4-7. Comparisons of daily continental FRP estimates from daytime fire detections contemporaneously sensed by VIIRS and MODIS during the period from April 2016 to March 2017 in six regions: (a) North America, (b) South America, (c) Europe, (d) Africa, (e) Asia, and (f) Australia. The solid line (red) is the fitted line and the dashed line is the 1:1 line. The date (day of year or DOY) of each sample is represented by different colors (see legend on the right).

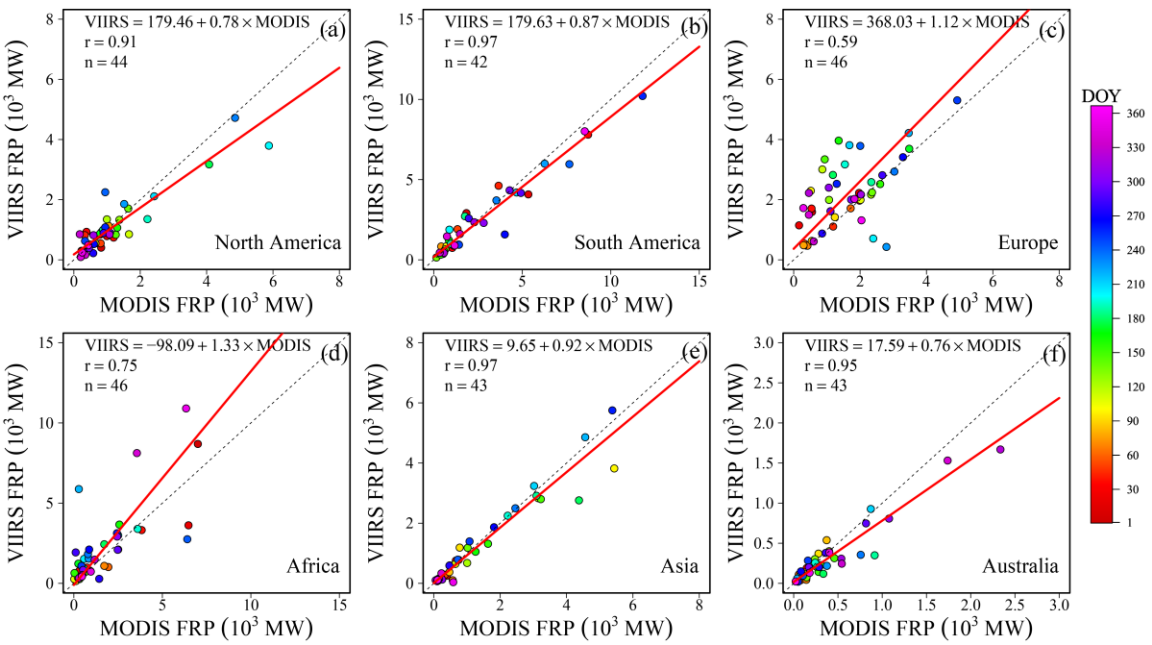

Figure 4-8. The same as in Figure 4-7 but for nighttime contemporaneous fire detections.

4.4.5. Spatial Pattern of Global FRP

The difference between VIIRS FRP and MODIS FRP estimates at grid cells is small in fire-prone regions (Figure 4-9). The fire-prone regions are quantified using the VIIRS fire pixel density showing large values for frequent fire occurrences (Figure 4-9a). These regions are mainly distributed in tropical and subtropical climate zones (including Africa, most parts of South America and Central America, Southeast Asia, and northern Australia). In fire-prone tropical and subtropical regions with a VIIRS fire pixel density that is larger than 0.05 count per square kilometer in a year, the VIIRS-to-MODIS FRP ratio shows that the VIIRS FRP estimates are, on average, 20% larger than MODIS FRP at the grid level (Figure 4-9b, c). The VIIRS-to-MODIS FRP ratio is consistent in fire-prone regions, whereas it varies dramatically in fire-limited regions where the VIIRS fire

pixel density is less than 0.02 count per square kilometer in a year (Figure 4-9c). The FRP ratio in fire-limited regions is not representative because the fire sample size is too small.

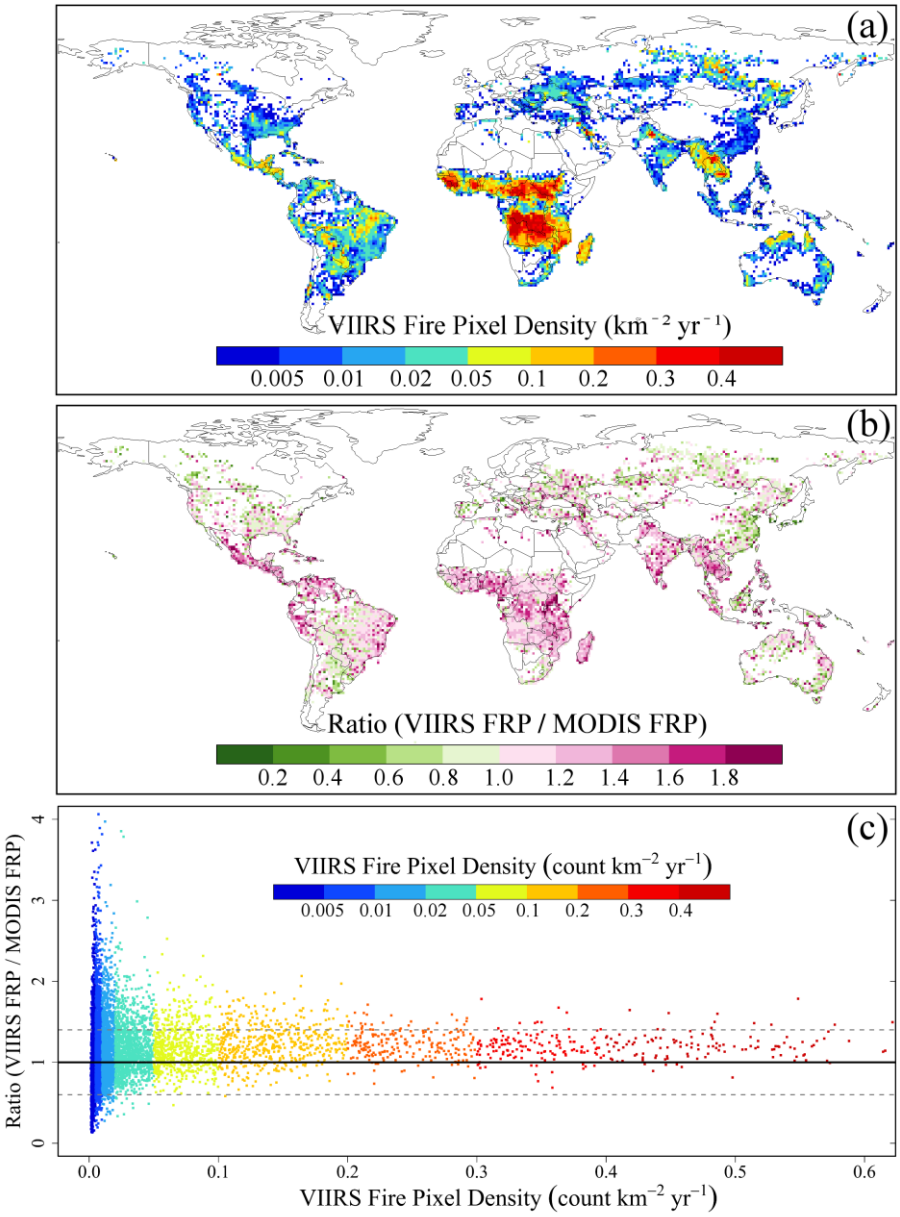

Figure 4-9. The VIIRS fire pixel density and the VIIRS-to-MODIS FRP ratio at 1°×1° grid cells during the period from April 2016 to March 2017. (a) The VIIRS fire pixel density, (b) the VIIRS-to-MODIS FRP ratio, and (c) the VIIRS-to-MODIS FRP ratio in grid cells as a function of VIIRS fire pixel density that is colored for different ranges. The

solid line and the upper and lower dashed lines in (c) are ratio values of 1.0, 1.4, and 0.6, respectively.

The VIIRS-to-MODIS FRP ratio presents the spatial variation of the difference between VIIRS and MODIS FRP estimates in the grid cell across the globe (Figure 4-9b). At low latitudes, the VIIRS FRP estimates are larger than MODIS FRP in most regions that are dominated by agricultural and savanna fires, including croplands in Mexico, India, and Pakistan, and savannas in most of Africa and eastern South America. In contrast, VIIRS FRP is mostly smaller than MODIS FRP in tropical forest fire regions, including areas in transition zones from savannas to rainforests in South America and on some Indonesian islands. In mid-latitudes, the FRP ratio varies considerably within a local region, indicating that the relationship between VIIRS FRP and MODIS FRP is very complex. At high latitudes, VIIRS FRP is generally smaller than MODIS FRP. For instance, in the boreal forests where large and intense fires frequently occur during summer months (July-September) in North America and northern Asia, VIIRS FRP is as much as 40% smaller (much smaller in a few grids) than MODIS FRP although VIIRS FRP is slightly larger in a small portion of grids.

4.4.6. Latitudinal FRP Distributions

VIIRS and MODIS fire counts vary substantially with latitude (Figure 4-10a). At low latitudes between 30°S and 30°N, the annual count of fire detections accounts for over 88% of the total global fire detections. The fire count peaks in the Equatorial

savannas where the fire season spans from August to October in the southern hemisphere and from December to the following March in the northern hemisphere. However, the fire count dips around the equator where tropical rainforests are dominant and fires are less frequent than in tropical savannas. Nevertheless, the fire count at mid-to-high latitudes decreases rapidly. This latitude-dependent pattern is the same for both the raw fire detections and the corrected fire detections. Relatively speaking, the count of the corrected VIIRS fire detections is much larger than that of the corrected MODIS fire detections, particularly in tropical regions (70% larger), which is mainly attributed to the difference in pixel size between the two sensors.

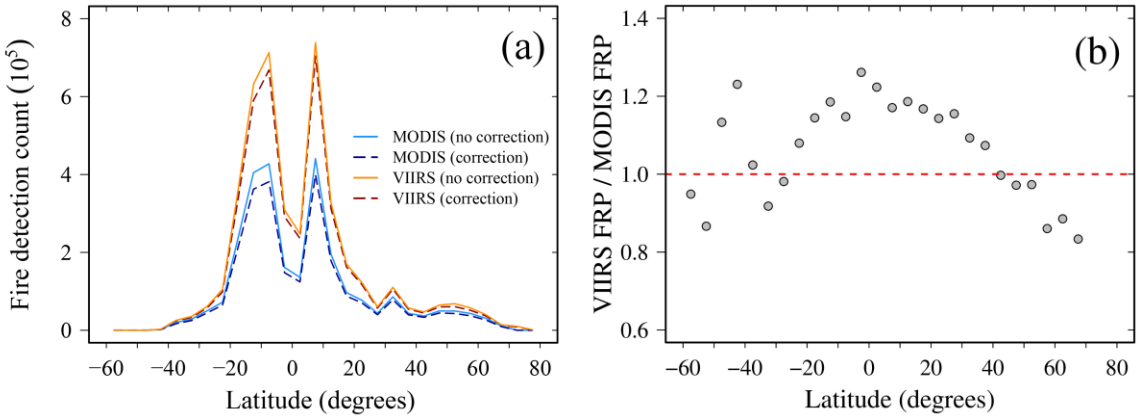

Figure 4-10. Variations in fire detection count and the VIIRS-to-MODIS FRP ratio with latitude during the period from April 2016 to March 2017. (a) The annual total count of fire detection aggregated every 5° latitudes, where solid and dashed lines represent fire detection data before and after corrections of duplicate detections, respectively. (b) The VIIRS-to-MODIS FRP ratio at every 5° latitudes using the corrected fire detection data. The red dash line shows a ratio value of one, indicating VIIRS and MODIS FRP estimates are equal.

VIIRS FRP is generally larger than MODIS FRP at low latitudes but is smaller at mid-to-high latitudes (Figure 4-10b). For the corrected fire detections, the VIIRS-to-MODIS FRP ratio indicates that VIIRS FRP is, on average, approximately 16% larger than MODIS FRP in the tropical zone (30°S - 30°N). In the northern hemisphere, VIIRS FRP is less than MODIS FRP up to 3% in mid-latitudes (30°N - 50°N) but up to 18% at high latitudes (55°N-70°N) where boreal forest fires frequently occur. In the southern hemisphere, the FRP ratio varies from 0.8 to 1.22 at mid-to-high latitudes where fire activity is relatively limited.

4.5. Discussion

The inter-scan duplicate fire detections could result in considerable FRP overestimation while the inter-orbital duplicates have very limited effect on FRP estimates. The inter-scan duplicates in the MODIS fire data increase the cumulative FRP by approximately 2 times more than those in the VIIRS fire data. This suggests that VIIRS fire data are less affected by the inter-scan duplicate detections than MODIS fire data. The difference is mainly because (1) the combined VIIRS PSF in the 3- and 2-pixel aggregation zones is much less likely to produce duplicate detections than the triangle-shaped MODIS PSF (Cao et al., 2014), and (2) the onboard deletion of over-sampled scans in VIIRS largely reduces the bow-tie effect and leads to very limited overlaps between VIIRS adjacent scans (Wolfe et al., 2013). For MODIS, however, the inter-scan duplicate detections result in higher overestimation of the cumulative FRP than total fire count (Figure 4-4). This is because the inter-scan duplicate detections mainly occur at large VZA where mean FRP per detection is several times that of the mean FRP at nadir

(Figure 4-5c). In contrast, the inter-orbital duplicates have very limited or negligible contributions to FRP estimates for both VIIRS and MODIS, although the impacts are stronger on the VIIRS than MODIS fire data because of the wider swath width and large overlap areas in VIIRS (Table 4-1) (Wolfe et al., 2013; Wolfe et al., 2002).

Geometry differences between MODIS and VIIRS sensors could result in considerable discrepancies in fire detection and characterization across swath. The MODIS fire counts decrease quickly as VZA increases, whereas the FRP per count, especially the mean and minimum, increases greatly. This pattern coincides with the variation of MODIS pixel size. In contrast, VIIRS fire detections and FRP per count show limited variations, particularly in large VZAs at off-nadir. This difference in fire detections between the two sensors is because of their different onboard aggregation schemes (Wolfe et al., 2013). Indeed, the large increase in MODIS pixel size across swath greatly decreases the MODIS detection capability, but the slight variation in VIIRS pixel size across swath marginally reduces the VIIRS detection capability, which is clearly demonstrated by the variation of the minimum FRP across swath (Figure 4-5c). Moreover, the difference in the mean FRP per count is mainly because the large MODIS pixels at off-nadir could contain more fire events or areas, whereas VIIRS pixel size is smaller with fewer fire areas. However, VIIRS FRP is larger overall than MODIS FRP across swath, which is attributed to the fact that VIIRS with a smaller pixel size can detect more small fires than MODIS.

The FRP differences between MODIS and VIIRS are also attributed to the differences in sensor spectral bands and satellite overpass time. The impact of the difference in their spectral bands is demonstrated in the cluster FRP comparison. The

carefully extracted fire clusters, after minimizing the differences in overpass time and VZA between MODIS and VIIRS data, provide FRP comparisons of individual fire events in different ecosystems globally. The relationship between the cluster MODIS and VIIRS FRP estimates is significant with a difference of 1% in croplands and savannas and less than 13% in broadleaf forests and rainforests. In boreal forests, however, the cluster MODIS FRP is as much as 47% higher than VIIRS FRP in intensive fire events (cluster FRP > 1000 MW) (Figure 4-6e) where FRP retrievals in nine MODIS fire detections range from 600-2000MW but VIIRS FRP in all fire detections is less than 600MW (Figure 4-11). The underestimation of VIIRS FRP in large boreal forest fires is likely associated with the attenuation of VIIRS FRP by thick smoke plumes because the 4-μm VIIRS M-band has a wider wavelength that contains an important carbon dioxide (CO_2) absorption window than the 4-μm MODIS band (Giglio et al., 2016b). As a result, the increased atmospheric attenuation leads to underestimation of VIIRS FRP and the magnitude of FRP underestimation could be substantial when CO_2-rich smoke plumes block the sensor's instantaneous field of view (Giglio et al., 2016b). This impact has been reported in a previous study, indicating that the absorption of infrared radiation by CO_2 in smoke plumes could result in a 10%-20% underestimation of VIIRS FRP (Oliva and Schroeder, 2015). Indeed, the larger the fire events (clusters), the heavier the smoke, which results in much stronger impacts on VIIRS FRP retrievals. However, the effect of smoke on VIIRS FRP could be very complex, which is likely associated with smoke thickness and plume height, etc. This result suggests that VIIRS FRP estimation could be improved with the atmospheric correction in the 4-μm band, particularly for large fires.

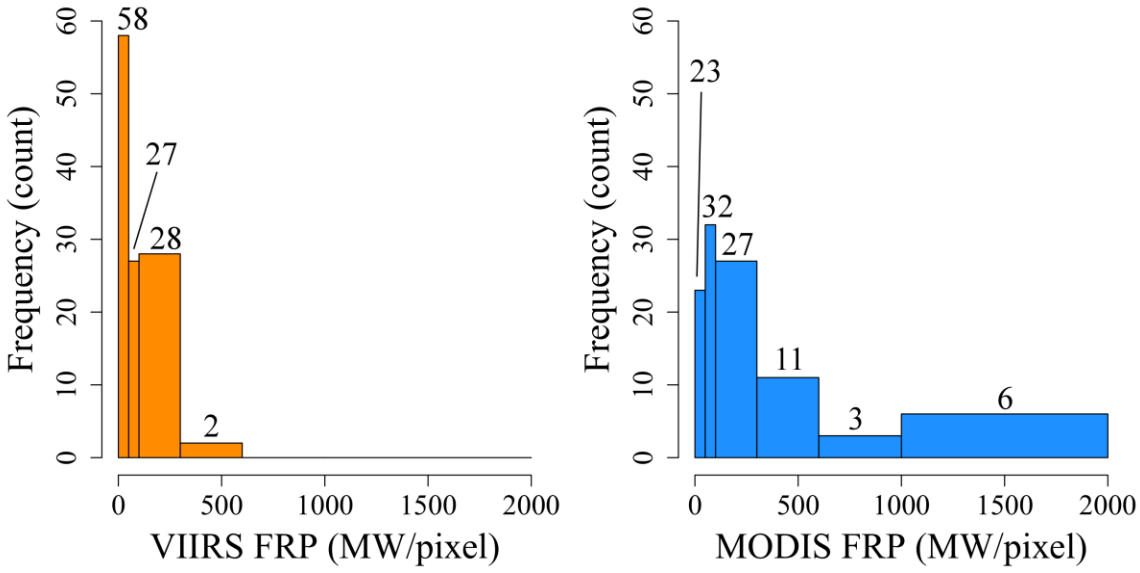

Figure 4-11. Distributions of the contemporaneous VIIRS and MODIS fire detections in fire clusters against FRP estimates in boreal forests (also see Figure 4-6e). The left panel shows VIIRS fire frequency varying with VIIRS FRP (per fire pixel) and the right panel is MODIS fire frequency in five FRP ranges: 0-50 MW, 51-100 MW, 101-300 MW, 301-600 MW, 601-1000 MW, and 1001-2000MW. Numbers on bars are the detection count in each range bin.

The temporal gap between the overpass time of VIIRS and MODIS, which spans from a few seconds to 50 min, has a twofold influence on their FRP difference. First, fire events, particularly small and fast spreading fires, could differ greatly during the period between the VIIRS and MODIS overpass times. This impact is demonstrated in agricultural fires in Punjab, India on 11 November 2016 (Figure 4-12), where the overpass time of Aqua MODIS was merely 15 min earlier than that of VIIRS. The large discrepancy between MODIS and VIIRS fire detections is likely because the burning

periods in individual agriculture fires are very short (Baucum et al., 2002). In other words, fires detected by one sensor could have gone out at the overpass of another sensor.

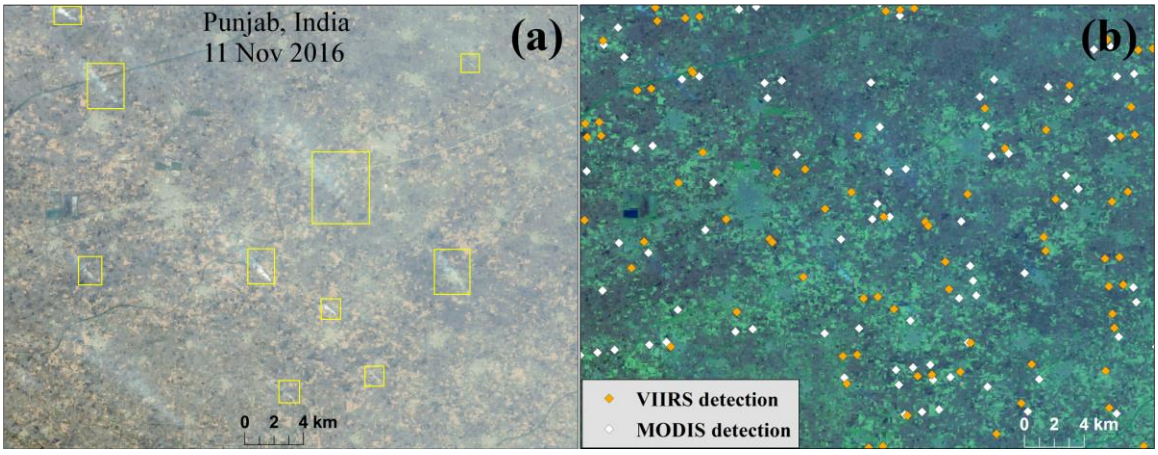

Figure 4-12. Active fire detections from MODIS and VIIRS in croplands of Punjab, India on 11 November 2016. MODIS and VIIRS flew over this area at 08:10 UTC and 08:25 UTC, respectively. (a) The false-color composite of Landsat 8 band 4 (red), band 3 (green), and band 2 (blue). Landsat 8 collected this data at 05:31 UTC. Smoke plumes (in white delineated by the yellow rectangles) from agricultural burning were spreading towards the upper-left direction. (b) Fire detections, for visualization purpose, were overlaid on the false-color composite image of Landsat 8 band 7 (red), band 5 (green), and band 3 (blue).

Second, during days when the temporal gaps are relatively long (e.g., > 20 min), the associated cloud variation is likely one of the sources that complicate the FRP relationship between MODIS and VIIRS fire detections, particular in some tropical regions. Such impacts of cloud cover have been demonstrated in previous research that shows approximately 11% of omission error in MODIS fire detections caused by cloud

obscuration in the Amazon basin compared to fire data from the Geostationary Operational Environmental Satellite (GOES) (Schroeder et al., 2008).

The continental-scale FRP comparison based on the contemporaneous fire detections sensed by MODIS and VIIRS is less likely affected by the overpass temporal gap. As a result, MODIS and VIIRS FRP estimates are very similar, although some slight differences exist. This discrepancy could be explained by the higher capability of VIIRS in detecting smaller and cooler fires than the MODIS sensor. For instance, the continental-scale VIIRS FRP estimates are overall larger than MODIS FRP in savanna fire dominated Africa (Figure 4-7d) and agriculture fire dominated Europe (Figure 4-7c). However, this advantage could be offset by the attenuation of VIIRS FRP by CO_2-rich smoke plumes in some large fire regions (e.g., Asia in Figure 4-7e).

At the global grid cells and latitude average, discrepancies between MODIS and VIIRS FRP estimates could be attributed to most above-discussed factors because all fire detections from MODIS and VIIRS during the period from April 2016 to March 2017 were used to calculate the VIIRS-to-MODIS FRP ratio. In addition to the factors mentioned above, the sensor's swath width (Table 4-1) also matters in low latitudes. In tropical regions, the grid-cell VIIRS FRP estimate is larger than MODIS FRP in most areas (e.g., Africa) (Figure 4-9), which could be mostly explained by the omission error of MODIS fire data due to spatial coverage gaps between adjacent orbits at low latitudes (30°S and 30°N, see Figure 4-1) (Wolfe et al., 2013). The MODIS omission error in the inter-orbital gaps has been demonstrated in fire detection (Cheng et al., 2013; Giglio et al., 2009) and emissions estimation (Wiedinmyer et al., 2011). Nevertheless, the larger MODIS FRP than VIIRS FRP in grid cells over South American tropical rainforests, as

shown in Figure 4-9b, suggests that a combination of multiple factors could have very complex impacts on the discrepancies between MODIS and VIIRS FRP estimates.

4.6. Conclusions

This study examined the capability of Aqua MODIS and Suomi NPP VIIRS sensors in fire detection and characterization along satellite view angles and investigated the relationship between MODIS FRP and VIIRS FRP estimates at different spatial scales. The results indicate that MODIS detection capability decreases as view angle increases from nadir to the scan edge, whereas VIIRS experiences a generally consistent detection capability from all view angles. As a result, FRP per detection across swath increases greatly in MODIS but only slightly in VIIRS retrievals. This is mainly due to the sensing geometry difference between the two sensors. FRP comparisons at fire clusters and continental to global scales revealed that the relationship between MODIS and VIIRS FRP retrievals varies across ecosystems and spatial scales. The FRP relationship in individual fire events shows that cluster FRP estimates are overall comparable in savannas, croplands, and tropical rainforests and broadleaf forests. However, VIIRS FRP is much smaller than MODIS FRP for large fires in boreal forests. The continental-scale FRP between contemporaneous MODIS and VIIRS fire detections is strongly correlated (Pearson's $r \geq 0.98$) in all six continents although VIIRS FRP is slightly larger. The grid-FRP difference between the two sensors is, on average, approximately 20% in most fire-prone regions, although it varies considerably in fire-limited regions. Generally, VIIRS FRP at grid cells is larger than MODIS FRP in savanna

and agricultural fires but is smaller in tropical rainforests in South America and especially in boreal forests in North America and Eurasia. Along latitudes, VIIRS FRP is, on average, approximately 16% larger than MODIS FRP in the tropical zone (30°S - 30°N) where over 88% of VIIRS and MODIS fires is mainly distributed. At mid-to-high latitudes, VIIRS FRP is mostly less than MODIS FRP, particularly in boreal forests (55°N-70°N). The larger VIIRS FRP estimates in small fires are generally attributed to the higher capability of detecting small and cool fires relative to MODIS estimates, whereas the lower VIIRS FRP in large and intensive fires, such as boreal forest fires, is likely associated with the attenuation of FRP by CO_2-rich smoke plumes associated with wider wavelength for VIIRS fire detections. Therefore, future work on atmospheric correction is expected to mitigate the underestimation of VIIRS FRP in these regions. In addition, inter-orbit gaps in MODIS observations at low latitudes could result in the underestimates of MODIS FRP.

The similarities of and discrepancies between MODIS and VIIRS FRP are associated with several other factors. VIIRS data have fewer duplicate fire detections than MODIS data. The FRP estimates from the inter-scan duplicate fire detections account for 18.3% overall in MODIS FRP, but 6.7% in VIIRS FRP. The inter-orbital duplicate detections exert very limited effects on FRP estimates, which is less than 1.3% of FRP. Moreover, the variations of cloudiness and small fires during the period between MODIS and VIIRS overpass times can also result in the discrepancy of FRP estimates.

In summary, the VIIRS sensor offers a good continuity to MODIS fire detections and FRP data record and provides a superior capability to detect smaller fires with no notable dependence on view zenith angle. Users integrating current VIIRS 750m active

fire product into current applications that use MODIS active fire products should pay attention to the advantages and shortcomings of VIIRS sensor (M-bands) and active fire product. In addition, applications could also consider the VIIRS 375m fire product (Schroeder et al., 2014), which is currently being evaluated for NOAA operational production. Finally, it should be noted that although the NOAA VIIRS NDEAF-L2 fire product provides timely or near real-time fire observations based on the operational VIIRS Sensor Data Records, the NASA VIIRS fire products are transitioning to use better calibrated (or reprocessed) upstream data (Schroeder and Giglio, 2017).

Acknowledgments

This research was funded by NOAA Contract No: NA14NES4320003 and BG-133E-15-SE-1613. The authors thank three anonymous reviewers for constructive comments. Thanks also go to Dr. Wilfrid Schroeder for discussions in particular on VIIRS FRP retrieval issues. The manuscript contents are solely the opinions of the author(s) and do not constitute a statement of policy, decision, or position on behalf of NOAA or the U. S. Government. The authors comply with AGU's data policy. The raw input datasets (Aqua MODIS C6 MYD14 and MYD03, and Suomi NPP VIIRS NDEAF-L2 and GMTCO) used in this study are available for the public at NASA’s Level-1 and Atmosphere Archive & Distribution System (LAADS) (https://ladsweb.modaps.eosdis.nasa.gov/) and the NOAA Comprehensive Large Array-Data Stewardship System (CLASS) (https://www.class.ncdc.noaa.gov/). The output data sets of this study are accessible at

the institutional repository of South Dakota State University (https://openprairie.sdstate.edu/global_land_surface_season_data/2/).

References

Archibald, S., C. E. R. Lehmann, J. L. Gómez-Dans, and R. A. Bradstock (2013), Defining pyromes and global syndromes of fire regimes, Proceedings of the National Academy of Sciences, 110(16), 6442-6447, doi: https://doi.org/10.1073/pnas.1211466110.

Baucum, L., R. Rice, and T. Schueneman (2002), An overview of Florida sugarcane, Agronomy Department, Florida Cooperative Extension Service, Institute of Food and Agricultural Sciences, University of Florida. Publication# SS-AGR-232, Available: http://hendry.ifas.ufl.edu/pdfs/overview_of_florida_sugarcane.pdf, last access on 08/07/2017.

Boersma, K. F., D. J. Jacob, M. Trainic, Y. Rudich, I. DeSmedt, R. Dirksen, and H. J. Eskes (2009), Validation of urban NO2 concentrations and their diurnal and seasonal variations observed from the SCIAMACHY and OMI sensors using in situ surface measurements in Israeli cities, Atmos. Chem. Phys., 9(12), 3867-3879, doi: https://doi.org/10.5194/acp-9-3867-2009.

Cao, C., F. J. D. Luccia, X. Xiong, R. Wolfe, and F. Weng (2014), Early On-Orbit Performance of the Visible Infrared Imaging Radiometer Suite Onboard the Suomi National Polar-Orbiting Partnership (S-NPP) Satellite, IEEE Transactions on

Geoscience and Remote Sensing, 52(2), 1142-1156, doi: https://doi.org/10.1109/TGRS.2013.2247768.

Cheng, D., J. Rogan, L. Schneider, and M. Cochrane (2013), Evaluating MODIS active fire products in subtropical Yucatán forest, Remote Sensing Letters, 4(5), 455-464, doi: https://doi.org/10.1080/2150704X.2012.749360.

Cohen, W. B., T. K. Maiersperger, S. T. Gower, and D. P. Turner (2003), An improved strategy for regression of biophysical variables and Landsat ETM+ data, Remote Sensing of Environment, 84(4), 561-571, doi: https://doi.org/10.1016/S0034-4257(02)00173-6.

Csiszar, I., W. Schroeder, L. Giglio, E. Ellicott, K. P. Vadrevu, C. O. Justice, and B. Wind (2014), Active fires from the Suomi NPP Visible Infrared Imaging Radiometer Suite: Product status and first evaluation results, Journal of Geophysical Research: Atmospheres, 119(2), 2013JD020453, doi: https://doi.org/10.1002/2013JD020453.

Csiszar, I., W. Schroeder, L. Giglio, V. Mikles, and M. Tsidulko (2016), The NOAA NDE Active Fire EDR External Users Manual. Available: https://www.star.nesdis.noaa.gov/jpss/documents/UserGuides/VIIRS_ActiveFire_EUM.pdf, last accessed on 1/20/2018.

Darmenov, A. S., and A. d. Silva (2015), The Quick Fire Emissions Dataset (QFED): Documentation of versions 2.1, 2.2 and 2.4 Rep. TM–2015–104606, 212 pp, NASA, Goddard Space Flight Center Greenbelt, MD.

Ellicott, E., E. Vermote, L. Giglio, and G. Roberts (2009), Estimating biomass consumed from fire using MODIS FRE, Geophysical Research Letters, 36(13), L13401, doi: https://doi.org/10.1029/2009GL038581.

Flannigan, M. D., and T. H. V. Haar (1986), Forest fire monitoring using NOAA satellite AVHRR, Canadian Journal of Forest Research, 16(5), 975-982, doi: https://doi.org/10.1139/x86-171.

Freeborn, P. H., W. M. Jolly, and M. A. Cochrane (2016), Impacts of changing fire weather conditions on reconstructed trends in U.S. wildland fire activity from 1979 to 2014, Journal of Geophysical Research: Biogeosciences, 2016JG003617, doi: https://doi.org/10.1002/2016JG003617.

Freeborn, P. H., M. J. Wooster, G. Roberts, B. D. Malamud, and W. Xu (2009), Development of a virtual active fire product for Africa through a synthesis of geostationary and polar orbiting satellite data, Remote Sensing of Environment, 113(8), 1700-1711, doi: https://doi.org/10.1016/j.rse.2009.03.013.

Freeborn, P. H., M. J. Wooster, D. P. Roy, and M. A. Cochrane (2014), Quantification of MODIS fire radiative power (FRP) measurement uncertainty for use in satellite-based active fire characterization and biomass burning estimation, Geophysical Research Letters, 41(6), 2013GL059086, doi: https://doi.org/10.1002/2013GL059086.

Friedl, M. A., D. Sulla-Menashe, B. Tan, A. Schneider, N. Ramankutty, A. Sibley, and X. Huang (2010), MODIS Collection 5 global land cover: Algorithm refinements and characterization of new datasets, Remote Sensing of Environment, 114(1), 168-182, doi: https://doi.org/10.1016/j.rse.2009.08.016.

Giglio, L., I. Csiszar, and C. O. Justice (2006), Global distribution and seasonality of active fires as observed with the Terra and Aqua Moderate Resolution Imaging Spectroradiometer (MODIS) sensors, Journal of Geophysical Research: Biogeosciences, 111(G2), G02016, doi: https://doi.org/10.1029/2005JG000142.

Giglio, L., J. Descloitres, C. O. Justice, and Y. J. Kaufman (2003), An Enhanced Contextual Fire Detection Algorithm for MODIS, Remote Sensing of Environment, 87(2–3), 273-282, doi: https://doi.org/10.1016/S0034-4257(03)00184-6.

Giglio, L., T. Loboda, D. P. Roy, B. Quayle, and C. O. Justice (2009), An active-fire based burned area mapping algorithm for the MODIS sensor, Remote Sensing of Environment, 113(2), 408-420, doi: https://doi.org/10.1016/j.rse.2008.10.006.

Giglio, L., W. Schroeder, and C. O. Justice (2016a), The collection 6 MODIS active fire detection algorithm and fire products, Remote Sensing of Environment, 178, 31-41, doi: https://doi.org/10.1016/j.rse.2016.02.054.

Giglio, L., W. Schroeder, I. Csiszar, and M. Tsidulko (2016b), Algorithm Theoretical Basis Document For NOAA NDE VIIRS Active Fire. Available: https://www.star.nesdis.noaa.gov/jpss/documents/ATBD/ATBD_NDE_AF_v2.6.pdf, last accessed on 6/2/2017.

Goldberg, M. D., H. Kilcoyne, H. Cikanek, and A. Mehta (2013), Joint Polar Satellite System: The United States next generation civilian polar-orbiting environmental satellite system, Journal of Geophysical Research: Atmospheres, 118(24), 13,463-413,475, doi: https://doi.org/10.1002/2013JD020389.

Ichoku, C., L. Giglio, M. J. Wooster, and L. A. Remer (2008), Global characterization of biomass-burning patterns using satellite measurements of fire radiative energy, Remote Sensing of Environment, 112(6), 2950-2962, doi: https://doi.org/10.1016/j.rse.2008.02.009.

Ichoku, C., L. T. Ellison, K. E. Willmot, T. Matsui, A. K. Dezfuli, C. K. Gatebe, J. Wang, E. M. Wilcox, J. Lee, and J. Adegoke (2016), Biomass burning, land-cover change, and the hydrological cycle in Northern sub-Saharan Africa, Environmental Research Letters, 11(9), 095005, https://doi.org/10.1088/1748-9326/11/9/095005.

Ichoku, C., and Y. J. Kaufman (2005), A method to derive smoke emission rates from MODIS fire radiative energy measurements, Geoscience and Remote Sensing, IEEE Transactions on, 43(11), 2636-2649, doi: https://doi.org/10.1109/TGRS.2005.857328.

Kaiser, J. W., A. Heil, M. O. Andreae, A. Benedetti, N. Chubarova, L. Jones, J. J. Morcrette, M. Razinger, M. G. Schultz, M. Suttie, and G. R. van der Werf (2012), Biomass burning emissions estimated with a global fire assimilation system based on observed fire radiative power, Biogeosciences, 9(1), 527-554, doi: https://doi.org/10.5194/bg-9-527-2012.

Kaufman, Y. J., C. O. Justice, L. P. Flynn, J. D. Kendall, E. M. Prins, L. Giglio, D. E. Ward, W. P. Menzel, and A. W. Setzer (1998), Potential global fire monitoring from EOS-MODIS, Journal of Geophysical Research: Atmospheres, 103(D24), 32215-32238, doi: https://doi.org/10.1029/98JD01644.

Kumar, S. S., D. P. Roy, L. Boschetti, and R. Kremens (2011), Exploiting the power law distribution properties of satellite fire radiative power retrievals: A method to

estimate fire radiative energy and biomass burned from sparse satellite observations, Journal of Geophysical Research: Atmospheres, 116(D19), D19303, doi: https://doi.org/10.1029/2011JD015676.

Oliva, P., and W. Schroeder (2015), Atmospheric correction of VIIRS and MODIS fire radiative power retrievals for multi-sensor comparison, paper presented at 2015 IEEE International Geoscience and Remote Sensing Symposium (IGARSS), 26-31 July 2015.

Peterson, D., J. Wang, C. Ichoku, E. Hyer, and V. Ambrosia (2013), A sub-pixel-based calculation of fire radiative power from MODIS observations: 1: Algorithm development and initial assessment, Remote Sensing of Environment, 129(0), 262-279, doi: https://doi.org/10.1016/j.rse.2012.10.036.

Prins, E. M., and W. P. Menzel (1992), Geostationary satellite detection of biomass burning in South America, International Journal of Remote Sensing, 13(15), 2783-2799, doi: https://doi.org/10.1080/01431169208904081.

Roberts, G. J., and M. J. Wooster (2008), Fire Detection and Fire Characterization Over Africa Using Meteosat SEVIRI, Geoscience and Remote Sensing, IEEE Transactions on, 46(4), 1200-1218, doi: https://doi.org/10.1109/TGRS.2008.915751.

Roberts, G., M. J. Wooster, W. Xu, P. H. Freeborn, J. J. Morcrette, L. Jones, A. Benedetti, H. Jiangping, D. Fisher, and J. W. Kaiser (2015), LSA SAF Meteosat FRP products – Part 2: Evaluation and demonstration for use in the Copernicus Atmosphere Monitoring Service (CAMS), Atmos. Chem. Phys., 15(22), 13241-13267, doi: https://doi.org/10.5194/acp-15-13241-2015.

Roy, D. P., and S. S. Kumar (2017), Multi-year MODIS active fire type classification over the Brazilian Tropical Moist Forest Biome, International Journal of Digital Earth, 10(1), 54-84, doi: https://doi.org/10.1080/17538947.2016.1208686.

Schroeder, W. and L. Giglio, 2017, Visible Infrared Imaging Radiometer Suite (VIIRS) 750 m Active Fire Detection and Characterization Algorithm Theoretical Basis Document 1.0. Available: https://viirsland.gsfc.nasa.gov/PDF/VIIRS_activefire_ATBD750_v1.pdf, last accessed on 1/20/2018.

Schroeder, W., I. Csiszar, and J. Morisette (2008), Quantifying the impact of cloud obscuration on remote sensing of active fires in the Brazilian Amazon, Remote Sensing of Environment, 112(2), 456-470, doi: https://doi.org/10.1016/j.rse.2007.05.004.

Schroeder, W., P. Oliva, L. Giglio, and I. A. Csiszar (2014), The New VIIRS 375 m active fire detection data product: Algorithm description and initial assessment, Remote Sensing of Environment, 143, 85-96, doi: https://doi.org/10.1016/j.rse.2013.12.008.

Smith, A. M. S., and M. J. Wooster (2005), Remote classification of head and backfire types from MODIS fire radiative power and smoke plume observations, International Journal of Wildland Fire, 14(3), 249-254, doi: https://doi.org/10.1071/WF05012.

Smith, R. J. (2009), Use and misuse of the reduced major axis for line-fitting, American Journal of Physical Anthropology, 140(3), 476-486, doi: https://doi.org/10.1002/ajpa.21090.

Vermote, E., E. Ellicott, O. Dubovik, T. Lapyonok, M. Chin, L. Giglio, and G. J. Roberts (2009), An approach to estimate global biomass burning emissions of organic and black carbon from MODIS fire radiative power, Journal of Geophysical Research: Atmospheres, 114(D18), D18205, doi: https://doi.org/10.1029/2008JD011188.

White, M. A., K. M. De Beurs, K. Didan, D. W. Inouye, A. D. Richardson, O. P. Jensen, J. O'Keefe, G. Zhang, R. R. Nemani, W. J. D. Van Leeuwen, J. F. Brown, A. De Wit, M. Schaepman, X. Lin, M. Dettinger, A. S. Bailey, J. Kimball, M. D. Schwartz, D. D. Baldocchi, J. T. Lee, and W. K. Lauenroth (2009), Intercomparison, interpretation, and assessment of spring phenology in North America estimated from remote sensing for 1982–2006, Global Change Biology, 15(10), 2335-2359, doi: https://doi.org/10.1111/j.1365-2486.2009.01910.x.

Wiedinmyer, C., S. K. Akagi, R. J. Yokelson, L. K. Emmons, J. A. Al-Saadi, J. J. Orlando, and A. J. Soja (2011), The Fire INventory from NCAR (FINN): a high resolution global model to estimate the emissions from open burning, Geosci. Model Dev., 4(3), 625-641, doi: https://doi.org/10.5194/gmd-4-625-2011.

Wolfe, R. E., G. Lin, M. Nishihama, K. P. Tewari, J. C. Tilton, and A. R. Isaacman (2013), Suomi NPP VIIRS prelaunch and on-orbit geometric calibration and characterization, Journal of Geophysical Research: Atmospheres, 118(20), 2013JD020508, doi: https://doi.org/10.1002/jgrd.50873.

Wolfe, R. E., M. Nishihama, A. J. Fleig, J. A. Kuyper, D. P. Roy, J. C. Storey, and F. S. Patt (2002), Achieving sub-pixel geolocation accuracy in support of MODIS land

science, Remote Sensing of Environment, 83(1–2), 31-49, doi: https://doi.org/10.1016/S0034-4257(02)00085-8.

Wolfe, R. E., D. P. Roy, and E. Vermote (1998), MODIS land data storage, gridding, and compositing methodology: Level 2 grid, Geoscience and Remote Sensing, IEEE Transactions on, 36(4), 1324-1338, doi: https://doi.org/10.1109/36.701082.

Wooster, M. J., and Y. H. Zhang (2004), Boreal forest fires burn less intensely in Russia than in North America, Geophysical Research Letters, 31(20), L20505, doi: https://doi.org/10.1029/2004GL020805.

Wooster, M. J., B. Zhukov, and D. Oertel (2003), Fire radiative energy for quantitative study of biomass burning: derivation from the BIRD experimental satellite and comparison to MODIS fire products, Remote Sensing of Environment, 86(1), 83-107, doi: https://doi.org/10.1016/S0034-4257(03)00070-1.

Wooster, M. J., G. Roberts, P. H. Freeborn, W. Xu, Y. Govaerts, R. Beeby, J. He, A. Lattanzio, D. Fisher, and R. Mullen (2015), LSA SAF Meteosat FRP products – Part 1: Algorithms, product contents, and analysis, Atmos. Chem. Phys., 15(22), 13217-13239, doi: https://doi.org/10.5194/acp-15-13217-2015.

Zhang, X., S. Kondragunta, A. Da Silva, S. Lu, H. Kim, H. Ding, Y. Zhu, and Z. Cheng (2014), Algorithm Theoretical Basis Document For NOAA GBBEPx Emissions Product, Version 1.1, edited, NOAA/NESDIS/STAR. Available: http://www.ospo.noaa.gov/Products/land/gbbepx/docs/GBBEPx_ATBD.pdf, last accessed on 1/8/2018.

Zhang, X., S. Kondragunta, J. Ram, C. Schmidt, and H.-C. Huang (2012), Near-real-time global biomass burning emissions product from geostationary satellite constellation, Journal of Geophysical Research-Atmospheres, 117(D14), D14201, doi: https://doi.org/10.1029/2012jd017459.

CHAPTER 5: Summary of the Research

As presented in Chapter 1, this research aimed to enhance to the capability of the FRP-based method for estimating BBE. To pursue this aim, this research set three objectives, which were addressed by testing three hypotheses, respectively. This Chapter summarizes the key findings and discusses the potential research directions in future.

5.1. Hypothesis #1

Satellite retrieved FRE estimates are linearly related to the biomass consumption at landscape scales with a factor of FRE biomass combustion coefficient (FBCC).

5.1.1. Summary of the Methods

The factor FBCC was derived by statistically comparing biomass consumption based on Landsat burned area with GOES and MODIS FRE estimates over 445 wildfires across the CONUS. First, to ensure the well observation of fires by the GOES and MODIS sensors, a total of 445 wildfires were selected by spatially and temporally matching MTBS Landsat burned areas with GOES and MODIS active fire detections. Then, for each selected wildfire, the biomass consumption was estimated using the conventional method that integrates burned area based on MTBS Landsat burn severity, FCCS fuel loading, and combustion completeness (CC) parameterized by burn severity; and GOES and MODIS FRE were estimated using the methods proposed by Zhang et al. (2012) and Boschetti and Roy. (2009), respectively. Finally, by assuming that the Landsat-burned-area-based biomass consumption is approximately equal to the FRE-based biomass consumption over each well-observed fire, the FBCC was derived using a simple linear regression with GOES FRE or MODIS FRE as the independent variable and the Landsat-burned-area-based biomass consumption as the dependent variable. In

addition, to examine the sensitivity of FBCC to the Landsat-burned-area-based biomass consumption, the biomass consumption was also estimated using the conventional method in two different ways: (1) using a constant of CC=0.5 by assuming that all fuels were consumed by 50%, and (2) using the Land-cover-based method endorsed by IPCC for estimating national emissions (IPCC, 2006).

5.1.2. Results and Conclusions

Hypothesis #1 was confirmed. Over the 455 wildfires across the CONUS, the estimates of biomass consumption based on Landsat burned area are linearly related to both GOES and MODIS FRE estimates. The results show that FBCC is 0.374 kg · MJ^{-1} for GOES FRE, 0.266 kg · MJ^{-1} for MODIS FRE, and 0.320 kg · MJ^{-1} considering both GOES and MODIS FRE. Over the same fires, sensitivity analyses of FBCC to combustion completeness and fuel consumption suggests that FBCC varies from 0.301 to 0.458 kg · MJ^{-1}. Overall, the FBCC values reported in this study were close to those FBCC values derived in controlled fire experiments (Wooster et al., 2005; Freeborn et al., 2008).

5.1.3. Implications and Future Work

The derived CONUS FBCC values in this study may be applicable to estimate BBE in other regions. Among the 455 wildfires that used to derive the CONUS FBCC, the majority of them occurred in forests, especially the forests in the Western CONUS, and the remaining small portion occurred in shrubland and grassland. Thus, the CONUS FBCC could be applied to estimate BBE using GOES and MODIS FRE in regions where fire activity is similar to that in the Western CONUS. To evaluate this, independent studies are needed. As the reported FBCC values are mainly limited to forests in the

CONUS, future work is needed to investigate the FBCC in other ecosystems in different fire-prone regions.

The derived CONUS FBCC values are affected by uncertainties in combustion completeness, fuel loads, and satellite FRE estimates that need to be addressed in future work. Although the FBCC based on the burn severity parametrized CC only differ slightly from the FBCC derived using a fixed CC, it is likely that CC values summarized from limited studies (Table 2-1 in Chapter 2) may not well represent the real CC values over the 455 wildfires. This is because wildfire CC is spatially explicit and is very difficult to estimate (Veraverbeke & Hook, 2013). Furthermore, although the best available fuel data, the FCCS fuel, in the CONUS is used, it is not able to characterize fuel dynamics. The challenge of estimating fuel consumption may be mitigated by advances in remote sensing technology, i.e., LiDAR. The LiDAR data from the airborne- and ground-based platforms have shown large potential in mapping vegetation structure and measuring fuel loads (Hudak et al., 2016; Lefsky et al., 2002). In the CONUS, a solution of applying LiDAR data to estimate fuel has been proposed by the LANDFIRE project (Peterson et al., 2015). In addition, the reported FBCC does show variation with FRE estimates from the MODIS and GOES sensors. Because of the improved capability of detecting fires, the advanced sensors (i.e., GOES-R series and VIIRS) will provide more accurate FRE estimates than the current GOES and MODIS sensors (Csiszar et al., 2014; Schmit et al., 2017). The potential advantages of VIIRS for improving FRP and FRE and thus BBE estimates over MODIS have been demonstrated in the third hypothesis (See hypothesis #3). Thus, studies are needed to investigate the FBCC using the accuracy-improved FRE.

5.2. Hypothesis #2

Diurnal FRP cycles can be reconstructed from the polar-orbiting and geostationary satellites FRP retrievals to improve emissions estimation.

5.2.1. Summary of the Methods

Diurnal FRP cycles were reconstructed by fusing GOES and MODIS FRP retrievals, and the reconstructed diurnal FRP cycles were further applied to estimate BBE in the CONUS. First, GOES FRP retrievals were calibrated against MODIS FRP to mitigate underestimate in GOES FRP. The calibration coefficients were derived for five land cover types (including forest, shrubs, savannas, grassland, and cropland) by comparing contemporaneous GOES and MODIS FRP over 628 fires across the CONUS. Second, the calibrated GOES FRP were fused with MODIS FRP to provide FRP in every 15min. Third, to predict FRP in the temporal gaps without observations due to sensor saturation or clouds obscurations, diurnal FRP climatology was derived for all 45 ecosystems in the CONUS using calibrated GOES FRP; and it was further applied to fit the fused FRP. A reconstructed diurnal FRP cycle consists of the fused and predicted FRP. Fourth, the reconstructed diurnal FRP cycles were used to estimate hourly BBE (i.e., PM2.5 and CO) at a 0.25°×0.3125° grid cell across the CONUS for the period from 2011 to 2015. The BBE estimates were evaluated in three ways by comparing with: (1) BBE based on Landsat burned area over 60 wildfires, (2) BBE from eight regional and global emissions inventories, and (3) BBE simulated by the WRF-Chem model over the Rim Fire in California, 2013. These BBE comparisons were used for the indirect evaluation of the applicability of the reconstructed diurnal FRP cycles.

5.2.2. Results and Conclusions

Hypothesis #2 was partially confirmed. Diurnal FRP cycles for the CONUS fire activity were reconstructed from the FRP estimates that were produced by fusing MODIS and GOES (11, 13, & 15) FRP retrievals at a 0.25°×0.3125° grid cell for the period from 2011 to 2015. The climatologic diurnal FRP cycle varies significantly in shape and magnitude among the 45 CONUS ecosystems. The mean annual BBE estimated using the reconstructed diurnal FRP cycles is approximately 690 Gg across the CONUS. For individual fire events in the Western CONUS, the estimated emissions compared well with the estimates based on the Landsat burned area, and with the hourly CO emissions that were simulated using the WRF-Chem model. In addition, the seasonal variation of the estimated PM2.5 emissions shows good agreement with that of existing emissions inventories, and the magnitude values are reasonable compared to existing inventories.

5.2.3. Implications and Future Work

The proposed method for reconstruction of diurnal FRP cycles in the CONUS is applicable in other regions in low-middle latitudes where geostationary satellite FRP retrievals are available. Studies have shown that the diurnal FRP cycle from only geostationary satellites leads to underestimation of BBE (Zhang et al., 2012). Thus, integrating higher spatial-resolution FRP from the polar-orbiting satellite into diurnal FRP cycle potentially improves the estimation of BBE. This method could be applied to improve diurnal FRP reconstruction and BBE estimates using FRP retrievals from the advanced VIIRS sensor (Csiszar et al., 2014) and geostationary sensors of SEVIRI (Wooster et al., 2015) for Africa, Himawari 9 (Xu et al., 2017) for Asia, and latest

generation of GOES (i.e., GOES-R series) (Schmidt et al., 2012) for South and North Americas.

Three main challenges in the estimation of BBE need to be addressed in future work. First, it is difficult to determine the consistent burning duration of fires using satellite observations for the purpose of reconstruction of diurnal FRP cycles. Based on the diurnal and seasonal distributions of GOES fire detections, this study applied the same assumptions of burning durations to all fire types (Section 3.2.5.2 in Chapter 3). These assumptions may result in moderate uncertainty in FRE and BBE estimates. For example, in most cases, GOES has very temporally sparse detections of low-intensity fires (e.g., agricultural and prescribed burnings), which may only last from less than an hour to a few hours (Baucum et al., 2002). Assumption of a consistent burning period of one hour before and after a GOES fire observation in the early afternoon could result in overestimate of FRE and BBE. Therefore, integration of the field-based data of burning duration will help to deal with this challenge.

Second, datasets and/or methods for validating BBE are greatly needed. Many efforts, including this study, have been put to estimate BBE and develop operational BBE products. However, very large discrepancies exist among BBE products. For instance, the long-term GFED data estimates annual global carbon emissions of 2.2 Pg (van der Werf et al., 2017), approximately 23% annual global carbon emissions from burning fossil fuels in 2014 (Boden et al., 2017), whereas the NASA's QFED products tripled the estimates of GFED emissions (Darmenov & Silva, 2015), approximately 60% of the fossil-fuel carbon emissions. Both datasets have been widely used as the smoke emissions input in chemical transport models (i.e., GEOS-CHEM) (Kim et al., 2015;

Eastham & Jacob, 2017). To evaluate the accuracy of BBE, the common practice is to simulate AOD using BBE estimates and compare it with the observed AOD. However, the models that simulate AOD require many parameters (i.e., weather data), which are often oversimplified and thus have large uncertainty (Ichoku & Ellison, 2014; Zhang et al., 2014). Therefore, independent validation datasets are greatly needed. Although a few satellites, i.e., NASA's Orbiting Carbon Observatory-2 (OCO-2) and Terra Measurements of Pollution In The Troposphere (MOPITT), provide direct measurements of Carbon emissions (i.e., CO_2 and CO), these emissions retrievals are either only sensitive to very large fires (Heymann et al., 2016) or impaired by thick smoke plumes (Deeter et al., 2016). Therefore, new special sensors for smoke emissions from fires are needed.

Last but not the least, there is a big gap between the emissions community and the application community. The emissions community, for the application purpose, tries to estimate BBE as accurately as possible. On the other hand, the application models take BBE as input to forecast air quality and assess the impact of smoke aerosols on numerical weather prediction (Reid et al., 2009). However, the application community provides very limited feedbacks to the emissions community, at least in the published literatures. Specific feedbacks are very important for the emissions community to target and fix issues in estimation of BBE.

5.3. Hypothesis #3

The 750-m VIIRS sensor has better capability of characterizing fires than the 1-km MODIS sensor.

5.3.1. Summary of the Methods

FRP retrievals from the 750-m VIIRS and 1-km MODIS sensors were compared to investigate the similarities and discrepancies between their capabilities of characterizing fire. First, the VIIRS and MODIS level-2 active fire products were preprocessed to correct the inter-scan and inter-orbital fire detection duplicates. Then, VIIRS and MODIS FRP were compared in four ways using: (1) contemporaneous (minimal, mean, maximal, and sum) FRP in different satellite view zenith angles across the swath; (2) FRP for 619 contemporaneous fire clusters over global 13 regions of savannas, tropical rainforest, boreal forests, broadleaf forest, and croplands; (3) contemporaneous FRP at continental scale; (4) FRP at global 1°×1° grid cells and along latitude variation using all detections (including contemporaneous and not contemporaneous detections).

5.3.2. Results and Conclusions

Hypothesis #3 was confirmed partially. The VIIRS sensor is able to detect many more small and cool fires than MODIS sensor, as expected theoretically. First, the minimal FRP (per pixel) of VIIRS is much less dependent on satellite view angles than that of MODIS. Second, for the low-intensity agricultural burnings and savanna grass fires, VIIRS FRP is overall larger than MODIS FRP for contemporaneous fire detections at continental scale and for all fire detections at a 1°×1° grid cell. For the contemporaneously detected individual fire events of different intensities, VIIRS and MODIS FRP estimates are generally comparable. However, VIIRS FRP is smaller than MODIS FRP in a few regions that were blanked out by thick smoke, i.e., Siberia boreal forest and the transition zone from savannas to rainforests in South America. This is

mainly due to the overlapping of the VIIRS 4-μm M-band with a significant CO_2 absorption window, which results in the attenuation of VIIRS FRP by the smoke CO_2. In summary, the VIIRS sensor does perform better than MODIS in characterizing low-intensity fires, but thick smoke plume affects VIIRS FRP retrievals.

5.3.3. Implications and Future Work

VIIRS 750m active fire data benefits the BBE science community in several aspects. First, advanced capability of characterizing fires will significantly improve the estimation of BBE. Being able to detect more small and cool fires, VIIRS active fire product potentially reduce underestimation of BBE in tropical savanna fires-the largest source of global BBE (van der Werf et al., 2010), and agricultural fires in which BBE is of large uncertainty due to detection capabilities of current sensors (Giglio et al., 2009; Roy et al., 2008). Nevertheless, VIIRS FRP is overall smaller than MODIS FRP for nighttime fires that do not burn intensely in most cases due to lower temperature and higher humidity compared to daytime burnings. This may be due to the slight difference between the fire detection algorithms of the two sensors and is expected to be fixed by a future improved algorithm.

Second, the VIIRS sensor has better coverage of low-latitude areas than MODIS. At low latitudes, VIIRS has a full coverage every day (Wolfe et al., 2013), whereas MODIS takes two days to cover all areas (Wolfe et al., 1998). The missed fire observations in the daily gaps between MODIS swaths at low latitudes obviously affect BBE estimates, which has been observed (Wiedinmyer et al., 2011) but is not quantitatively known yet. Wang et al. (2018) tried to correct BBE bias caused by MODIS swath gaps in a very empirical way based on two-day MODIS fire detections. However, a

better way is to apply the contemporaneous VIIRS observations to predict missed observations by MODIS, which is very meaningful for correcting the MODIS gap-induced BBE bias in the past almost two decades.

Third, the VIIRS active fire data provides a good continuity to MODIS fire records. The long-term fire data is essential to understand the role of biomass burning in climate change and atmosphere dynamics. However, thick smoke plum affects the VIIRS FRP retrievals. Thus, efforts on atmospheric correction of VIIRS FRP are needed to mitigate the effect of smoke plumes.

5.4. A brief summary of the three hypotheses

The three hypotheses tested in this research address the parameters of FBCC and FRE in the FRP-based method to improve BBE estimation. First, hypothesis #1 investigates the FBCC at landscape scale in CONUS wildfires using surface biomass consumption based on Landsat burned area and GOES and MODIS FRE estimates. The results further confirm the empirical relationship that biomass consumption is a linear function of FRE. The derived FBCC has a similar range to the reported FBCC in the controlled small fire experiments, although the derived FBCC value in landscape-scale wildfires varies with GOES and MODIS FRE and with biomass consumption estimated in different parameterizations

Second, hypothesis #2 attempts to improve accuracy of FRE estimates through reconstructing diurnal FRP cycles (or high-spatiotemporal-resolution FRP) by fusing MODIS and GOES FRP retrievals. The BBE estimates based on the reconstructed diurnal

FRP cycles match well with the Landsat-burned-area-based and the model-simulated BBE, as well as BBE from some emissions inventories. This suggests that reconstruction of diurnal FRP cycles by fusing polar-orbiting and geostationary satellite FRP retrievals is a promising way to improve FRE and BBE estimates.

Third, hypothesis #3 investigates the potential improvement of VIIRS FRP and FRE estimates by examining the similarities and discrepancies between FRP retrievals from 1-km MODIS and the follow-on 750-m VIIRS. The results indicate that VIIRS and MODIS FRP are generally comparable over most contemporaneously detected fire clusters and for contemporaneous fire detections at continental scale as well. However, the continental-scale VIIRS FRP is larger than MODIS FRP in Europe and Africa dominated by low-intensity agricultural and savanna grass fires. Considering all annual fire detections, VIIRS FRP is ~20% larger than MODIS FRP in most fire-prone regions except boreal forest areas where VIIRS FRP is generally smaller than MODIS FRP. Therefore, FRP from the VIIRS sensor potentially improve FRE and BBE estimates.

In summary, this research confirms the linear relationship between biomass consumption and FRE at landscape scale, provides FBCC values for MODIS and GOES FRE, develops a method to simulate high-spatiotemporal-resolution FRP, generates hourly BBE emissions (i.e., PM2.5 and CO) at a 0.25°×0.3125° grid across the CONUS from 2011 to 2015, and investigates the potential of VIIRS FRP for improving FRE and BBE estimates. The developed methods could be used to improve the estimates of regional-to-global BBE which could be used as input of air quality forecast models.

5.5. Recommendations for Future Research

This part gives a vision of future research directions on biomass-burning emission. Based on the discussions of demanding future work in the above three hypotheses (See Sections 5.1.3, 5.2.3, and 5.3.3), I recommend the following three main directions for future research work.

First, observations of the fire and smoke-aerosol dedicated sensors hold large potentials to estimate and evaluate of BBE. The new generation of geostationary satellites (i.e., Himawari-9 and GOES16) observe fires every 5-10 min with a spatial resolution of 2 km (Schmit et al., 2017; Xu et al., 2017), which provides very good opportunities to understand the diurnal cycle of fire activity. Thus, integration of FRP from these new geostationary satellites and the advanced polar-orbiting satellites (i.e., VIIRS) could largely improves BBE estimation. Furthermore, the TROPOspheric Monitoring Instrument (TROPOMI) on board the Sentinel-5 Precursor satellite launched on 13 October 2017 provides daily global observations of aerosols and carbon monoxide (CO) at a spatial resolution of 7 km (the highest resolution for CO observation to date) (Borsdorff et al., 2018), which could be used as a good-quality dataset for evaluating BBE estimates at a variety of spatial scales. Besides the TROPOMI instrument, a similar sensor is also planned for the Sentinel-5 mission starting from 2021 (Ingmann et al., 2012).

Second, validation of BBE at landscape scales is urgently needed. As discussed in Section 5.2.3, very large discrepancies existing between BBE products raise large uncertainties in BBE applications (i.e., air quality forecast). This is primarily due to the lack of good-quality datasets for validating BBE estimates. The advancements of remote

sensing technology make it possible to validate BBE at landscape scale. For example, the LiDAR data from the airborne- and ground-based platforms has shown large potential in measuring landscape-scale fuel loads (Hudak et al., 2016; Lefsky et al., 2002). Thus, fuel consumption can be obtained by measuring pre-fire and post-fire fuel loads using LiDAR even for wildfires if field campaigns are well planned during fire season. Integration of airborne- and ground-based LiDAR data with high-spatial-resolution burned area based on Landsat8 and Sentinel-2A data provides a promising way to validate BBE at landscape scales.

Third, BBE contribution from small fires could be substantial, yet has not been well quantitatively understood. Small fires often occurring in agriculture-related regions generally burn for short time periods in small-size areas with low intensity, which makes satellite sensors difficult to detect (Giglio et al., 2016) and map the burned areas (Giglio et al., 2009; Hawbaker et al., 2017; Huang et al., 2018; Roy et al., 2008). Small fires may contribute a substantial portion of annual regional and global BBE estimates (McCarty, 2011; Randerson et al., 2012), and some important areas (e.g., Southeastern United States) have not been well targeted (Randerson et al., 2012). Combination of fire detections from new sensors, like VIIRS, Landsat-8 OLI, and Sentinel-2 (2A & 2B) for instance, may help to detect small fires. For example, the 375-m VIIRS I band has shown large potential in detecting agricultural fires (Zhang et al., 2017); yet it still misses a significant number of small fires compared to 30-m Landsat-8 fire detections (Schroeder et al., 2016) that, however, have a long revisit interval. Besides the new sensors, more field campaigns are needed in important areas for understanding emissions from small

fires, although limited campaigns have been conducted (Kim Oanh et al., 2011; Liu et al., 2016).

References

Baucum, L., R. Rice, and T. Schueneman (2002), An overview of Florida sugarcane, *Agronomy Department, Florida Cooperative Extension Service, Institute of Food and Agricultural Sciences, University of Florida. Publication# SS-AGR-232*.

Boden, T. A., G. Marland, and R. J. Andres (2017), Global, Regional, and National Fossil-Fuel CO2 Emissions, edited by O. R. N. L. Carbon Dioxide Information Analysis Center, U.S. Department of Energy, Oak Ridge, Tenn., U.S.A., doi: https://doi.org/10.3334/CDIAC/00001_V2017.

Borsdorff, T., J. Aan de Brugh, H. Hu, I. Aben, O. Hasekamp, and J. Landgraf (2018), Measuring Carbon Monoxide With TROPOMI: First Results and a Comparison With ECMWF‐IFS Analysis Data, Geophysical Research Letters, 45(6), 2826-2832, doi: https://doi.org/10.1002/2018GL077045.

Boschetti, L., and D. P. Roy (2009), Strategies for the fusion of satellite fire radiative power with burned area data for fire radiative energy derivation, *Journal of Geophysical Research: Atmospheres*, *114*(D20), D20302, doi: https://doi.org/10.1029/2008JD011645.

Csiszar, I., W. Schroeder, L. Giglio, E. Ellicott, K. P. Vadrevu, C. O. Justice, and B. Wind (2014), Active fires from the Suomi NPP Visible Infrared Imaging Radiometer Suite: Product status and first evaluation results, *Journal of*

Geophysical Research: Atmospheres, *119*(2), 2013JD020453, doi: https://doi.org/10.1002/2013JD020453.

Darmenov, A. S., and A. d. Silva (2015), The Quick Fire Emissions Dataset (QFED): Documentation of versions 2.1, 2.2 and 2.4*Rep. TM–2015–104606*, 212 pp, NASA.

Deeter, M. N., S. Martínez-Alonso, L. V. Gatti, M. Gloor, J. B. Miller, L. G. Domingues, and C. S. C. Correia (2016), Validation and analysis of MOPITT CO observations of the Amazon Basin, *Atmos. Meas. Tech.*, *9*(8), 3999-4012, doi: https://doi.org/10.5194/amt-9-3999-2016.

Eastham, S. D., and D. J. Jacob (2017), Limits on the ability of global Eulerian models to resolve intercontinental transport of chemical plumes, *Atmos. Chem. Phys.*, *17*(4), 2543-2553, doi: https://doi.org/10.5194/acp-17-2543-2017.

Freeborn, P. H., Wooster, M. J., Hao, W. M., Ryan, C. A., Nordgren, B. L., Baker, S. P., & Ichoku, C. (2008). Relationships between energy release, fuel mass loss, and trace gas and aerosol emissions during laboratory biomass fires. *Journal of Geophysical Research*, 113, DO1301, doi: https://doi.org/10.1029/2007JD008679.

Giglio, L., T. Loboda, D. P. Roy, B. Quayle, and C. O. Justice (2009), An active-fire based burned area mapping algorithm for the MODIS sensor, *Remote Sensing of Environment*, *113*(2), 408-420, doi: https://doi.org/10.1016/j.rse.2008.10.006.

Giglio, L., W. Schroeder, and C. O. Justice (2016), The collection 6 MODIS active fire detection algorithm and fire products, Remote Sensing of Environment, 178, 31-41, doi: https://doi.org/10.1016/j.rse.2016.02.054.

Hawbaker, T. J., M. K. Vanderhoof, Y.-J. Beal, J. D. Takacs, G. L. Schmidt, J. T. Falgout, B. Williams, N. M. Fairaux, M. K. Caldwell, J. J. Picotte, S. M. Howard, S. Stitt, and J. L. Dwyer (2017), Mapping burned areas using dense time-series of Landsat data, Remote Sensing of Environment, 198, 504-522, doi: https://doi.org/10.1016/j.rse.2017.06.027.

Heymann, J., M. Reuter, M. Buchwitz, O. Schneising, H. Bovensmann, J. P. Burrows, S. Massart, J. W. Kaiser, and D. Crisp (2017), CO2 emission of Indonesian fires in 2015 estimated from satellite-derived atmospheric CO2 concentrations, *Geophysical Research Letters*, *44*(3), 1537-1544, doi: https://doi.org/10.1002/2016GL072042.

Huang, R., X. Zhang, D. Chan, S. Kondragunta, G. Russell Armistead, and M. T. Odman (2018), Burned Area Comparisons Between Prescribed Burning Permits in Southeastern United States and Two Satellite‐Derived Products, Journal of Geophysical Research: Atmospheres, 123(9), 4746-4757, doi: https://doi.org/10.1029/2017JD028217.

Hudak, A. T., M. B. Dickinson, B. C. Bright, R. L. Kremens, E. L. Loudermilk, J. J. O'Brien, B. S. Hornsby, and R. D. Ottmar (2016), Measurements relating fire radiative energy density and surface fuel consumption – RxCADRE 2011 and 2012, *International Journal of Wildland Fire*, *25*(1), 25-37, doi: https://doi.org/10.1071/WF14159.

Ichoku, C., and L. Ellison (2014), Global top-down smoke-aerosol emissions estimation using satellite fire radiative power measurements, *Atmos. Chem. Phys.*, *14*(13), 6643-6667, doi: https://doi.org/10.5194/acp-14-6643-2014.

Ingmann, P., B. Veihelmann, J. Langen, D. Lamarre, H. Stark, and G. B. Courrèges-Lacoste (2012), Requirements for the GMES Atmosphere Service and ESA's implementation concept: Sentinels-4/-5 and -5p, Remote Sensing of Environment, 120, 58-69, doi: https://doi.org/10.1016/j.rse.2012.01.023.

IPCC (2006). 2006 IPCC guidelines for National Greenhouse Gas Inventories. In H. S. Eggleston, et al. (Eds.), Prepared by the National Greenhouse gas Inventories Programme (Chap. 2, pp. 1–59). IGES, Japan.

Kim Oanh, N. T., B. T. Ly, D. Tipayarom, B. R. Manandhar, P. Prapat, C. D. Simpson, and L. J. Sally Liu (2011), Characterization of particulate matter emission from open burning of rice straw, Atmospheric Environment, 45(2), 493-502, doi: https://doi.org/10.1016/j.atmosenv.2010.09.023.

Kim, P. S., D. J. Jacob, J. A. Fisher, K. Travis, K. Yu, L. Zhu, R. M. Yantosca, M. Sulprizio, J. L. Jimenez, and P. Campuzano-Jost (2015), Sources, seasonality, and trends of southeast US aerosol: an integrated analysis of surface, aircraft, and satellite observations with the GEOS-Chem chemical transport model, *Atmospheric Chemistry and Physics*, *15*(18), 10411-10433, doi: https://dx.doi.org/10.5194/acp-15-10411-2015.

Lefsky, M. A., W. B. Cohen, D. J. Harding, G. G. Parker, S. A. Acker, and S. T. Gower (2002), Lidar remote sensing of above‐ground biomass in three biomes, *Global Ecology and Biogeography*, *11*(5), 393-399, doi: https://doi.org/10.1046/j.1466-822x.2002.00303.x.

Liu, X., Y. Zhang, L. G. Huey, R. J. Yokelson, Y. Wang, J. L. Jimenez, P. Campuzano-Jost, A. J. Beyersdorf, D. R. Blake, Y. Choi, J. M. St. Clair, J. D. Crounse, D. A.

Day, G. S. Diskin, A. Fried, S. R. Hall, T. F. Hanisco, L. E. King, S. Meinardi, T. Mikoviny, B. B. Palm, J. Peischl, A. E. Perring, I. B. Pollack, T. B. Ryerson, G. Sachse, J. P. Schwarz, I. J. Simpson, D. J. Tanner, K. L. Thornhill, K. Ullmann, R. J. Weber, P. O. Wennberg, A. Wisthaler, G. M. Wolfe, and L. D. Ziemba (2016), Agricultural fires in the southeastern U.S. during SEAC4RS: Emissions of trace gases and particles and evolution of ozone, reactive nitrogen, and organic aerosol, Journal of Geophysical Research: Atmospheres, 121(12), 2016JD025040, doi: https://doi.org/10.1002/2016JD025040.

McCarty, J. L. (2011), Remote Sensing-Based Estimates of Annual and Seasonal Emissions from Crop Residue Burning in the Contiguous United States, Journal of the Air & Waste Management Association, 61(1), 22-34, doi: https://doi.org/10.3155/1047-3289.61.1.22.

Peterson, B., K. J. Nelson, C. Seielstad, J. Stoker, W. M. Jolly, and R. Parsons (2015), Automated integration of lidar into the LANDFIRE product suite, *Remote Sensing Letters*, *6*(3), 247-256, doi: https://doi.org/10.1080/2150704X.2015.1029086.

Randerson, J. T., Y. Chen, G. R. van der Werf, B. M. Rogers, and D. C. Morton (2012), Global burned area and biomass burning emissions from small fires, Journal of Geophysical Research: Biogeosciences, 117(G4), G04012, doi: https://doi.org/10.1029/2012JG002128.

Reid, J. S., E. J. Hyer, E. M. Prins, D. L. Westphal, Z. Jianglong, W. Jun, S. A. Christopher, C. A. Curtis, C. C. Schmidt, D. P. Eleuterio, K. A. Richardson, and J. P. Hoffman (2009), Global Monitoring and Forecasting of Biomass-Burning Smoke: Description of and Lessons From the Fire Locating and Modeling of

Burning Emissions (FLAMBE) Program, *Selected Topics in Applied Earth Observations and Remote Sensing, IEEE Journal of*, *2*(3), 144-162, doi: https://doi.org/10.1109/JSTARS.2009.2027443.

Roy, D. P., L. Boschetti, C. O. Justice, and J. Ju (2008), The collection 5 MODIS burned area product — Global evaluation by comparison with the MODIS active fire product, *Remote Sensing of Environment*, *112*(9), 3690-3707, doi: https://doi.org/10.1016/j.rse.2008.05.013.

Schmidt, C. C., J. Hoffman, and E. M. Prins (2012), GOES-R Advanced Baseline Imager (ABI) Algorithm Theoretical Basis Document For Fire / Hot Spot Characterization Version 2.5, edited, pp. 1-97, NOAA NESDIS STAR.

Schmit, T. J., P. Griffith, M. M. Gunshor, J. M. Daniels, S. J. Goodman, and W. J. Lebair (2017), A Closer Look at the ABI on the GOES-R Series, *Bulletin of the American Meteorological Society*, *98*(4), 681-698, doi: https://doi.org/10.1175/bams-d-15-00230.1.

van der Werf, G. R., J. T. Randerson, L. Giglio, G. J. Collatz, M. Mu, P. S. Kasibhatla, D. C. Morton, R. S. DeFries, Y. Jin, and T. T. van Leeuwen (2010), Global fire emissions and the contribution of deforestation, savanna, forest, agricultural, and peat fires (1997–2009), *Atmos. Chem. Phys.*, *10*(23), 11707-11735, doi: https://doi.org/10.5194/acp-10-11707-2010.

van der Werf, G. R., J. T. Randerson, L. Giglio, T. T. van Leeuwen, Y. Chen, B. M. Rogers, M. Mu, M. J. E. van Marle, D. C. Morton, G. J. Collatz, R. J. Yokelson, and P. S. Kasibhatla (2017), Global fire emissions estimates during 1997–2016,

Earth Syst. Sci. Data, *9*(2), 697-720, doi: https://doi.org/10.5194/essd-9-697-2017.

Veraverbeke, S., and S. J. Hook (2013), Evaluating spectral indices and spectral mixture analysis for assessing fire severity, combustion completeness and carbon emissions, *International Journal of Wildland Fire*, *22*(5), 707-720, doi: https://doi.org/10.1071/WF12168.

Wang, J., Y. Yue, Y. Wang, C. Ichoku, L. Ellison, and J. Zeng (2018), Mitigating Satellite-Based Fire Sampling Limitations in Deriving Biomass Burning Emission Rates: Application to WRF-Chem Model Over the Northern sub-Saharan African Region, *Journal of Geophysical Research: Atmospheres*, *123*(1), 507-528, doi: https://doi.org/10.1002/2017JD026840.

Wiedinmyer, C., S. K. Akagi, R. J. Yokelson, L. K. Emmons, J. A. Al-Saadi, J. J. Orlando, and A. J. Soja (2011), The Fire INventory from NCAR (FINN): a high resolution global model to estimate the emissions from open burning, *Geosci. Model Dev.*, *4*(3), 625-641, doi: https://doi.org/10.5194/gmd-4-625-2011.

Wolfe, R. E., G. Lin, M. Nishihama, K. P. Tewari, J. C. Tilton, and A. R. Isaacman (2013), Suomi NPP VIIRS prelaunch and on-orbit geometric calibration and characterization, *Journal of Geophysical Research: Atmospheres*, *118*(20), 2013JD020508, doi: https://doi.org/10.1002/jgrd.50873.

Wolfe, R. E., D. P. Roy, and E. Vermote (1998), MODIS land data storage, gridding, and compositing methodology: Level 2 grid, *Geoscience and Remote Sensing, IEEE Transactions on*, *36*(4), 1324-1338, doi: https://doi.org/10.1109/36.701082.

Wooster, M. J., Roberts, G., Perry, G. L. W., & Kaufman, Y. J. (2005). Retrieval of biomass combustion rates and totals from fire radiative power observations: FRP derivation and calibration relationships between biomass consumption and fire radiative energy release. *Journal of Geophysical Research*, 110, D24311, doi: https://doi.org/10.1029/2005JD006318.

Wooster, M. J., G. Roberts, P. H. Freeborn, W. Xu, Y. Govaerts, R. Beeby, J. He, A. Lattanzio, D. Fisher, and R. Mullen (2015), LSA SAF Meteosat FRP products – Part 1: Algorithms, product contents, and analysis, *Atmos. Chem. Phys.*, *15*(22), 13217-13239, doi: https://doi.org/10.5194/acp-15-13217-2015.

Xu, W., M. J. Wooster, T. Kaneko, J. He, T. Zhang, and D. Fisher (2017), Major advances in geostationary fire radiative power (FRP) retrieval over Asia and Australia stemming from use of Himarawi-8 AHI, *Remote Sensing of Environment*, *193*, 138-149, doi: https://doi.org/10.1016/j.rse.2017.02.024.

Zhang, F., J. Wang, C. Ichoku, E. J. Hyer, Z. Yang, C. Ge, S. Su, X. Zhang, S. Kondragunta, and J. W. Kaiser (2014), Sensitivity of mesoscale modeling of smoke direct radiative effect to the emission inventory: a case study in northern sub-Saharan African region, *Environmental Research Letters*, *9*(7), 075002, doi: https:// dx.doi.org/10.1088/1748-9326/9/7/075002.

Zhang, T., M. J. Wooster, and W. Xu (2017), Approaches for synergistically exploiting VIIRS I- and M-Band data in regional active fire detection and FRP assessment: A demonstration with respect to agricultural residue burning in Eastern China, Remote Sensing of Environment, 198, 407-424, doi: https://doi.org/10.1016/j.rse.2017.06.028.

Zhang, X., S. Kondragunta, J. Ram, C. Schmidt, and H.-C. Huang (2012), Near-real-time global biomass burning emissions product from geostationary satellite constellation, *Journal of Geophysical Research-Atmospheres, 117*, doi: https://doi.org/10.1029/2012jd017459.